

Search for charged long-lived particles with the ATLAS detector in pp collisions at $\sqrt{s} = 8$ TeV

Research Thesis



In Partial Fulfillment of the Requirements for the Degree of
Doctor of Philosophy

Revital Kopeliansky

CERN-THESIS-2015-119
24/08/2015



Submitted to the Senate of the
Technion – Israel Institute of Technology
Elul Haifa August 2015

This research thesis was done under the supervision of
Prof. Shlomit Tarem in the Faculty of Physics.

The generous financial help of the Technion is gratefully
acknowledged.

Acknowledgments

This great journey would not have been accomplished without the help, guidance and support of many people I met on my way.

High-Energy physics is a very challenging field of research. And the ATLAS collaboration, that is an international composition of many dedicated people who spends days and nights devoting their time to find the existence of new physics, is a supporting environment for this task. The work is done with endless excitement and enthusiasm that is not always understandable to an outsider.

While I was summarizing my study I couldn't help noticing the resemblance between this time in my life to the adventures of Alice in Wonderland:

"But I don't want to go among mad people," Alice remarked.

"Oh, you can't help that," said the Cat: "we're all mad here. I'm mad. You're mad."

"How do you know I'm mad?" said Alice.

"You must be," said the Cat, "or you wouldn't have come here."

Lewis Carroll, Alice in Wonderland

I am very proud and grateful that I am a part of this collaboration, as much as the intensive work and commotion seem sometimes as 'mad' from the outside.

And so, I would like to thank first and most to Prof. Shlomit Tarem, who granted me with this amazing opportunity, even though my lack of experience in this field of research at the beginning.

Shlomit, your care, devotion and enthusiasm for the research and detector work are admirable and I have learned so much from you, in so many different aspects. I know it was not easy at times, but I appreciate every moment and every stage I spent under your supervision. You are a remarkable and unique person and I am honored to be your graduate. Thank you.

To my closest colleagues who became very good friends, Shikma, Silvia, Enrique and Elisa: thank you for teaching me the tools of this work, for your time and explanations and for always being there. It was a pleasure working by your side and learning from you, and you will always have a warm place in my heart.

To Yoram Rozen, thank you for the advises and unique point of view, but mostly, thank you for making my time in the group more interesting and for teaching me to take life more lightly ☺

To Yael Shadmi, thank you for insisting and caring for my knowledge, and for the fruitful consultations and advises to our research.

To the people from the ATLAS Moun collaboration whom I had the pleasure working with and learning from: Giora Mikenberg, Stefan Schlenker, Slava K., Slava F., Masaya Ishino, Toshi Sumida and their great team, Thank you all.

Special thanks to Stephanie Zimmermann, for never saying no when in need of advice, and for the constant whiling to share her endless knowledge, even at the most stressful times.

To our most kindness analysis convener Monica D'Onofrio thank you for all the help. And to the people of the SMP group: Troels, Sascha, and Jorge-Armando for the great times we worked together.

To colleagues and friends I have, met and worked with along the way: Shany, Yaniv, Iftah, Moti, Shahrazad, Sofia, Gabe, Sho, Henso, Susan, Yonatan, Vera, Ofri, Michael, Tal, Anat, Israel, Dor, Ohad, Alex, Omri and Yoav – it has been a pleasure!

David, thanks for being there and for always willing to help ☺

Eitan and Niv, thank you for many brainstorming, funny moments, but mostly for being part of my life.

To the administrative and technical staff of the Physics faculty and the graduate school who always took care of matters, even if it was at the last moment: Noam, Israel, Orly, Eti, Irit, Avital, Sharon, Yan, Avi, Misha and Rauia – Thank you!

To Prof. Leonid Feigel Burlachkov, you would always have my endless gratitude.

To my mentor, advisor and amazing person who became family – Dr. Ania Kibrik, without you none of this was feasible. Thank you from the bottom of my heart.

To my closest family, my beloved grandmother – Sima and my brother – Avishai, Thank you for being there.

Last but not least, I mostly thank my dearest mother – Mirit, without you none of this would mean a thing.

In memory of my late grandfather, who is an inspiration to me all my life, Alex, you will always be missed...

And so I summaries,

"Begin at the beginning," the King said gravely, "and go on till you come to the end: then stop..."

Alice's Adventures in Wonderland, Lewis Carroll

Contents

Abstract.....	1
List of Abbreviations and symbols.....	2
List of publications	3
I. Introduction.....	4
II. Motivation for physics beyond the Standard Model.....	7
III. Supersymmetry [20] [21].....	8
i. Minimal Supersymmetric Standard Model (MSSM)	9
ii. R-parity	12
iii. SUSY breaking	12
(i) Gauge Mediated SUSY Breaking (GMSB).....	13
(ii) Split-Supersymmetry (SplitSUSY).....	14
(iii) Simplified Models.....	17
IV. The LHC and the ATLAS detector.....	21
i. The LHC	21
ii. The ATLAS detector.....	22
(i) The Pixel sub-detector	24
(ii) The calorimetric system.....	25
(iii) The Muon Spectrometer.....	25
V. Measurement Strategy	29
VI. Data and simulated samples	35
i. Data.....	35
ii. Simulated Monte-Carlo (MC) Samples.....	35
(i) Simulated Background Samples	36
(ii) Simulated Signal Samples.....	36
VII. Mass reconstruction.....	39
i. Mass from dEdX measurement	39
ii. Mass from ToF measurements.....	41
(i) Measurement.....	42

Contents – continue

(ii)	ToF measurement calibration	43
(iii)	Calibration of $\sigma\beta$ scale	46
(iv)	Smearing simulated MC hit time measurements	46
(v)	Internal consistency of a β measurement	47
(vi)	Combining β measurements.....	50
VIII.	Selection	51
i.	Online event selection – Triggers	51
(i)	Single-Muon trigger	51
(ii)	Missing transvers momentum trigger	54
(iii)	Total trigger efficiency.....	54
ii.	Offline event selection	57
iii.	Offline candidate selection	58
(i)	Sleptons	58
(ii)	Charginos	62
(iii)	R-hadrons	64
IX.	Background Estimation	72
i.	Sleptons and Charginos.....	73
ii.	R-Hadrons.....	77
X.	Systematic Uncertainties	80
i.	Theoretical cross-sections	81
ii.	Expected signal	81
(i)	Muon trigger efficiency	81
(ii)	Missing transverse momentum trigger	84
(iii)	Missing transverse momentum offline cut for charginos.....	88
(iv)	Initial state radiation in GMSB, LeptoSUSY and stable chargino events 91	
(v)	Initial state radiation in R-hadron events.....	93
(vi)	Time smearing in signal samples	93
(vii)	Uncertainty in $\beta\gamma$ from pixel $dEdx$	96

Contents – continue

(viii) Luminosity.....	96
iii. Background estimation in the slepton search.....	97
(i) Momentum independence of the β distribution.....	97
(ii) Variability of β in the η regions	99
(iii) Source independence of the β distribution	100
(iv) Presence of signal	102
iv. Background estimation in the chargino search	104
v. Background estimation in the R-hadron search.....	104
XI. Results	106
i. Sleptons	106
ii. Charginos.....	113
iii. R-Hadrons.....	114
XII. Summary	117
XIII. Bibliography	118
תקציר	I

List of figures

Figure 1: Cut-away view of the ATLAS detector [26].....	22
Figure 2: Cut-away view of the ATLAS muon system.....	26
Figure 3: Cross-section of MDT tube [26].	28
Figure 4: Left: Distribution of $dEdX$ vs. charge times momentum for minimum bias collisions in a data sample from 2010. Right: Simulated distribution of specific energy loss vs. momentum for singly-charged hypothetical R-hadrons of various masses.....	41
Figure 5: The relative shift of all calorimeter cell time measurements averaged per run as a function of run-number before any calibration is performed.	44
Figure 6: A comparison of calorimeter cell times (left) and the reconstructed β (right) before (black) and after (red) calibration.	45
Figure 7: A comparison of the calorimeter energy deposits for sleptons (red), R-hadrons (green) and muons (blue).	45
Figure 9: Pulls of the β measurement for muons from data in the calorimeters (top), the MDTs (middle) and the RPCs (bottom).	48
Figure 9: Hit times (left) and β measurement distribution (right) for $Z \rightarrow \mu\mu$ events before (black) and after (red) calibration for the RPC (top) and MDT (bottom).	49
Figure 11: Distribution of the β from the calorimeter measurements (left) and the combined β (right) obtained for selected $Z \rightarrow \mu\mu$ events in MC before (red) and after (blue) the smearing procedure.....	50
Figure 11: Left: Muon trigger efficiency in simulated GMSB events as a function of the trigger hit β (after correcting the mean with respect to BC according to the data). Right: Distribution of β for trigger candidates (line) and for all candidates in the event (points) passing the trigger. Candidates with β below the trigger threshold are found in triggered events when there is another higher- β particle that triggered the event.	53
Figure 12: Expected efficiency of the muon triggers (green points), the <i>ETmiss</i> triggers (purple triangles) and a logical OR of the two (blue squares) for GMSB events, as a function of the stau mass.	55
Figure 13: Expected efficiency of the muon triggers (green points), the <i>ETmiss</i> triggers (purple triangles) and a logical OR of the two (blue squares) for LeptoSUSY events as a function of squark mass (left) and gluino mass (right).	56
Figure 14: Expected efficiency of the muon triggers (green points), the <i>ETmiss</i> triggers (purple triangles) and a logical OR of the two (blue squares) for the long-	

lived chargino samples as a function of the chargino mass (left) and gluino within the R-hadron simulation (right).	56
Figure 15: The number of calorimeter cells plus MS hits contributing to the β measurement, minus the number of sub-detector systems used for a signal slepton sample.	60
Figure 16: The mean value of the reconstructed mass peak as a function of the slepton (left) and chargino (right) truth mass, for different mass hypothesis. ...	62
Figure 17: ET_{miss} vs. $\Delta\phi$ between the reconstructed LLP and the ET_{miss} for data (left) and for simulated chargino-neutralino sample (right).....	66
Figure 18: β distribution of data in the different η regions of the slepton search.	74
Figure 19: Reconstructed mass $m\beta$ of one candidate (m_2) vs. $m\beta$ of the other candidate (m_1) for observed data (black) and expected signal (red) in the GMSB slepton search in the two-candidate signal-region (top-left). Observed data, background estimate and expected signal (red/blue) in the slepton search for the lower of the two masses (m) in the two-candidate signal-region (GMSB τ_1 masses of 344.5 and 437 GeV) (top-right), and for the one-candidate signal-region (LeptoSUSY simulation mass $m_q = 2.0, 1.2$ and 0.9 TeV with $m_g = 1.2$ TeV) (bottom).	75
Figure 20: Reconstruction mass $m\beta$ in observed data, background estimate and expected signal ($\chi_1 \pm$ masses of 400 and 600 GeV) in the chargino search for the lower of the two masses in the two-candidate signal-region (top-left), for the one-loose-candidate signal region (middle) and the one candidate signal-region (bottom).....	76
Figure 21: Data and background estimation for $m\beta$ (left) and $m\beta\gamma$ (right) in the full-detector R-hadron search of a 500GeV gluino.....	78
Figure 22: Data and background estimation for $m\beta$ (left) and $m\beta\gamma$ (right) in the full-detector R-hadron search of a 500GeV stop.	78
Figure 23: Data and background estimation for $m\beta$ (left) and $m\beta\gamma$ (right) in the full-detector R-hadron search of a 500GeV sbottom.	79
Figure 24: Top: Comparison between the hit time distribution in uncalibrated data (solid line) and in smeared simulated $Z \rightarrow \mu\mu$ events (dashed line). Middle: The β distribution in simulated GMSB events before (solid line) and after (dashed line) the RPC hit times were smeared to correspond to uncalibrated data. Bottom: Muon trigger efficiency in simulated GMSB events as a function of the trigger hit β in each of the three η barrel regions.....	83
Figure 25: Turn-on curve for the xe70 (left) and xe80_tclcw_loose (right) trigger chains in $Z \rightarrow \mu\mu$ data (blue) and in MC (red).....	87

Figure 26: Missing transverse energy distribution for $Z \rightarrow \mu\mu$ (data in red, MC in blue) events, overlaid with three different stable Chargino of 400/700 GeV (left) and Gluino R-hadrons of 300/1300 GeV (right) signal events, respectively.	87
Figure 27: Comparison between the ET_{miss} distribution from the reconstruction and the MissingETUtility for an exemplary chargino signal sample with a chargino mass of 400 GeV.	91
Figure 28: The β measurements of $Z \rightarrow \mu\mu$ events in the Calorimeters (top), MDTs (middle) and RPCs (bottom) with decreased (red) and increased (green) smearing of MC compared to the data (black).	94
Figure 30: Combined β distribution of $Z \rightarrow \mu\mu$ in the data (black) and MC smeared with up (green) and down (red) smearing factors.	95
Figure 31: The $\beta\gamma$ measurements for muons from $Z \rightarrow \mu\mu$ in the data (red) and MC (blue).	95
Figure 32: The mass distribution of $\tau 1l$ with a mass of 248.6 GeV smeared with nominal (blue), up (green) and down (red) factors.	95
Figure 33: The background estimates obtained for the two-candidate (left) and one-candidate (right) SRs in the slepton search by using β PDFs obtained from ‘high-p’ and ‘low-p’ candidates.	98
Figure 33: Momentum distributions for a sample of muons in data with $\beta < 0.95$ and with $\beta > 0.95$ (red).	99
Figure 35: Comparison of the background estimation for the sleptons search using β distributions with (red) and without (blue) the Z veto for the two-candidate (left) and the one-candidate (right) signal regions.	101
Figure 36: Comparison of the background estimate for the slepton search with 8 and 25 η regions for the two-candidate (left) and the one-candidate (right) signal-regions. The black line shows the background estimation obtained when dividing into 8 η regions, and the red line shows the background estimation obtained when dividing into 25 η regions.	101
Figure 37: Mass distribution (left) and background estimation (right) for a data sample contaminated with GMSB MC signal for the one-candidate signal-region.	103
Figure 38: Mass distribution (left) and background estimation (right) for a data sample contaminated with GMSB MC signal for the two-candidate signal-region.	103
Figure 38: RMS between the resulting backgrounds estimated using baseline, tighter and looser selections for the PDF as a function of mass hypothesis. These results are fitted with a line which is then used as the final mass dependent systematic uncertainty on the background estimate.	105

Figure 40: Cross-section upper limits as a function of the mass of the lightest stau for the GMSB models with $\tan\beta = 10, 20$ (upper first row) 30,40 (middle row) and 50 (bottom row). The expected limit is drawn as a dashed black line with $\pm 1\sigma$ and $\pm 2\sigma$ uncertainty bands drawn in green and yellow, respectively. The observed limit is shown as solid black line with markers. The theoretical cross-section prediction is shown as a solid blue line with a shaded $\pm 1\sigma$ uncertainty band..... 109

Figure 41: Cross-section upper limits as a function of the $\tau 1$ mass for direct $\tau 1$ production and three values of $\tan\beta$. The expected limit for $\tan\beta = 10$ is drawn as a dashed line with $\pm 1\sigma$ and $\pm 2\sigma$ uncertainty bands drawn in green and yellow, respectively. The observed limit for the three values of $\tan\beta$ are shown as solid lines with markers. The theoretical cross-section prediction for $\tan\beta = 10$ is shown as a colored $\pm 1\sigma$ band, and does not vary significantly for other $\tan\beta$ values. 110

Figure 42: 95% CL excluded regions for directly produced sleptons in the plane $m_l - m_{\tau 1}$ vs. $m_{\tau 1}$. The excluded region is shown in blue. The expected limit is drawn as a solid black line with a $\pm 1\sigma$ uncertainty band drawn in dashed black lines. The observed limit is shown as solid red line with a $\pm 1\sigma$ uncertainty band drawn as dashed red lines..... 110

Figure 43: 95% CL excluded regions for squark and gluino mass in the LeptoSUSY models. The excluded region is shown in blue. The expected limit is drawn as a solid black line with a $\pm 1\sigma$ uncertainty band drawn in dashed black lines. The observed limit is shown as solid red line with a $\pm 1\sigma$ uncertainty band drawn as dashed red lines..... 111

Figure 44: Cross-section upper limits as a function of the $\chi 1$ mass for $\tau 1$ sleptons resulting from the decay of directly produced charginos and neutralinos in GMSB. Observed limits are given as a solid black line with markers. Expected limits for $\tan\beta = 10$ are drawn as a dashed black line with $\pm 1\sigma$ and $\pm 2\sigma$ uncertainty bands drawn in green and yellow, respectively. The theoretical cross-section prediction (dominated by $\chi 1 \pm \chi 10$ production) is shown as a colored $\pm 1\sigma$ band. Depending on the hypothesis and to a small extent on $\tan\beta$, in these models, the chargino mass is 210 to 260 GeV higher than the neutralino mass..... 111

Figure 45: Cross-section upper limits as a function of the LLP mass for the R-hadron search. The expected limit is drawn as a dashed black line with $\pm 1\sigma$ and $\pm 2\sigma$ uncertainty bands drawn in green and yellow, respectively. The observed limit is shown as solid black line with markers. The theoretical cross-section prediction is shown as a solid blue line with a shaded $\pm 1\sigma$ uncertainty band..... 116

List of tables

Table 1: List of SM particles and their superpartners according to the MSSM..	11
Table 2: List of mixed mass states in the MSSM.	11
Table 3: Overview of all searches, mass ranges and signal regions.....	33
Table 4: Number of events in data and expected number of events and the efficiency in the signal simulation at each step of the events selection for several signal models.	60
Table 5: Number of candidates in data and expected number of candidates and the efficiency in the signal simulation at each step of the candidates selection for several signal models.	61
Table 6: Number of events in data and expected signal efficiency at each step of the event selection for the stable chargino models, for chargino–chargino, chargino–neutralino and in total	67
Table 7: Number of candidates in data and the expected signal efficiency at each step of the candidate selection for a stable chargino model with mass of 300GeV for chargino–chargino, chargino–neutralino SR and in total	68
Table 8: Number of candidates in data and the expected signal efficiency at each step of the candidate selection for a stable chargino model with mass of 700GeV for chargino–chargino, chargino–neutralino SR and in total	69
Table 9: Full-detector search of R-hadron candidate selection requirement for a combined track.	70
Table 10: Full-detector search of R-hadron candidate selection requirement for an ID+ Calo track.	71
Table 11: Definition of the 8 η regions.	74
Table 12: Summary of systematic uncertainties for the slepton searches (in percentages). Ranges indicate a mass dependence for the given uncertainty (low-mass to high-mass).	80
Table 13: Summary of systematic uncertainties for the chargino and R-hadron searches (in percentages). Ranges indicate a mass dependence for the given uncertainty (low-mass to high-mass).	80
Table 14: Efficiencies and relative change with respect to the central values of the fit parameters obtained by multiplying the fitted $xe80_tclcw_loose$ turn-on curve, from $Z \rightarrow \mu\mu$ data, bin-by-bin with the ET_{miss} spectrum, for the 800 GeV gluino R-hadrons signal MC sample. Independent 1σ variations of the effective threshold (B) and the resolution (C) are shown.....	86

Table 15: Efficiencies and relative change with respect to the central values of the fit parameters obtained by multiplying the fitted <code>xe80_tclcw_loose</code> turn-on curve, from pile-up re-weighted $Z \rightarrow \mu\mu$ data, bin-by-bin with the <i>ETmiss</i> spectrum, for the 800 GeV gluino R-hadrons signal MC sample. Independent 1σ variations of the effective threshold (B) and the resolution (C) are shown.....	86
Table 16: Overview of the maximal relative missing transverse momentum trigger efficiency variations for various signal types (in percentages).....	86
Table 17: Various contributions and total systematic errors on the signal efficiency due to the <i>ETmissoffline</i> cut for some of the chargino models in the total chargino production.....	89
Table 18: Various contributions and total systematic errors on the signal efficiency due to the <i>ETmissoffline</i> cut for some of the chargino models in the chargino-neutralino production.....	90
Table 19: Overview of the effect of ISR variations for the GMSB samples. The numbers are given as percentage change with respect to the nominal sample..	92
Table 20: Overview of the effect of ISR variations for the LeptoSUSY samples. The numbers are given as percentage change with respect to the nominal sample.....	92
Table 21: Overview of the effect of ISR variations for the chargino samples. The numbers are given as percentage change with respect to the nominal sample..	92
Table 22: Momentum cut used in the different η regions to test the momentum dependence of the muon β PDF.....	97
Table 23: Summary of systematic uncertainties (given in percentages) for the chargino search. Ranges indicate mass dependence for the given uncertainty (low mass – high mass).....	104
Table 24: Variations of selection for PDFs used for background estimation. The RMS between the resulting backgrounds estimated using baseline, tighter and looser selections for the PDF is evaluated for each mass hypothesis.....	105
Table 25: Observed and expected event yields, as well as efficiencies and uncertainties for three MC simulation signal samples, in the two signal regions used in the GMSB slepton search. Cross-section upper limits are stated at 95% CL.....	112
Table 26: Observed and expected event yields, as well as efficiencies and uncertainties for three MC simulation signal samples, in the two signal regions used in the LeptoSUSY slepton search. Cross-section upper limits are stated at 95% CL.....	112
Table 27: Observed and expected event yields, as well as efficiencies and uncertainties for three MC simulation signal samples, in the two signal regions	

used in the chargino search. Cross-section upper limits are stated at 95% CL.
..... 114

Table 28: Observed and expected event yields, as well as efficiencies and
uncertainties for three MC simulation signal samples, in the two signal regions
used in the R-hadron search. Cross-section upper limits are stated at 95% CL.
..... 115

Table 29: Summary of the lower mass limits at 95% CL from the various searches.
..... 117

Abstract

Searches for heavy charged long-lived particles (LLPs) were performed under the Supersymmetry (SUSY) theory using data sample of 19.1 fb^{-1} from proton-proton collisions at center-of-mass energy $\sqrt{s} = 8 \text{ TeV}$ collected by the ATLAS detector at the Large-Hadron-Collider (LHC).

When traveling with a speed measurably lower than the speed of light, charged particles can be identified and their mass (m) determined from their measured speed (β) and momentum (p), using the relation: $m = \frac{p}{\beta\gamma}$, where the momentum p can be deduced from the particle's track in the detector, γ is the Lorenz factor, and the velocity β can be estimated from the measured Time-of-Flight (ToF) and from specific ionization energy loss $\frac{dE}{dx}$ that measures $\beta\gamma$.

The searches are based almost entirely on the characteristics of the LLP itself, but are further optimized for the different experimental signatures of sleptons, charginos and composite colorless states of a squark or gluino together with light Standard Model (SM) quarks or gluons, called R-hadrons.

No excess was observed above the estimated background and limits were placed on the mass of long-lived particles in various supersymmetric models. Long-lived tau sleptons in models with gauge-mediated SUSY breaking are excluded up to masses between 440 and 385 GeV for $\tan \beta$ between 10 and 50, with a 290 GeV limit in the case where only direct tau slepton production is considered. In the context of LeptoSUSY models, where sleptons are stable and have a mass of 300 GeV, squark and gluino masses are excluded up to a mass of 1500 and 1360 GeV, respectively. Directly produced stable charginos, that are nearly degenerate to the lightest neutralino, are excluded up to a mass of 620 GeV. R-hadrons, composites containing a gluino, bottom squark and top squark, are excluded up to a mass of 1270, 845 and 900 GeV, respectively, using the full detector.

List of Abbreviations and symbols

- **LLP**: Long-Lived Particle
- **LHC**: Large Hadron Collider
- **SUSY**: Supersymmetry
- **GMSB**: Gauge Mediated SUSY Breaking
- **SplitSUSY**: Split Supersymmetry
- **LeptoSUSY**: Leptogenic Supersymmetry
- **PVX**: Primary Vertex
- **ID**: Inner Detector
- **Calo**: Calorimeter
- **LAr**: Liquid Argon calorimeter
- **MS**: Muon Spectrometer
- **SM**: Standard Model
- **LSP**: Lightest Supersymmetric Particle
- **NLSP**: Next-to Lightest Supersymmetric Particle
- **LO**: Leading Order
- **NLO**: Next-to Leading Order
- **NLL**: Next-to Leading Order Logarithm
- **MDT**: Monitored Drift Tubes
- **RPC**: Resistive Plate Chambers
- **CSC**: Cathode Strip Chambers
- **TGC**: Thin Gap Chambers
- **ISR**: Initial State Radiation
- **FSR**: Final State Radiation
- **BC**: Bunch Crossing
- **RoI**: Region of Interest

- ToF: Time Of Flight
- CB: ID+ MS combined
- Full-detector: ID+ MS and ID+ Calo tracks
- SR: Signal Region
- CR: Control Region
- MC: Monte Carlo
- MSSM: Minimal Supersymmetric Standard Model
- IP: Interaction Point
- MET or E_T^{miss} : Missing Transvers Energy
- p_T : Transvers Momentum
- $\frac{dE}{dx}$: Specific Ionization Energy Loss
- EF: Event Filter
- HLT: High Level Trigger
- SR-SL-2C: Slepton two-candidate signal-region
- SR-SL-1C: Slepton one-candidate signal-region
- SR-CH-2C: Chargino two-candidate signal-region
- SR-CH-1LC: Chargino one-loose-candidate signal-region
- SR-CH-1C: Chargino one-candidate signal-region
- SR-RH-FD: R-hadron full-detector search

List of publications

“*Searches for heavy long-lived sleptons and R-Hadrons with the ATLAS detector in pp collisions at $\sqrt{s} = 7 \text{ TeV}$* ”, ATLAS Collaboration, Phys. Lett. **B** 720 (2013) 277–308

“*Searches for heavy long-lived charged particles with the ATLAS detector in pp collisions at $\sqrt{s} = 8 \text{ TeV}$* ”, ATLAS Collaboration, JHEP01(2015)068 (arxiv.org/pdf/1411.6795)

I. Introduction

Heavy long-lived particles (LLPs) are predicted in many extensions to the Standard Model (SM) [1]. R-parity conserving supersymmetry (SUSY) models, such as split SUSY [2] [3], gauge-mediated SUSY breaking (GMSB) [4] [5] [6] [7] [8] [9] [10] [11] and LeptoSUSY [12] [13], as well as other scenarios allow for a variety of LLP states stable enough to be directly identified by the ATLAS detector. These states include long-lived super-partners of the leptons, quarks and gluons: sleptons (\tilde{l}), squarks (\tilde{q}) and gluinos (\tilde{g}), respectively; as well as charginos ($\tilde{\chi}_{1,2}^{\pm}$), which together with neutralinos ($\tilde{\chi}_{1-4}^0$) are a mixture of super-partners of the Higgs and γ /W/Z bosons, known as Higgsinos, winos and binos.

This research focuses on the search for charged LLPs at the reach of the Large-Hadron Collider (LHC) and under the Supersymmetry (SUSY) theory.

When traveling with a speed measurably lower than the speed of light, charged particles can be identified and their mass (m) determined from their measured speed (β) and momentum (p), using the relation: $m = \frac{p}{\beta\gamma}$, where the momentum p can be deduced from the particle's track in the detector, γ is the Lorentz factor, and the velocity β can be estimated from the measured Time-of-Flight (ToF) and from specific ionization energy loss $\frac{dE}{dx}$ that measure $\beta\gamma$.

The searches are based almost entirely on the characteristics of the LLP itself, but are further optimized for the different experimental signatures of sleptons, charginos and composite colorless states of a squark or gluino together with light SM quarks or gluons, called R-hadrons.

Long-lived charged sleptons would interact like muons, releasing energy by ionization as they pass through the ATLAS detector. A search for long-lived sleptons identified in both the inner detector (ID) and in the muon spectrometer (MS) is therefore performed ("slepton search). The search is optimized for GMSB

and LeptoSUSY models. In the former, the Gravitino is the lightest supersymmetric particle (LSP) and the light tau slepton ($\tilde{\tau}_1$) is the long-lived (long enough to be measured by all the ATLAS detector layers), next-to-lightest supersymmetric particle (NLSP). The $\tilde{\tau}_1$, the lightest $\tilde{\tau}$ mass eigenstate resulting from the mixture of the right-handed and left-handed leptons super-partners of the τ lepton, is predominantly the partner of the right-handed lepton in all models considered here. In addition to GMSB production, results are also interpreted for the case of direct production of charged sleptons, independently of the mass spectrum of other SUSY particles. The recent discovery of the Higgs boson with a mass of about 125 GeV [14] [15] disfavors minimal GMSB within reach of the LHC. For Higgs boson to have such mass, the top squark mass would have to be several TeV, and in GMSB the slepton masses are strictly related to the squark masses. However, modifications to minimal GMSB can easily accommodate the observed Higgs mass without changing the stau masses [16] [17] [18]. The LeptoSUSY models, characterized by final states with high multiplicity of leptons and jets, are studied in the context of a simplified model, where all the neutralinos and charginos are decoupled with the exception of the $\tilde{\chi}_1^0$, and the sleptons are long-lived and degenerate, with a mass set to 300 GeV, a value motivated by exclusion limits of previous searches [19]. In these models a substantial fraction of the events would contain two LLP candidates, a feature also used to discriminate signal from background.

Charginos can be long-lived in scenarios where the LSP is a nearly pure wino and is mass-degenerate with the charged wino. The chargino signature in the detector would be the same as for a slepton, but the dominant production is in chargino-neutralino ($\tilde{\chi}_1^\pm \tilde{\chi}_1^0$) pairs, where the neutralino leaves the apparatus undetected. As a result, the event would have one LLP and significant missing transverse

momentum (\vec{p}_T^{miss} with magnitude denoted by E_T^{miss}). This signature is used in a dedicated “chargino search”.

Colored LLPs (\tilde{q} and \tilde{g}) would hadronise forming R-hadrons, bound states composed of the LLP and light SM quarks or gluons. They may emerge as charged or neutral states from the pp collisions and be converted to a state with a different charge by interactions with the detector material, and thus arrive as neutral, charged or doubly charged particles in the MS. Searches for R-hadrons are performed using all available detector information (“full detector R-hadrons search”). In the R-hadron search the LLPs considered are either gluino, stop or sbottom.

In all searches the relatively massive LLPs are distinguishable from SM relativistic particles by their lower velocity ($\beta < 1$), and the expected background for these physical scenarios is mainly boosted muons with miss-measured β .

II. Motivation for physics beyond the Standard Model

The theory of the Standard Model (SM) of high-energy physics describes the current understanding of interactions of fermionic particles – the compositors of all matter as we know today, mediated by gauge bosons – the force carriers of the interaction itself. The lagrangian density is used to describe the dynamics and kinematics of the system and requires its terms to be invariant under both global and local transformations $SU(3)\times SU(2)\times U(1)$. Spontaneous symmetry breaking via the Higgs mechanism generates masses for fermions and gauge bosons.

The SM was experimentally tested at the ranges of eV and up to the 100 GeV scale, yet other experimental evidences and theoretical studies show the SM is an incomplete theory:

- The fundamental force of Gravitation is not taken into consideration in the SM. Although there is an assumption that this force is mediated by a gauge boson called ‘*graviton*’, quantum field theories break down before reaching the Plank scale ($M_p \sim 2.4 \times 10^{18} GeV$) where quantum gravitational effects can no longer be neglected.
- The SM considers *neutrinos* to be massless, yet there are experimental evidence that suggest otherwise.
- Astronomical and cosmological observations indicate the existence of dark-matter and that it accounts for most of the matter in the universe, however no candidate is considered in the SM for it.
- High-order loop corrections of off-shell particles coupling to the Higgs field result in the higgs mass correction dependence in the momentum cut-off, Λ_{UV}^2 (at the order of the Plank scale). This results in enormous quantum corrections to the Higgs mass, much higher than the Higgs mass itself [20].

- Extensions to the SM such as the ‘Grand Unification Theory’ (GUT) and the ‘Theory of everything’ attempts to bring all forces of interaction (strong, electromagnetic and weak) together into a framework of a single field where all the coupling constants of the SM come to a single coupling point.

The above strengthen the need for an extension to the SM, one which will satisfy physics at higher energy scales and include new variables to cancel the diverging corrections to the Higgs mass.

One of the more elegant solutions is offered by the theory of Supersymmetry (SUSY).

III. Supersymmetry [20] [21]

Supersymmetry (SUSY) is a well-motivated theoretical framework extending the SM. SUSY suggest an elegant solution to the ‘*hierarchy problem*’, potential candidate for dark-matter and in some versions of it also the possibility of gauge coupling unification.

SUSY suggests symmetric relations between fermions and bosons i.e. every fundamental SM particle have a superpartner identical in every aspect but differ by $\frac{1}{2}$ spin unit from its own spin. Hence every SM fermionic degree of freedom have a superpartner with bosonic degree of freedom, and ‘*Supermultiplets*’ (a term defined to describe the SM particle and its super-partner states) that represent the superpartner of a SM particle state. Particles from the same supermultiplet will go through the same gauge transformations, same couplings and have the same electric charge, weak isospin and color charge.

SM fermions will have a spin-0 bosonic superpartners, named ‘*sfermions*’, scalar fermions. SM vector bosons will have a spin- $\frac{1}{2}$ fermion superpartner named as ‘*gaugino*’. The addition of these particles will cancel the loop corrections applied to the Higgs mass by contributing opposite sign terms to the equation.

Although SUSY implies that all particles of the same supermultiplet are degenerate in mass, the fact that no super-particle has been observed in none of the experiments conducted so far, suggest that SUSY, if it exists, is a broken symmetry.

i. Minimal Supersymmetric Standard Model (MSSM)

The MSSM is the simplest SUSY model available as an extension to the SM. It suggests the existence of a superpartner to each and every SM particle with a spin differing by a $\frac{1}{2}$ unit. As a result, the total number of particles predicted is doubled, since every SM fermion (lepton or quark) have two chirality states (left-handed and right-handed), will have two superpartners called ‘*sfermion*’s (*slepton*, and *squark*), one for each chiral state. The mass eigenstate of the scalar partners are a mixture of the *left* and *right* sfermions. Mixing between the lepton Yukawa’s are approximate slepton mass eigenstate. However, in general, the right-handed sleptons are lighter. For the τ -sleptons the mixing between the two chiral slepton states can be larger, hence the mass eigen states are usually called $\tilde{\tau}_2$ and $\tilde{\tau}_1$.

Each SM gauge boson have a fermionic superpartner called ‘*gaugino*’. There are 8 color-charge carriers *gluinos*, one for each of the SM gluons. The supersymmetric partners of the $SU(2)_L$: W and Z gauge bosons are fermions called ‘*Wino*’s and ‘*Zino*’, respectively, and the supersymmetric partner of the $U(1)_Y$ gauge boson: γ is a fermion called ‘*Bino*’ (‘*Photino*’).

In order to maintain the electroweak gauge symmetry, and hence give mass to the up-type and down-type fermions, SUSY requires the existence of two Higgs doublets. A Higgs with hypercharge $Y = \frac{1}{2}$ and the other Higgs with hypercharge $Y = -\frac{1}{2}$: (H_u^+, H_u^0) and (H_d^0, H_d^-) respectively, while a linear combination of the two neutral Higgs is the SM Higgs itself. Each Higgs doublet has its own Vacuum Expectation Value (VEV), and the ratio between the two VEVs is called $\tan\beta$. The superpartners of these Higgs field are fermions and are called ‘*Higgsinos*’. Table 1 specifies the different SM particles and their superpartners according to the MSSM.

As SUSY is expected to be a broken symmetry, the lagrangian will be the sum of two lagrangian terms: $L = L_{SUSY} + L_{soft}$, the SUSY term which contains all the gauge and Yukawa couplings $-L_{SUSY}$, and another for the soft breaking of the symmetry and will include only the mass terms and the coupling parameters $-L_{soft}$.

The two types of symmetry breaking: the electroweak symmetry breaking and the SUSY breaking, can cause mixing between the electroweak gauginos and the Higgsinos. The resulting mass states are four neutral particles called: ‘*neutralinos*’ and two charged particles called ‘*charginos*’. Table 2 specifies the resulting mixed states.

In some SUSY models the lightest-supersymmetric particle (LSP) is assumed to be the *Gravitino* (the superpartner of the presumably gravitational force carrier the ‘*graviton*’ G), and in others the lightest *Neutralino* (out of the four) that are potential candidates for a cold dark-matter.

SM particle	Spin	SUSY partner	Spin
Lepton l	$\frac{1}{2}$	Slepton \tilde{l}	0
Quark q	$\frac{1}{2}$	Squark \tilde{q}	0
Higgs H	0	Higgsino $(\tilde{H}_u^+, \tilde{H}_u^0), (\tilde{H}_d^-, \tilde{H}_d^0)$	$\frac{1}{2}$
Gluon g	1	Gluino \tilde{g}	$\frac{1}{2}$
W^\pm	1	Wino \tilde{W}^\pm	$\frac{1}{2}$
Z	1	Zino \tilde{Z}	$\frac{1}{2}$
Photon γ	1	Photino $\tilde{\gamma}$ (Bino)	$\frac{1}{2}$

Table 1: List of SM particles and their superpartners according to the MSSM.

Mixing mass states	SUSY particle
<i>Neutralinos</i> $\tilde{\chi}_4^0, \tilde{\chi}_3^0, \tilde{\chi}_2^0, \tilde{\chi}_1^0$	Zino \tilde{Z}
	Photino $\tilde{\gamma}$ (Bino)
	Neutral Higgsino $\tilde{H}_u^0, \tilde{H}_d^0$
Charginos $\tilde{\chi}_2^\pm, \tilde{\chi}_1^\pm$	Wino \tilde{W}^\pm
	Charged Higgsino $\tilde{H}_u^+, \tilde{H}_d^-$

Table 2: List of mixed mass states in the MSSM.

ii. R-parity

In the total MSSM lagrangian density all the SUSY terms are required to be gauge-invariant under transformations, yet there appear terms that violate the leptonic (L) and baryonic number (B) conservations, which is highly constrained experimentally. The MSSM solves this problem by introducing a new symmetry called R -parity, which forbids all L and B violating terms in the lagrangian.

R-parity symmetry associate to each particle the parameter:

$$\text{Equation 1: } P_R = (-1)^{3(B-L)+2S_1}$$

Where SM particles have $P_R = 1$ and SUSY particles $P_R = -1$.

The conservation of R-parity imply that the LSP will be stable (will not decay, as there is no SUSY particle lighter than it). All other SUSY particles will eventually decay into the LSP. And in case of collision experiments the SUSY particles will be produced in pairs.

iii. SUSY breaking

As SUSY expected to be a broken symmetry, the masses of the sparticles are assumed to be much higher than those of their SM partners. Most of the SUSY breaking models predict the sparticles to have a mass at the scale of $\sim 1\text{TeV}$. If that is indeed the case, there is a good chance to discover these particles at the collision experiments conducted in the Large-Hadron Collider (LHC) at CERN, where the center of mass energy can reach 14 TeV. Yet, this study was done based on 8 TeV collisions.

¹ B - baryonic number, L- leptonic number, S - the spin of the particle

There are many SUSY models currently available, all differ in the way the symmetry is broken. Among them are the Gauge Mediated SUSY Breaking (GMSB) and SplitSUSY, which will be discussed in this work. Simplified predictions, in the sense of less restriction and less variables that are considered here are: the LeptoSUSY and Stable Charginos models. Details on these models will be specified in the next sections.

(i) Gauge Mediated SUSY Breaking (GMSB)

In GSMB, the symmetry breaking is mediated by gauge interactions at the scale of \sqrt{F} (the fundamental SUSY breaking scale, i.e. the total contribution of the SUSY breaking VEV of the superfields). Three sectors are defined: the *observable* sector (refers to all SM fermions, two Higgs doublets and their superpartners), the *secluded* sector (refers to the SUSY breaking hidden sector) and the *messenger* sector (new superfields that transform under gauge group and couple to the tree-level secluded sector. These messengers are taken to be a complete representations of SU(5)). The coupling between the secluded sector and the messenger sector generates a supersymmetric mass term: $m_{messenger}$ for the messenger fields, and a squared term for the mass splitting between the messenger fields Δm^2 , at the order of \sqrt{F} . One loop diagrams involving the messenger fields give mass to the gauginos and two-loop diagrams to the sfermions.

The LSP in the GMSB models is the Gravitino (\tilde{G}) while the next-to-lightest-SUSY- particle (NLSP) can be either the lightest neutralino or a charged slepton. The \tilde{e}_R and $\tilde{\mu}_R$ sleptons are nearly mass degenerate, while the τ Yukawa coupling lowers the lightest $\tilde{\tau}$ mass through renormalization group evolution and left-right mixing. The NLSP in this case is the lightest $\tilde{\tau}$, i.e. $\tilde{\tau}_1$.

In general 6 main parameters characterize the GSMB models:

- $\Lambda = \frac{F}{m_{messenger}}$ the SUSY breaking mass scale
- $m_{messenger}$ – the messenger superfields mass
- N_5 – the number of messengers
- $\tan\beta$ – the ratio between the two Higgs doublets VEVs
- $sign(\mu)$ – the sign of the μ term (the Higgsino mass parameter)
- C_{grav} – the scale factor of the Gravitino mass

GMSB is an R-parity conserving model, hence whatever SUSY particle produced at the collision, it will eventually decay into the NLSP and then to the LSP (if these are not being directly produced). In these models, the NLSP life-time is proportional to c_{grav}^2 . Hence, if c_{grav}^2 is at the order of $o(\sim 10^3)$, the NLSP is relatively long-lived and has a decay length larger than the size of the detector. As a result, the signature left in the detector will be affected by the features of the NLSP. The NLSP scenario considered in this study is of a long-lived charged $\tilde{\tau}_1$, which is expected to interact in the detector like a heavy muon, losing energy through ionization as it passes through the detector.

(ii) Split-Supersymmetry (SplitSUSY)

SplitSUSY suggests that at high energies such as the Grand-Unification energy scale ($\Lambda_{GUT} \sim 10^{16} GeV$) new particles exist and SUSY at low energies is not probable. The superpartners of the SM gauge bosons (the gluino \tilde{g} , wino \tilde{W} , bino \tilde{B} and Higgsino doublets \tilde{H}_u and \tilde{H}_d) are predicted at the $\sim TeV$ scale, while all other SUSY particles are expected to have much higher masses, closer to the GUT scale. The possible LSP candidate in these models is the neutralino (a mixture of the Higgsino and Gaugino-Wino).

A striking feature of the SplitSUSY prediction is that the gluino is considered as stable particle and long-lived. Since the squarks in this model assume to have much higher masses, considering color charge constraints and R-parity conservation the gluino cannot decay to squarks and hence is the long-lived particle in this scenario.

The proton-proton collisions at the LHC give rise to the possibility of a strongly produced events to occur, and if SplitSUSY indeed exist it is likely that two gluinos will be produced at these collisions. The gluino is then expected to bind with SM colored particles through hadronization processes into a color-singlet state called *R*-hadron (R - refers to their non-trivial R-parity) at a mass of approximately the LLP (i.e. the gluino).

The type of hadron resulted depends on the other binding particles:

- R-baryon: a gluino bounding with 3 quarks: $qqq\tilde{g}$
- R-meson: a gluino bounding with a quark and an anti-quark: $q\bar{q}\tilde{g}$
- R-ball (gluino ball): a gluino bounding with a gluon: $g\tilde{g}$

This study also consider cases of third generation squarks (stop and sbottom) as LLP in similar compositions. The difference between such scenarios and a gluino-based R-hadron scenario will be detailed in the next sections.

Scattering of R-hadrons in the detector [22] [23]

The way the R-hadron scatter in the detector, and especially in the calorimeter can affect the detector signature left by the passing particle.

Both charged and neutral heavy hadrons loss energy through scattering-off a nuclei. Yet the probability that a parton such as the massive LLP will strongly interact with quarks in the target nucleon is small. Such interactions are suppressed by R-parity conservation as well as the invers squared mass of the

parton. Hence the massive R-hadron is a composition of non-interacting heavy stable LLP and colored hadronic cloud of light constituents responsible for the interaction. Since the kinetic energy carried by the light quarks is very small, the energy scale of the heavy hadron scattering processes off nucleons is low. The total cross-section scattering of such R-hadron in the detector will be roughly the same as regular hadron-hadron scattering carrying similar quark composition.

In gluino-based R-hadrons models, the scattering of the R-hadron is assumed to follow the generic-scattering model, i.e. does not depend on the energy carried by the R-hadron and the scattering rate is estimated with a constant geometric cross-section (12 mbarn for light quarks and 6 mbarn for s-quarks).

Exotic scenarios of long-lived stop or sbottom squarks are also considered. Here a light-squark (stop or sbottom) based R-hadrons scattering follows the triple-Regge model that was originally developed for exotic hadrons scattering [24]. Since these R-hadrons contain a light-quark system at low energies, it can be treated with the phenomenology describing a low energy hadron-hadron scattering. This is done in the triple Regge formalism where the scattering cross-section depends on the kinetic energy carried by the hadron.

The scattering of the R-hadron in the detector can change the electrical charge state formed by the R-hadron at the production and result in flip-charge cases. For example, if the initial electrical state of the R-hadron is charged, a track can be detected in the layers of the inner-detector. However, the scattering of the R-hadron within the calorimeter layers might result in a new hadronization state, which might be electrically neutral state or doubly charged. If the R-hadron will exit from the calorimeters as neutral, only a half-track (ID+ Calo information only) will be detected by the ATLAS detector. An opposite scenario where the R-hadron is produced neutral but turns into electrically charged in the calorimeters is also

possible. The best case scenario will be an R-hadron that is charged in all layers and will allow for a full track detection. Yet a worst case scenario where the R-hadron is neutral in all detector layers is another possibility and there is no way to predict which will be the case.

Since the net-charge of the R-baryon state is given by the total quark composition, the scattering in the calorimeters is expected to result in equal number of charged and neutral gluino-based R-hadrons. Yet, for stop-based R-hadrons twice as much will be charged while for the sbottom-based R-hadrons twice as much will be neutral, due to the electrical charge carried by these squarks.

R-hadron signature in the ATLAS detector [22]

Depending on the topology of the event, missing energy in neutral compositions can be indirectly measured at the reconstruction stage.

The measured ionization energy loss in the ID tracker is expected to be large with respect to SM relativistic particles due to the small velocity of the R-hadron.

The amount of energy deposited in the calorimeters divided by the momentum of the track, will be considerably smaller than that of light hadrons (that usually carry smaller momentum), but a bit larger than that of high-momentum muons. Hence also the shape of the shower in the calorimeter layers will be different (narrower).

The slow velocities will result in large measured ToF by the calorimeter and muon chambers.

(iii) Simplified Models

In the MSSM there are more than 100 free parameters influencing the signature of the long-lived particles via the appearance of intermediate sparticles cascade.

As a result a very large SUSY parameters space is created and the study is then done for very constrained models.

Lately it has become favored to use a more ‘simplified’ study, an approach of model-independent study, which reduces the parameter space by identifying the most important parameters that parametrize the mass spectrum, determines the sparticle signature in the detector but does not make assumptions about the origin of the sparticles.

In this study, three different simplified models are being considered: a stable slepton model – LeptoSUSY, stable charginos and R-hadrons with either stop or sbottom as the long-live particles. Details on these models are specified in the next sections.

Leptogenic Supersymmetry (LeptoSUSY)

Leptogenic Supersymmetry (LeptoSUSY) refers to a kinematic decay characterized by cascade decays with copious lepton production. The production of new particles is assumed to be dominated by QCD (Quantum Chromo Dynamic) production of squarks and gluinos, which are assumed to be at the top of the mass spectrum. Colored particles decay into lighter charginos and neutralinos that are predicted to be heavier than the sleptons and therefore decay into leptons and sleptons. All the sleptons decay into the lightest slepton – the NLSP, a collider stable particle that will eventually decay into the Gravitino outside of the detector range.

LeptoSUSY models usually considers the squark masses to be at the \sim TeV scale, nearly mass degenerate and the gluino to be either lighter or heavier than the squarks. Thus all three generations of squarks can be produced at the LHC. The Gravitino, the LSP, is assumed to be lighter than \sim 1GeV, and the $\tilde{\tau}_1$ the NLSP, to have a very long life-time, exiting the detector without decaying. The other right-

handed sleptons (\tilde{e}_R and $\tilde{\mu}_R$) have a very short decay length and will decay to the $\tilde{\tau}_1$. The Higgsinos and gauginos must decay to the lightest collider-stable sparticle, i.e the $\tilde{\tau}_1$ and hence produce leptons. The lightest neutralino $\tilde{\chi}_1^0$ can be either Higgsino-like or Bino-like, and the number of resulting leptons depend on whether the neutralino went through a short ($\tilde{\chi}_1^0 \rightarrow \tilde{\tau}_1$) or long ($\tilde{\chi}_1^0 \rightarrow \tilde{l}_2 \rightarrow \tilde{\tau}_1$) decay chain.

In this work the LeptoSUSY models are focused on the production of colored particle, decaying through a cascade to a final state with two LLP candidate per event. The third generation squarks are assumed to be very heavy (~ 10 TeV), and the mass of the first two squark generations are varied in order to exclude models in a region of $(m_{\tilde{q}}, m_{\tilde{g}})$ for a fixed mass of $\tilde{\chi}_1^0$ at 400 GeV. The sleptons are long-lived and set to be degenerate with mass of 300 GeV, a value that was already excluded by previous searches [25]. Last the Gravitino is the LSP in these scenarios.

Stable Charginos

In this model a production of either $\tilde{\chi}_1^\pm \tilde{\chi}_1^0$ or $\tilde{\chi}_1^\pm \tilde{\chi}_1^\mp$ with no other supersymmetric particles accompanying the event is considered, where the lightest chargino and the lightest neutralino are nearly degenerate in their mass, therefore both are long-lived.

In this study, the chargino mass was moved up and down in a range from 100 to 800 GeV, keeping the mass splitting between the chargino and neutralino constant.

The chargino (essentially $\sim 100\%$ wino-like) was forced to be stable and the other sparticle masses were set to very high masses, outside of the LHC at $\sqrt{s} = 8$ TeV reach.

The total cross-section is mostly composed of lightest-chargino-lightest-chargino ($\sim 33\%$) and lightest-chargino-lightest-neutralino ($\sim 67\%$) direct production.

Squark R-hadrons

A simplified model considering the third generation squarks: either *stop* (\tilde{t}) or *sbottom* (\tilde{b}) as the long-lived particles forming an R-hadron bound state. These two scenarios assume the scattering of these R-hadrons in the calorimeters follows the Regge scattering model as default, where the cross-section is derived from low-energy hadron scattering and considers calculations of energy loss using the triple Regge formalism [24].

IV. The LHC and the ATLAS detector

This analysis is based on pp collision experiments conducted at the Large Hadron Collider (LHC) and measured by the ATLAS detector, located at CERN.

i. The LHC

The LHC is a ring shaped tunnel collider, of 27 km circumference, comprising two adjacent-parallel beam pipes intersecting at four points. Each beam pipe contains a proton beam, with the two beams traveling in opposite directions. The circular path of the beam is maintained by an up to ~ 8 Tesla of magnetic fields, generated by superconducting magnets immersed in liquid helium, maintaining their temperature at their superconducting phase.

A series of accelerating systems accelerate the protons as they reach to a 450 GeV when injected into the collider, and continuing accelerating till reaches an energy of 4 TeV (as to 2012). The traveling protons are accumulated into $\sim 2.8\text{k}$ bunches, each containing $\sim 115\text{ G}$ protons, maintaining 50 ns interval between the two beam collisions.

There are seven detection systems located along the collider ring, conducting several different experiment studies: ATLAS and CMS, located in opposite sides of the LHC ring, both studying high-energy phenomena involving massive particles as well as a search for physics beyond the SM, LHCb (B-physics experiments), ALICE (Study of heavy Ion collisions), LHCf (astro-particle experiments), MoEDAL (magnetic monopole research), and TOTEM (measurements of total cross-section, elastic scattering and diffraction dissociation at the LHC).

This study is focused on the search for heavy long-lived particles, based on experimental data collected by the ATLAS detector.

ii. The ATLAS detector

The ATLAS detector is a particle detection apparatus constructed at the Large Hadron Collider (LHC) [26] and is located at one of its four intersecting points. It is 44 meters long and 25 meters in diameter with a forward-backward symmetric cylindrical geometry and nearly 4π coverage in solid angle (Figure 1).

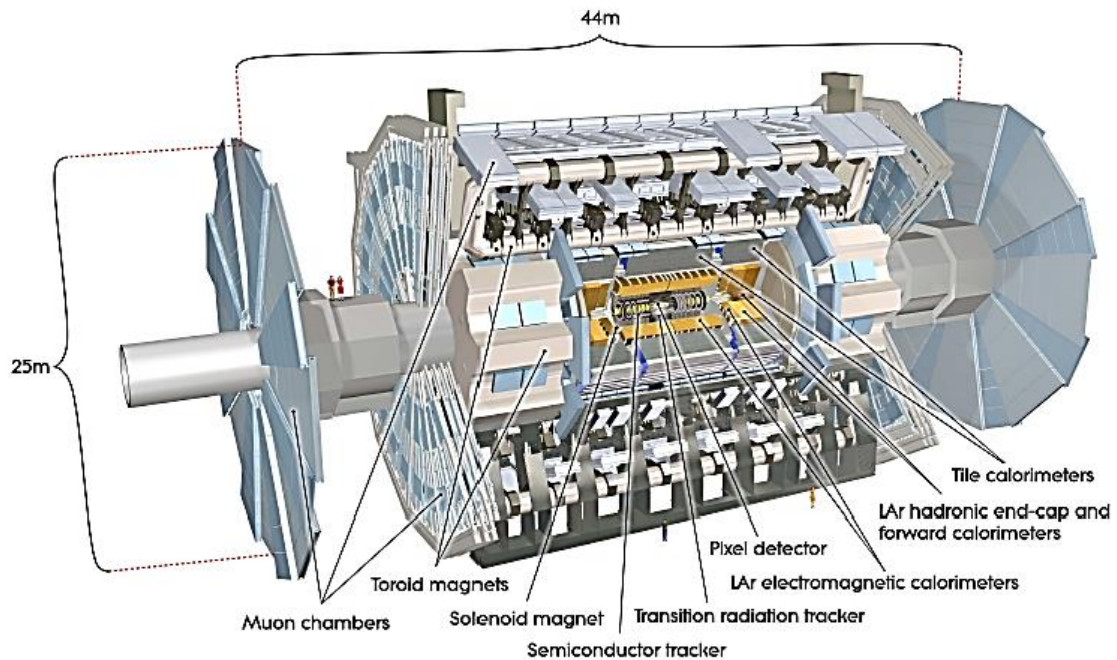


Figure 1: Cut-away view of the ATLAS detector [26]

The Interaction-Point (IP) is defined as the origin of the coordinate system. The beam travels along the z -axis line and the x - y plane is transverse to the beam axis. The azimuthal angle ϕ is measured around the z -axis, and the polar angle θ is the angle between the beam axis and the x - y plane. The transverse momentum p_T , the transverse energy E_T and the missing transverse energy (MET) E_T^{miss} are all x - y plane parameters. The pseudo-rapidity is defined as:

$$\text{Equation 2: } \eta = -\ln \left[\tan \frac{\theta}{2} \right]$$

The ATLAS detector is composed out of three main types of sub-detectors, each play a different role in the particle detection process:

- The Inner Detector (ID) – the closest detector to the IP, includes three sub-systems: a Pixel silicon detector, a silicon micro-strip detector (SCT) and a transition radiation tracker (TRT). All combined they operate to detect tracks of charged particles. The ID is immersed in magnetic field of 2T and is surrounded by the EM calorimeter.
- The calorimetric system – the middle layer of the detector, includes the Electromagnetic Calorimeter – a high-granularity liquid-argon sampling calorimeter and a hadronic calorimeter with an iron scintillator tile calorimeter in the barrel, liquid Argon calorimeter in the end-cap (HEC) and a forward calorimeter (FCal).
- The Muon Spectrometer (MS) – the outer most layer of the detector includes two systems of precision tracking chambers (The MDT and the CSC), providing momentum measurements of muons and muon-like particles. As well as two trigger chamber systems, the RPC in the barrel and the TGC in the end-caps.

ATLAS is composed of two main regions: the barrel region, includes all the sub-detector systems constructed as concentric cylindrical layers surrounding the beam axis. And the end-cap region, completes the coverage of detection by sub-detector systems mounted as disks from both sides of the barrel region, in perpendicular to the beam axis.

Following is a brief summary of the main sub-detector systems this analysis relies on:

(i) The Pixel sub-detector

The Pixel detector is the innermost sub-detector in ATLAS, i.e. the closest to the IP, providing at least three precision measurements for each track in the region $|\eta| < 2.5$ at radial distances from the beam line $R < 15\text{cm}$.

Energy loss measurements of charged particles are performed by the Pixel detector, enabling mass calculations via the following steps:

- Ionization measurements (dE/dx): A charge threshold is set for each pixel. Once the signal is above the set threshold, the Time above the Threshold (ToT) is measured. There is a good linear relation between the ToT and the charge deposition in each pixel, enabling high quality measurements of energy loss.
Once the ionization energy of the passing particle is released and deposited in the pixels, it is reconstructed by joining all relevant pixels to form a cluster and the sum of all the charge is calculated (after calibration is applied). Then the average energy loss dE/dx can be estimated for each cluster associated with the track.
- Mass measurements: Once dE/dx is estimated and the momentum has been reconstructed, particles can be identified by fitting the values to a Bethe-Bloch distribution function, and the mass can be deduced. Mass estimation

for negative charged particles and positive ones is done separately, as well as for different numbers of good clusters (nGC).

(ii) The calorimetric system

The Calorimetric system surrounding the ID, measures the energy deposited by the particle. Two types of calorimeters constructed in the ATLAS detector:

- The Electromagnetic (EM) Calorimeter - measures the energy of electrons and photons passing through, designed in accordion shape, allowing full ϕ symmetry coverage in both the barrel and end-cap regions.
- The Hadronic calorimeters - refer to both the Tile and the HEC (Hadronic end-cap) calorimeters. Both measure the energy absorbed when strongly interacting particles (mainly hadrons) lose their energy in nuclear interactions with the calorimeter material. The calorimeter has full ϕ -symmetry coverage around the beam axis. The Tile covers the barrel region while the HEC the end-cap region.

The Tile contains steel absorbers and scintillators as active medium, while both the EM and HEC calorimeter use Liquid Argon (LAr) as the active medium (hence referred to as the 'Lar' calorimeters). The Lar and the Tile calorimeters have sufficiently accurate timing to distinguish between highly relativistic SM particles and slower LLPs of interest to the searches considered in this work, and hence will be used to measure the time of flight of the candidates.

(iii) The Muon Spectrometer

The Muon Spectrometer is the most outer part of the ATLAS detector and is designed to detect charged particles exiting the Hadronic calorimeters. In the

barrel region, tracks are measured in chambers arranged in three cylindrical layers around the beam axis. In the transition and end-caps regions, the chambers are installed in planes perpendicular to the beam, also in three layers. The conceptual layout of the muon spectrometer is shown in Figure 2.

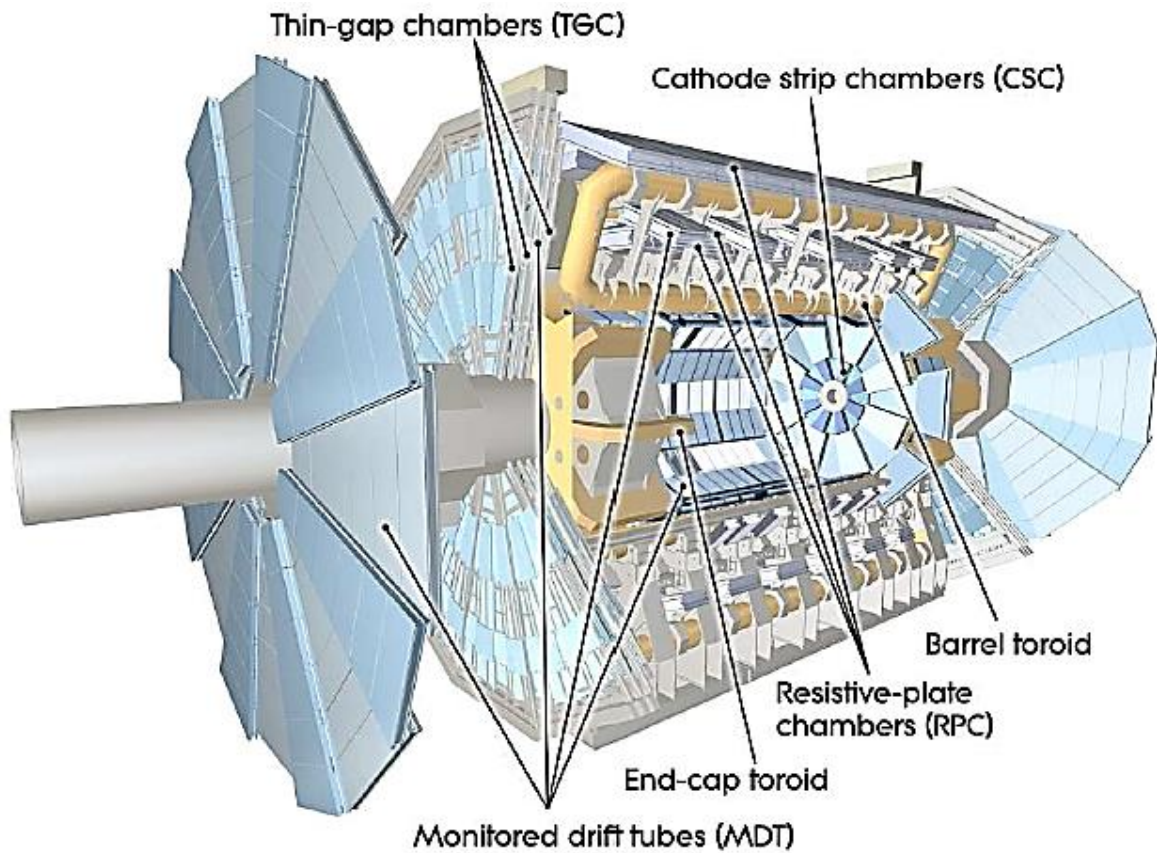


Figure 2: Cut-away view of the ATLAS muon system.

The MS is composed of 2 main systems:

1. The precision tracking chambers – measure the momentum of the particle. Monitored Drift Tube chambers (MDTs) and cover the entire $|\eta| < 2.7$ region (except in the innermost end-cap layer where their coverage is limited to $|\eta| < 2.0$). Cathode Strip Chambers (CSC) cover the inner forward region: $2 < |\eta| < 2.7$.

2. The Trigger chambers – delivering track information from the collision BC every 25 ns. They measure the coordinates of the track in both ϕ and η planes. The two trigger systems are: the Resistive Plate Chambers (RPC) covering the range $|\eta| < 1.05$, and the Thin Gap Chambers (TGC) at $1.05 < |\eta| < 2.4$.

The MDTs – are precision tracking chambers measuring the momentum of a charged particle passing in the region $|\eta| < 2.7$. They consist of drift tubes filled with Ar/CO₂ gas composition layers.

A charged particle passing through one of the tubes ionizes the gas which cause the electrons to drift towards a W₄₇/ Re wire held in $\sim 3\text{kV}$ (Figure 3). The hit position is obtained from the particle drift time measured with 0.8 ns granularity, while $R = R(t_{drift})$ represents the radius obtained from the hit position and the wire (Figure 3). Collecting hit radii from different layers and applying a tangent line between them enables reconstruction of a segment of the particle's track. Assuming a relativistic particle ($\beta = 1$), the drift time can be estimated by subtracting the expected ToF t_0 , from the measured signal time. Since LLP are expected to be slower, the measured radius will be mismeasured as larger. Larger radii can result in a badly measured segment or wrong segment direction. Further information on the MDT β estimation can be found in chapter VII.

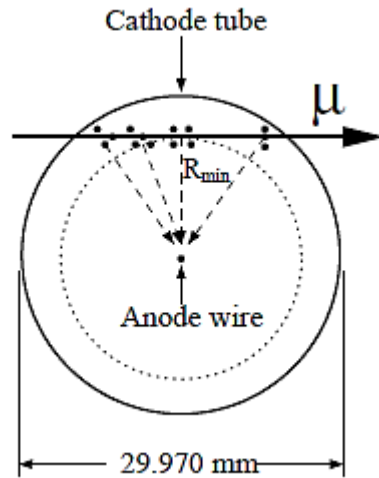


Figure 3: Cross-section of MDT tube [26].

The RPCs – are triggering the system in response to a charged particle passing through in the barrel region ($|\eta| < 1.05$). Track information is delivered within 25 ns once the trigger was set on. It is constructed as three concentric cylindrical layers around the beam axis, each layer is referred to as an RPC station. The time granularity of the RPC is 3.125 ns, permitting accurate ToF measurements. Two signals are generated upon a charge particle passing through: one measures the time and position in ϕ direction and the other in the η direction. The time measured includes both the ToF and the propagation time along the strip (the time from the point the particle passed by till the signal reached the readout electronics). Once the hit position is known in both directions, the propagation time can be subtracted and the ToF extracted.

V. Measurement Strategy

This analysis studies two cases of LLP interactions: strongly interacting LLPs and weakly interacting LLPs. There can be a difference between the two cases in terms of the detector signature such a particle would leave.

Heavy charged weakly interacting LLPs, such as charginos and sleptons are expected to interact with the detector just like heavy muons. Hence, a full track should be reconstructed all the way from the ID through the calorimeters and into to the muon spectrometer.

R-hadron LLP's detector signature cannot be anticipated in advance due to possible charge flip. Colored LLPs bound together with light quarks or gluons and then travel as a neutral color composition through the detector. While crossing the hadronic calorimeter layers, hadronic interactions of the SM particles with the calorimeter medium can change the hadronic state of the R-hadron, leading to either neutral or electrically charged states. Nuclear interactions of partons with nuclei are suppressed by the squared inverse of the mass of the parton, hence R-hadrons are modeled as a spectator accompanied by interacting light quarks and/or gluons. Therefore the expected cross-section for the interaction of R-hadrons with the detector is of the order of the ones of light quark bound states. In ATLAS, the energy loss during these interactions is expected to be small because the amount of kinetic energy available in the interacting system is small as can be seen in Figure 7.

This study considers two possible detector signatures:

1. "Combined candidates" – candidates that reconstruct to a full-track based on information from the ID, calorimeters and MS. The β of the candidate will be estimated from measured ToF of hits in all available technologies:

Calorimeters, RPC and MDT and will be combined into a combined β by a weighted average. $\beta\gamma$ deduced from the Pixel $\frac{dE}{dx}$ measurements will be used for consistency check between β from the ID and the combined β from the other technologies. The momentum will be evaluated from the candidate track in the ID only. The momentum measurement of the candidate from the MS is not exploited in this analysis. It was found to reduce the signal efficiency and give inaccurate measurements in the case of R-hadrons that reach the MS as doubly charged.

2. “ID+Calo candidates” –information based only on the ID and the calorimeters is used. The momentum is deduced from the ID track and β is estimated from either pixel $\frac{dE}{dx}$ ($\beta\gamma$) or ToF measurements from the calorimeters.

Requiring consistency of the β measurements within each technology and between the different technologies will allow for an optimized combined β resolution. Although noisy measurements are rejected when internal consistency is required, it is of high importance to ensure the measured β was indeed of a slow particle and not an artifact of the technology measuring it. Hence a consistency between the different technologies is required as well.

Once the combined β is estimated and the momentum reconstructed, the mass of the candidate can be calculated:

$$\text{Equation 3: } m = \frac{p}{\beta\gamma}.$$

The massive LLPs are expected to travel slower than SM relativistic particles, hence cutting on $\beta < 1$ will allow for background to be reduced.

As a result, the expected remaining background should be composed mainly of high momentum muons with β from the tails of the distribution.

Three factors set the quality of this search:

1. β resolution: high β resolution will result in a narrow distribution with reduced tails. If such resolution will be achieved, the background at the high mass region will be reduced as well as ensure that anomalies at high masses will be spotted easily. This is performed by applying a good calibration to the measured ToF measurements to account for time off-set of the different detector elements. Quality cuts that require a minimum number of degrees-of-freedom (DoF) and consistency between hits within each ToF measurement technology and between the different technologies play a dominant role in achieving a good β resolution.
2. Background elimination: is also performed by applying quality and consistency cuts on the estimated β . However, topological cuts on the candidate track remove background originating from cosmic rays, muons from Z or beam halo muons. Applying a final cut on the candidate's combined β to be lower than 1 will ensure a massive reduction of the background.
3. Background estimation: an accurate estimation of the background shape is required in order to claim a new discovery or set new limits. The background shape and normalization are estimated using only the data.

Furthermore, a detector signature prediction is not sufficient when dealing with reconstruction of events. The different searches will not always display the expected tracks in the events due to measurement resolutions. This was taken into consideration by defining different signal regions (SR) to cover all possible scenarios, as will be explained in further details in the selection chapter VIII.

All the slepton models considered here conserve R-parity, hence two charged LLP tracks are expected to be reconstructed and are categorized in the “two-candidate” loosely selected SR. In order not to eliminate cases where only one

candidate was properly reconstructed, another SR is defined when the LLP is tightly selected, the “one-candidate” SR.

In the stable chargino production model 33% of all events are expected to be a $\tilde{\chi}_1^\pm \tilde{\chi}_1^\mp$ direct production, while the rest 67% should be a $\tilde{\chi}_1^\pm \tilde{\chi}_1^0$ production. Since the mass splitting between the $\tilde{\chi}_1^\pm$ and the $\tilde{\chi}_1^0$ is set to be negligible, a $\tilde{\chi}_1^\pm \tilde{\chi}_1^0$ event will result in one reconstructed charged LLP and a large MET. To account for these two scenarios and the possibility of a $\tilde{\chi}_1^\pm \tilde{\chi}_1^\mp$ with only one charged LLP reconstructed properly, three SRs are defined: “two-candidate” SR for loosely selected $\tilde{\chi}_1^\pm \tilde{\chi}_1^\mp$, “one-loose-candidate” SR loosely selected with a large cut on the MET $E_T^{miss} > 100\text{GeV}$ for the $\tilde{\chi}_1^\pm \tilde{\chi}_1^0$ production case, and last, a “one-candidate” tightly selected for a case of only one reconstructed charged LLP.

The SRs for both sleptons and chargino searches are exclusively selected, in the sense that only if they fail to pass the two-candidate SR they will be tested for the one-candidate SR.

Due to possible charge flip scenarios in the R-Hadrons case, a “full-detector” search is defined to account for either a full detector track (ID, Calo and MS) or half-track (ID+ Calo) information only. These options cover the two cases where the R-hadron is produced and remained electrically charged while crossing the detector, and the case where it becomes neutral when exiting the hadronic calorimeter. In this SR selection the candidates are selected inclusively. First searching for a combined track candidate and only if it was not found, an ID+ Calo candidate is selected. The case where the R-hadron is produced as neutral and becomes charged while exiting the hadronic calorimeter is not investigated in this study, mainly due to low quality of the reconstructed tracks and lack of enough background statistics in this case. Also, the case of neutral R-hadron in all

detector stations is ignored. Table 3 lists the different searches included in this study, the mass range of the LLPs and the defined SRs.

Search	Mass Range (GeV)	Signal-Region	Signature/Requirements
GMSB	175–500	Two-candidate	Two loose combined candidates
		One-candidate	One tight combined candidate
LeptoSUSY	600–3000	Two-candidate	Two loose combined candidates
		One-candidate	One tight combined candidate
Charginos	100–800	Two-candidate	Two loose combined candidates
		One-loose-candidate	One loose combined candidate plus E_T^{miss}
		One-candidate	One tight combined candidate
R-hadrons	300–1700	One-candidate	One preferably combined candidate. In case missing, one ID_Calo candidate selection. *In case of multi-combined candidates, random choice of a candidate will be taken.

Table 3: Overview of all searches, mass ranges and signal regions.

The background in all searches will be estimated for the mass distribution of the candidates, separately for each search (sleptons, charginos and R-hadrons) and SR and is completely data driven.

Simulated samples are used in this search for two main purposes: As mentioned previously, the background for these searches is expected to be composed mainly of high-p muons with badly measured β . Therefore simulation of $Z \rightarrow \mu\mu$ events is

suitable for calibration and smearing studies as they can be easily compared with $Z \rightarrow \mu\mu$ data events collected. β measurements of the simulated events are compared with β measurements of the data, and adjustment of the smearing of the generated hit times according to the ones in the data sample is done in order to account for the ToF measurement resolution. The smearing factors deduced from this procedure are implemented on simulated signal samples.

Signal samples for the different signal searches: GMSB, LeptoSUSY, Charginos and R-hadrons are used for signal efficiency studies, and for optimization of the selection cuts to ensure highest signal efficiency possible with minimum background.

VI. Data and simulated samples

i. Data

The total integrated luminosity collected by the ATLAS detector in 2012 runs was 20.3 fb^{-1} . The study presented here is based on data from 2012 collisions with a total integrated luminosity of 19.1 fb^{-1} reprocessed in ATLAS official reprocessing. The reason for the smaller integrated luminosity considered is due to a technical failure to run over all the events in the grid. Yet, the difference is negligible and would not change the results reported in this study.

Another data sample of mainly $Z \rightarrow \mu\mu$ events collected in 2012 runs with a total integrated luminosity of 19.8 fb^{-1} is used as a control sample.

ii. Simulated Monte-Carlo (MC) Samples

Simulated samples play a crucial role in this type of search. MC samples that are properly simulated can ensure an accurate estimation of the expected signal efficiency in the different scenarios, and in case of no discovery setting limits.

The data taking runs in ATLAS may differ one from the other due to changes applied in the trigger menus to account for the increase in luminosity. In order to reflect these changes in the simulated MC, the samples are divided into sets and each set represents a number of data taking periods. In each set the distribution of pile-up events, the detector conditions and trigger changes, matches the conditions in the different data taking periods. To make sure that the MC sets represents accurately the fraction of the data collected in each run, re-weighting is applied using a PileupReweighting-00-02-11 ATLAS package.

(i) Simulated Background Samples

Simulated sample of 4 million $Z \rightarrow \mu\mu$ events generated with PHYTHIA6² [27] is used for calculating the smearing of the hit times according to what is observed in the $Z \rightarrow \mu\mu$ data sample and by comparing time and beta distributions between $Z \rightarrow \mu\mu$ data and MC validate the hit time smearing procedure applied to the signal simulated samples.

(ii) Simulated Signal Samples

GMSB Simulated Samples

A range of simulated GMSB samples were generated using HERWIG++ [28] for the study of a $\tilde{\tau}$ NLSP in the mass range between 175–500GeV. The fixed-value parameters of the GMSB model are the following: $N_5=3$ the number of supermultiplets in the messenger sector, $M_{\text{messenger}}=250\text{TeV}$ the messenger mass scale, $\text{sign}(\mu)=1$ the sign of the Higgsino mass, and $C_{\text{grav}}=5000$ the scale factor of the Gravitino mass which determines the NLSP lifetime (it is set high enough to ensure the NLSP will not decay within the ATLAS detector).

Other parameters that vary from one mass point to another are: $\tan(\beta)$, the ratio between the vacuum expectation values of the two Higgs doublets in a range between 10 and 50 in intervals of 10. The effective SUSY breaking scale Λ is varied between 80TeV and 160TeV, in intervals of 10TeV. The variations in $\tan(\beta)$ set the mass splitting between the $\tilde{\tau}_1$ and the other SUSY particles. Increasing $\tan(\beta)$ will reduce the $\tilde{\tau}_1$ mass while increasing the mass splitting between the $\tilde{\tau}_1$ and the other s-particles. Increasing Λ will increase the masses of all SUSY

² PHYTHIA6 is a program for the generation of high-energy physics events and allows for description of collisions at high energies between elementary particles.

particles, which will result in a decrease of the cross-section (higher mass s-particles, especially squarks and gluinos are pushed higher in the TeV scale and are then less likely to be produced). The right-handed sleptons ($\tilde{e}, \tilde{\mu}$) are lighter than the left-handed sleptons and are heavier than the $\tilde{\tau}_1$ mass by 0.75–90 GeV. The light neutralino masses vary from 328–709 GeV and the chargino masses from 540–940 GeV. With these model parameters the resulted mass of the squarks and gluinos is above 1 TeV in all samples.

LeptoSUSY Simulated Samples

The LeptoSUSY samples are simulated in MADGRAPH [29] with BRIDGE [30] for decaying the quarks, and PHYTHIA8 [31] for parton shower.

The sleptons are considered as long-lived within the ATLAS detector, and their masses are fixed to 300 GeV.

The masses of the neutralinos and charginos are decoupled, hence are not within the LHC reach with the exception of the lightest neutralino $\tilde{\chi}_1^0$ that its mass is fixed to 400 GeV.

The third generation squarks (\tilde{t}, \tilde{b}) are also assumed to be too heavy to be produced in the LHC, while the first and second generation squarks and gluinos have mass at the range of 600–3000 GeV.

Charginos Simulated Samples

Samples of long-lived charginos were generated using HERWIG++ [28] assuming the lightest neutralino and chargino are nearly mass degenerate. The chargino is the NLSP and the neutralino the LSP. In case a chargino is produced it is unlikely that it will decay to the neutralino, due to the small mass splitting between the two. The mass splitting is set to 0.14 GeV and is fixed for all mass points investigated in this study.

All other SUSY particle's mass were set to very high mass values, beyond the LHC production reach, to ensure scenarios of either $\tilde{\chi}_1^\pm \tilde{\chi}_1^\mp$ or $\tilde{\chi}_1^\pm \tilde{\chi}_1^0$ production only. The total cross-section is mostly composed of $\tilde{\chi}_1^\pm \tilde{\chi}_1^\mp$ ($\sim 33\%$) and $\tilde{\chi}_1^\pm \tilde{\chi}_1^0$ ($\sim 67\%$) direct production.

R-hadron Simulated Samples

Simulation of pair production of gluinos, stops and sbottoms were simulated in PHYTHIA6 [27] with a full detector simulation, where the interactions with matter are handled by GEANT4³ [32].

The gluino R-hadron is studied under the context of the Split SUSY model where the gluino is long-lived due to R-parity conservation and the assumption that the other squarks mass is higher. The interactions of such R-hadron with matter is referred to as the 'generic model'. 10% of the events are of gluino-ball scenarios, where a gluino and a gluon bounds together forming a neutrally electrically charge state.

The cases of long-lived stop or sbottom interacting with matter according to a 'triple Regge' interaction are studied under the same conditions and the same analysis strategy is applied as in the gluino R-hadron case.

All R-hadron scenarios considered here are studied with LLP at mass range between 300-1700GeV.

³ GEANT4 is a tool package used for simulation of particles passage through matter. The simulation consider variety of sources that can affect the way the particle scatters-off a nuclei (tracking, physics models, etc...) The physical process included in this package are: electromagnetic, hadronic and optical for a large set of particles, materials and elements over a wide energy scale (250 eV up to the TeV scale).

VII. Mass reconstruction

In this study the mass is calculated by the ratio between the momentum and $\beta\gamma$:

(Equation 3) $m = \frac{p}{\beta\gamma}$ where β is estimated in two ways.

β estimated from ToF measurements of available technologies with good time resolution (Calorimeters, RPCs and MDTs) is used for the case of combined candidates, i.e. with a full track. The mass calculations that considers a ToF measurement based β is referred to as m_β in this study and is used for the sleptons, charginos and R-hadrons.

For the R-hadron case, where there is no guarantee for a full-track candidate but sometimes an ID+ Calo candidate only, there is also a mass calculation based on $\beta\gamma$ calculations deduced from the Pixel $\frac{dE}{dx}$ measurements. The mass calculations that considers the Pixel measurement based $\beta\gamma$ is referred to as $m_{\beta\gamma}$ in this study and is used for R-hadron scenarios only. As for the ID+ Calo case, the information comes only from the ID and the Calorimeters, hence a measurement based on just one out of the two might not be accurate, and combining the β from the ToF Calo measurements and $\beta\gamma$ from the Pixel is not possible as one technology measures energy loss while the other relay on timing of the hits. Hence, for the R-hadron case, the mass is estimated twice, once for m_β and once for $m_{\beta\gamma}$ and both mass estimations are required to be above a certain mass cut to pass into the SR.

i. Mass from $\frac{dE}{dx}$ measurement

The hits from the Pixel detector contain the physical coordinate of the signal and the time-over-threshold (ToT) associated with it. The maximum measurable ToT

value corresponds to approximately 8.5 times the average charge released by the minimum ionizing particle (MIP). Above this value the measurement is lost.

The energy deposit by a particle traversing the Pixel layers is rarely confined to a single pixel, hence neighboring pixels are joint together to form clusters and the charge of each cluster is calculated by summing up the charges of all pixels.

The specific energy loss $\frac{dE}{dX}$, is defined as an average of the individual cluster charge measurements for the clusters associated with the track. The energy deposited by a track in each cluster follows an asymmetric Landau distribution. The average is composed of charge measurements from three clusters, yet in order to avoid bias, the clusters with the highest charge are removed from the calculation.

The mass of a slow charged particle can be measured by fitting each $\frac{dE}{dX}$ and momentum measurement to an empirical Bethe-Bloch function, and from that deduce the $\beta\gamma$ value. Within the ToT and MIP boundaries, the possible range of $\beta\gamma$ is between 0.2 and 1.5 respectively. The particle identification method described in [33] uses five-parameter function to describe how the most probable value of specific energy loss $\mathcal{M}_{\frac{dE}{dX}}$ depends on $\beta\gamma$:

$$\text{Equation 4: } \mathcal{M}_{\frac{dE}{dX}} = \frac{p_1}{\beta^{p_3}} \ln(1 + (p_2\beta\gamma)^{p_5}) - p_4$$

Figure 4 (left) shows how $\mathcal{M}_{\frac{dE}{dX}}$ overlaps data for low momentum tracks. Figure 4 (right) shows the simulated Pixel $\frac{dE}{dX}$ spectra for singly-charged hypothetical R-hadrons for several mass points. The most probable value of $\frac{dE}{dX}$ for MIPs is about $1.2 \text{ MeVg}^{-1}\text{cm}^2$ with a slight η dependence. $\beta\gamma$ is obtained by inverting the above equation, then for all the tracks with a reconstructed momentum p and $\frac{dE}{dX}$ above the value of the MIP the mass $m_{\beta\gamma}$ is estimated.

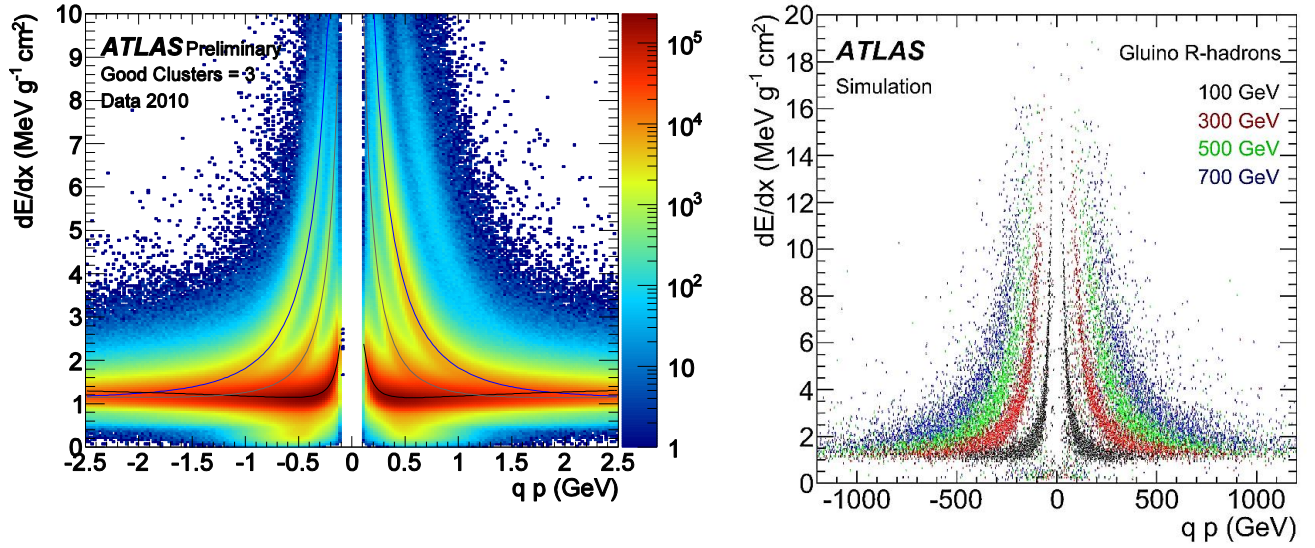


Figure 4: Left: Distribution of $\frac{dE}{dx}$ vs. charge times momentum for minimum bias collisions in a data sample from 2010. Right: Simulated distribution of specific energy loss vs. momentum for singly-charged hypothetical R-hadrons of various masses.

ii. Mass from ToF measurements

The calorimeters (LAr as EM calorimeter, Tile and HEC as hadronic calorimeters), RPCs and MDTs are used for the time measurement to estimate the β of a particle. These sub-detectors have good timing resolution and allow to distinguish between relativistic SM particles and slower LLPs. However due to differences in performance between the different systems, a calibration of the hit times is required in case of off-sets and later a combining by a weighted average of the different β estimations into a combined β .

(i) Measurement

Once the hits in a particle's trajectory have been reconstructed, the location of the hits and the ToF from each technology can be used to calculate the β of the particle. A weighted average of the estimated β 's from the different sub-system is calculated. The uncertainty on the hits location is relatively negligible, yet the errors on the ToF measurements are not and they are distributed in a Gaussian shape, hence the β 's will be estimated in the form of β^{-1} :

$$\text{Equation 5: } \beta_{reco}^{-1} = \frac{\left(\sum_{i=0}^N \frac{\beta_i^{-1}}{\left(\frac{\sigma^2}{\beta_i^{-1}} \right)} \right)}{\left(\sum_{i=0}^N \frac{1}{\left(\frac{\sigma^2}{\beta_i^{-1}} \right)} \right)}$$

where the β of the corresponding ToF of hit i is divided by its distance:

$$\text{Equation 6: } \beta_i^{-1} = \frac{ToF_i}{d_i}$$

and $\sigma_{\beta_i^{-1}}$ is the time resolution of hit i divided by its distance:

$$\text{Equation 7: } \sigma_{\beta_i^{-1}}^2 = \frac{1}{\sum_{i=0}^N \left(\frac{1}{\frac{\sigma^2}{\beta_i^{-1}}} \right)}$$

and β is calculated as the invers of β^{-1} . The error on β is given by the error propagation as:

$$\text{Equation 8: } \sigma_{\beta} = \beta^2 \sigma_{\beta^{-1}}$$

and σ^{β} is proportional to β . As a result, for small β the error is smaller as well and for a given resolution on the time measurement a slower particle has a better β resolution.

(ii) ToF measurement calibration

The increase in events statistics and on-going efforts of the ATLAS collaboration have improved the timing calibration of the sub-detectors in the 2012 data with respect to previous years. Yet, an optimization of the timing resolutions is still required due to sensitivity of the ToF measurement to relative offsets in the time calibration between the different detector elements.

In a perfectly calibrated detector, relativistic particle such as energetic muon coming from the IP will reach the detector at $t_0 = 0$. The t_0 distributions of the different sub-detectors are measured for muons from a data sample enriched with $Z \rightarrow \mu\mu$ events. The means of these distributions are used to correct the calibration of the timing, by performing a shift to the measured t_0 's and their widths are used as the resolution of the time measurement in the β^{-1} average.

Smearing the $Z \rightarrow \mu\mu$ simulated MC t_0 distribution according to the $Z \rightarrow \mu\mu$ data t_0 distribution will simulate the real detector conditions in the MC sample and the resolution widths will be similar.

LHC-ATLAS phase shift correction

The shift in the mean of the t_0 distribution from zero in the calorimeters and RPCs was found to be run dependent. This shift presumably comes from a misalignment in the ATLAS and LHC clocks caused by weather influence on the fiber that

synchronizes between the two clocks. A correction has been applied based on the average of the calorimeter measurements.

Figure 5 shows the calorimeter time shift average per run as a function of run number.

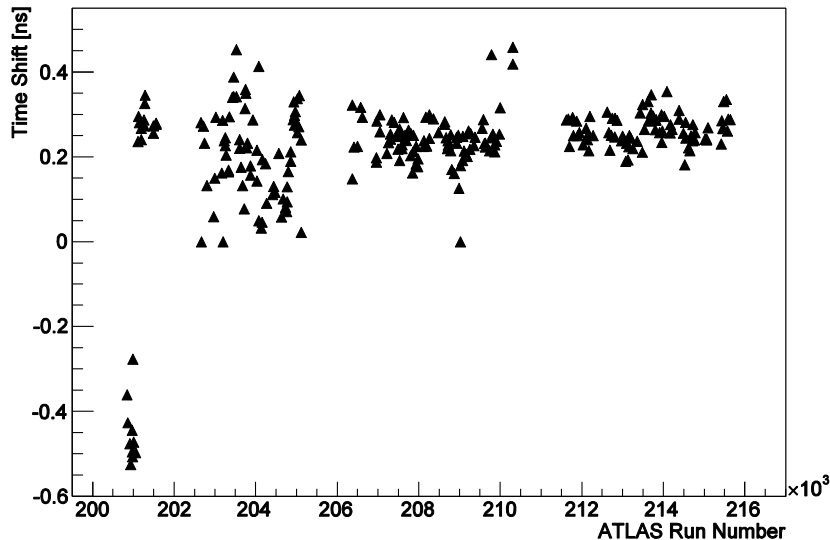


Figure 5: The relative shift of all calorimeter cell time measurements averaged per run as a function of run-number before any calibration is performed.

Calorimeter timing calibration

The t_0 distribution depends strongly on the calorimeter layer and the energy deposition on the cells. Deriving calibration constants to account for these dependencies, the data from a control sample ($Z \rightarrow \mu\mu$) is divided into energy-layer bins, from which the mean and width of the t_0 is extracted. Calibration correction to the data and the smearing of the MC is applied to the same energy-layer bins. Figure 6 shows a comparison between un-calibrated and calibrated cell times and β , while Figure 7 exhibits a comparison of the expected energy deposit by the different LLPs vs. muons in the calorimeters.

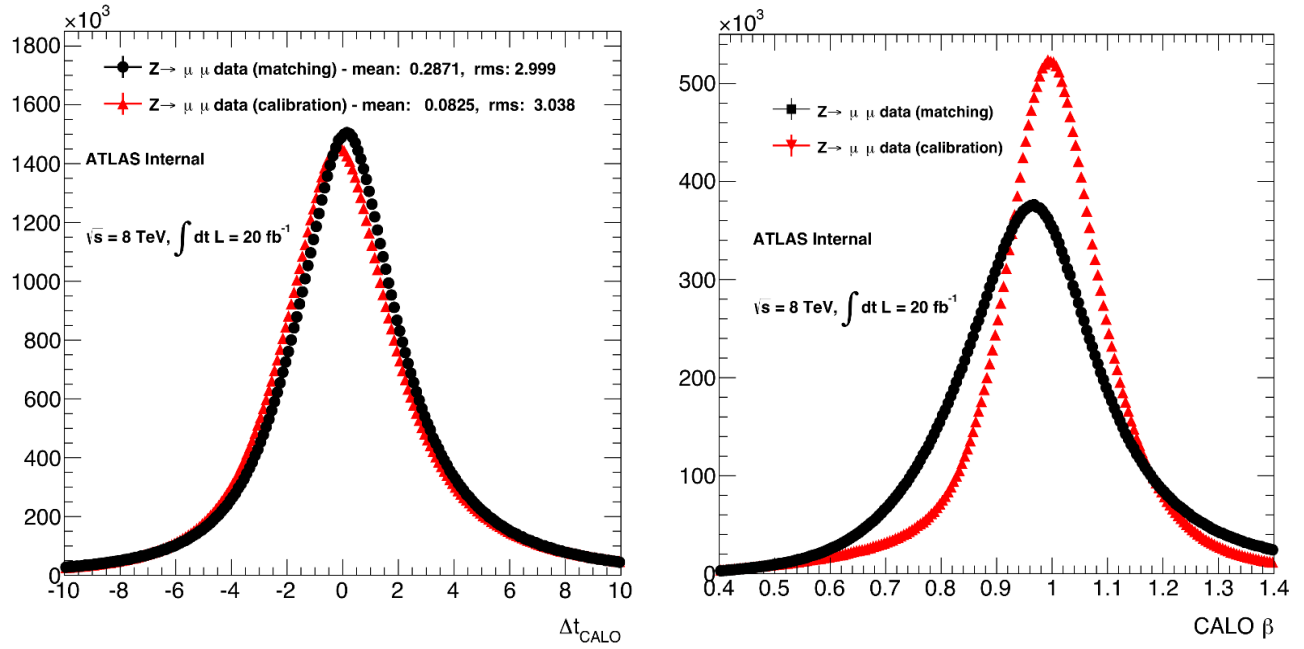


Figure 6: A comparison of calorimeter cell times (left) and the reconstructed β (right) before (black) and after (red) calibration.

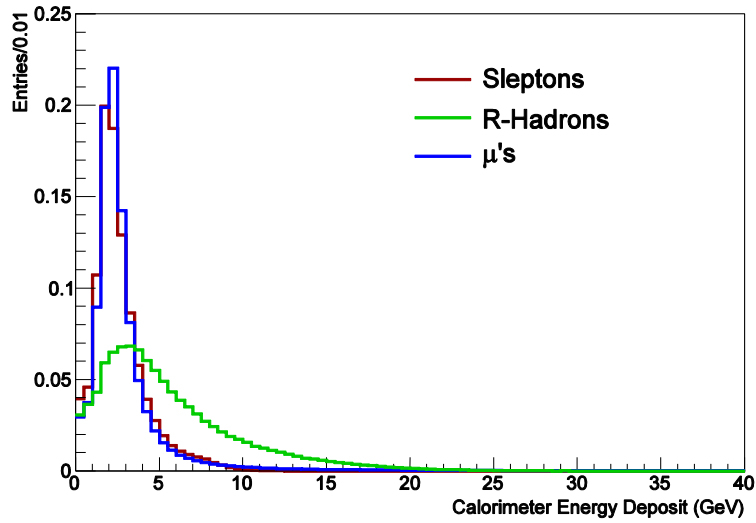


Figure 7: A comparison of the calorimeter energy deposits for sleptons (red), R-hadrons (green) and muons (blue).

Muon Spectrometer technologies timing calibration

The calibration for the RPC technology is performed by extracting 372K constants to correct the calibration timing of the RPC strips.

For the MDT, the calibration is performed by extracting approximately 32K pairs of constants for correction of corresponding timing reading in the readout boards.

Figure 8 shows the hit times and β measurement distributions for muons from $Z \rightarrow \mu\mu$ events before and after calibration for the RPC and MDT technologies.

(iii) Calibration of σ_β scale

Once a weighted average of β and its errors, σ_β , have been obtained, a final calibration of σ_β is performed. It has been investigated how well the calculated errors describe the width of the β distribution. Histogram of pull values, i.e.

$$\text{Equation 9: } \frac{(1-\frac{1}{\beta})}{\sigma(1-\frac{1}{\beta})}$$

are filled in bins of β and η to correct for any dependence as a function of these variables. The width values from the histograms are used directly as scaling factors of σ_β . Figure 8 shows the pulls of the β measurement in different sub-detectors.

(iv) Smearing simulated MC hit time measurements

The simulation of events in MC does not describe accurately the distribution of the real-time measurements. Hence smearing of the hit times according to the distribution observed in the data is an important step in the analysis when a realistic estimation of a signal within all the measured background is required. The procedure of smearing the simulated hit times considers separate smearing factors for the different detectors measuring the ToF and their elements.

For the calorimeters and the MDT technologies each hit is smeared by the time resolution observed in the detector element where it was measured.

For the RPC technology the simulation does not include an error on the measurement, and one has to model correctly the digitization changes coming from the time resolution. Further details on the RPC simulation constraints and overcoming them can be found in chapters VIII (section (i)) and X (section (i)).

(v) Internal consistency of a β measurement

The β measurements within each technology are required to be consistent in order to remove noisy measurements.

For the calorimeters, the consistency is checked by calculating the χ^2 distribution of the average β^{-1} : The square sum of each individual β_i^{-1} measurement relative to the average β^{-1} weighted with the error on the measurement $\sigma_{\beta_i^{-1}}$. In case the χ^2 probability for the number of DoF is found to be below 0.001, the measurement is rejected.

For the MS technologies, i.e. RPC and MDT a cut is applied on the R.M.S of the β_i^{-1} measurement.

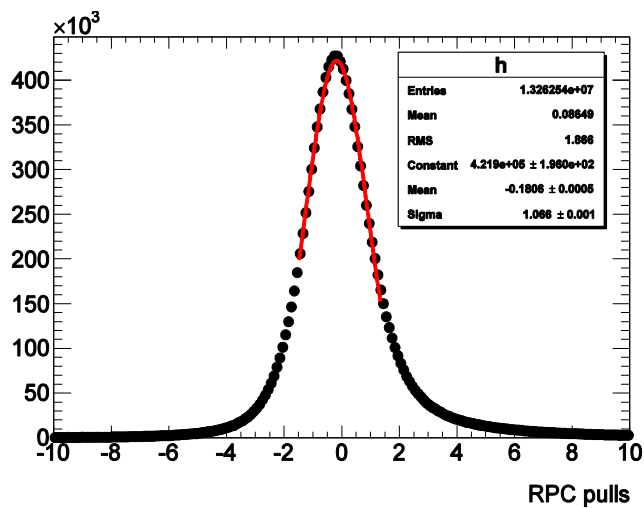
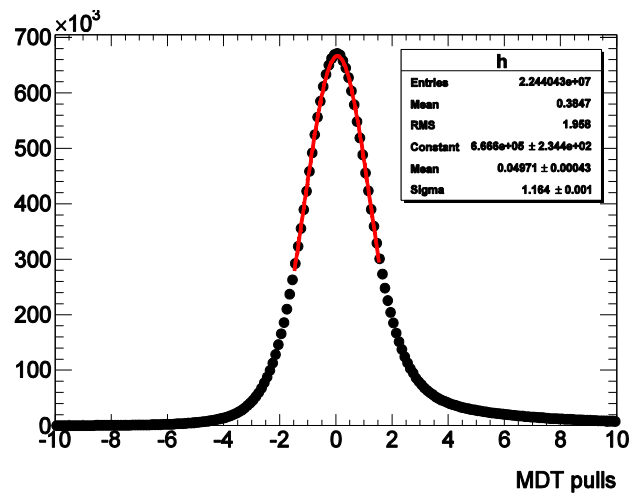
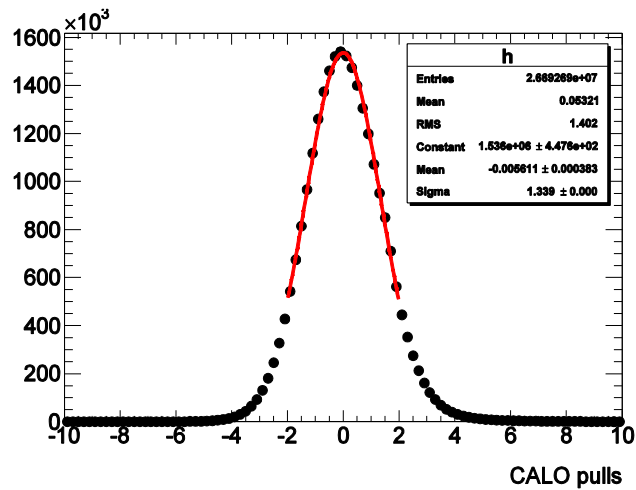


Figure 8: Pulls of the β measurement for muons from data in the calorimeters (top), the MDTs (middle) and the RPCs (bottom).

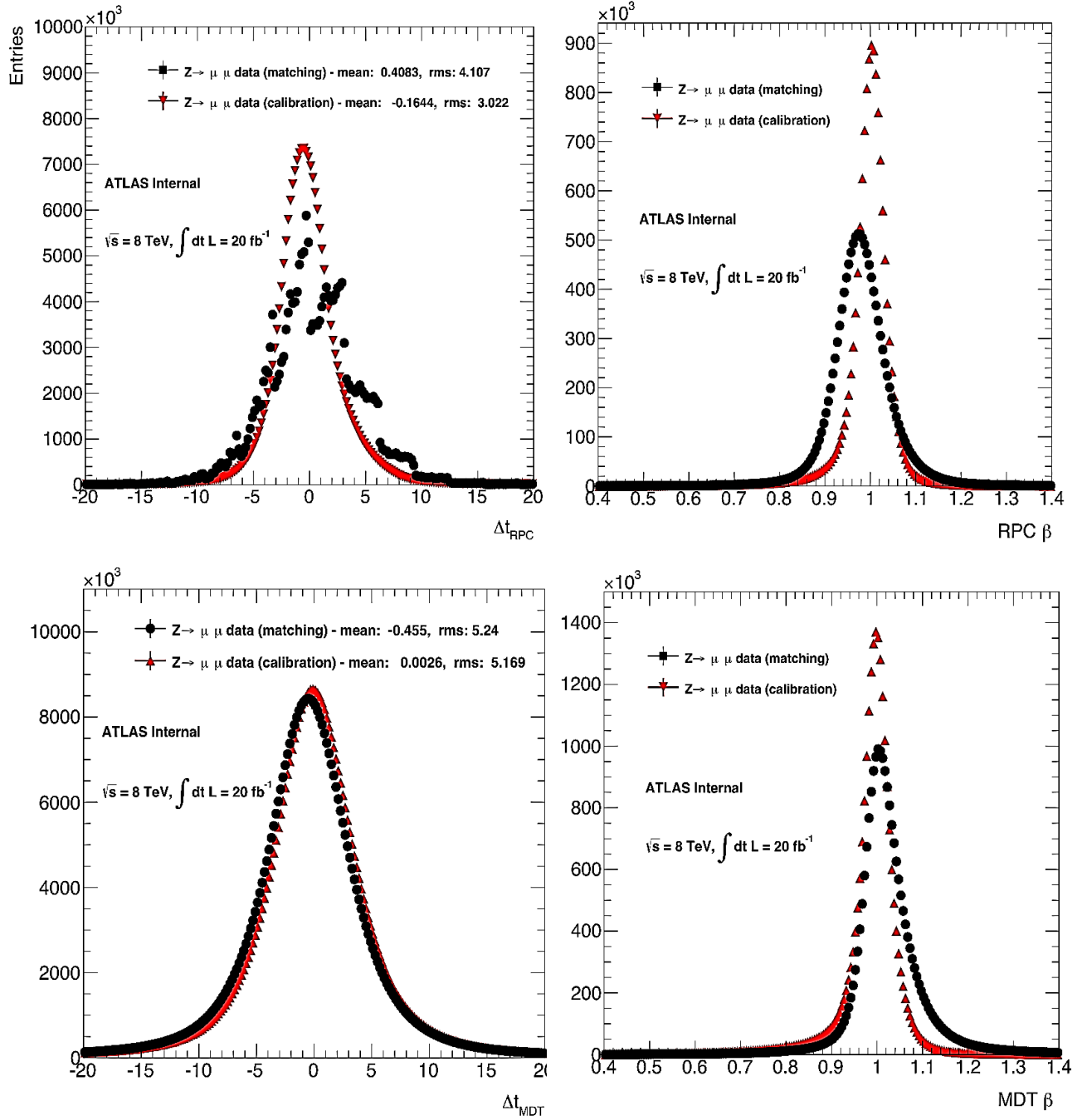


Figure 9: Hit times (left) and β measurement distribution (right) for $Z \rightarrow \mu\mu$ events before (black) and after (red) calibration for the RPC (top) and MDT (bottom).

(vi) Combining β measurements

Only β measurements that were found to be consistent in each technology and between the different technologies are combined in a weighted average to provide a final β measurement of the candidate, while the weights are obtained from the calculated error of each measurement. A consistency is also required between the combined β and $\beta\gamma$ from Pixel $\frac{dE}{dX}$ measurements. Figure 10 shows the β measurement distribution obtained from the calorimeters only (left) and a combined β measurement (right) for selected $Z \rightarrow \mu\mu$ events in data and smeared MC. The combined β measurements is distributed nicely around 1 ($\bar{\beta} = 0.999$) in both data and MC distributions, with a fine and relatively narrow distribution ($\sigma_\beta = 0.0232$ in the data, and $\sigma_\beta = 0.0237$ in MC). The results of the smearing mechanism can be seen in this figure, exhibiting almost equal distributions of the data and MC.

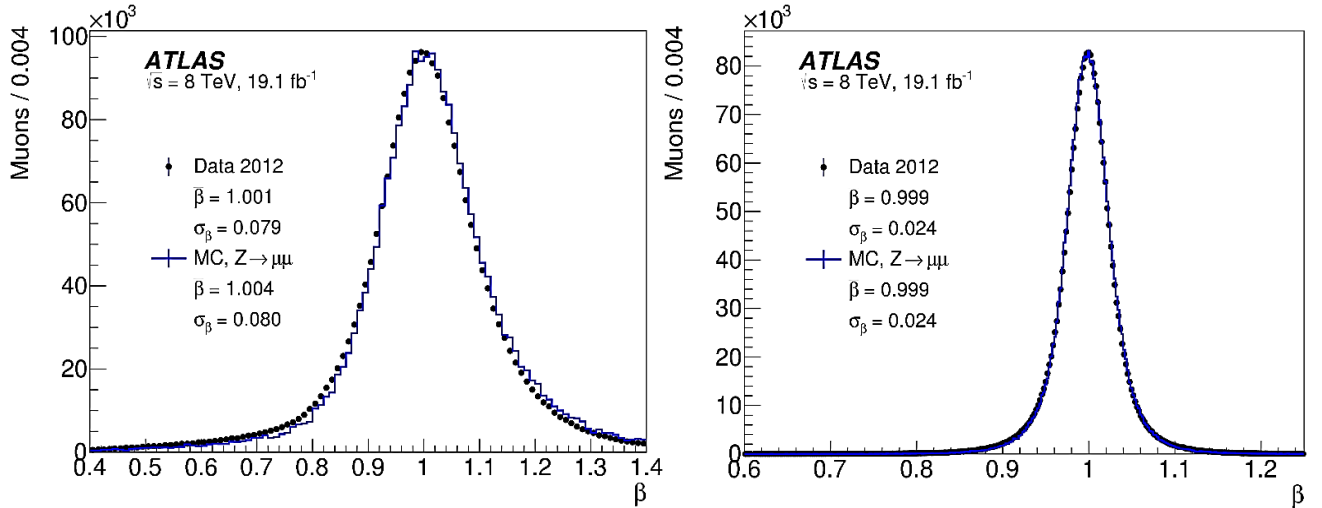


Figure 10: Distribution of the β from the calorimeter measurements (left) and the combined β (right) obtained for selected $Z \rightarrow \mu\mu$ events in MC before (red) and after (blue) the smearing procedure.

VIII. Selection

This analysis relies on three stages of selection: An ‘on-line’ selection of events to be kept for analysis and ‘off-line’ selection of events and the candidates within these events. This narrows further the number of events that demonstrate a reconstructed LLP of the SR detector signature being studied.

i. Online event selection – Triggers

All searches in this study include only events that passed either the unrescaled single-muon or missing-transvers-momentum trigger chains to ensure maximum trigger efficiency possible.

(i) Single-Muon trigger

The single-muon trigger chains included require p_T threshold above 24GeV, low enough with respect to the off-line selection cut on the p_T : for the full track candidates in the R-hadrons search the cut is above 50GeV while for the other searches the cut is above 70GeV.

Level-1 muon triggers are accepted and passed to the high-level trigger (HLT) only if assigned to the collision bunch-crossing (BC). Later triggers due to late arrival of the particles are lost at the HLT stage.

The majority of candidates in the data are in-time muons, hence late arrival particles are coming mostly from miss-measurements. The trigger efficiency for late arrival particles cannot be estimated from the data due to low statistics in this region. Simulated signal samples are used for the trigger efficiency studies of slow massive LLPs, yet the accuracy of this estimation depends directly on the exact timing implementation in the simulation and needs to be compatible with what is described in the data.

The Level-1 trigger simulation is a detailed emulation of the trigger electronics chain and would give the same result as the online electronics, given the same input data.

The two Level-1 muon trigger systems are the RPC in the barrel and the TGC in the end-cap regions of the ATLAS detector.

The TGC digitization of the time distribution is based on a detailed study test-beam, and cable delays are compensated accurately in the electronics. As a result, the Level-1 trigger simulation and the data were observed to correspond well to each other.

For the RPC the measured times that go into the emulation have some difference between the data and the MC. Cables in the hardware that transmit the signals to the electronics are transmitting with a small delay that should be compensated by the electronics delay taken in account, yet the compensation is not perfect.

Furthermore, in the simulation the alignment of the particle times within the BC is shifted by 5nsec compared to the data, and the electronic jitter and signal creation jitter are underestimated.

The calibration of the hit times in the RPC considers a fix for this delay, yet the simulation of the signal MC can be biased as a result of this imperfection, and the signal efficiency of the trigger estimated as higher than it should be.

In order to overcome this issue, we have assessed a systematic error on the RPC trigger efficiency, by smearing the simulated MC hit times to be distributed as uncalibrated data, and re-estimate the trigger efficiency on the signal.

When tested on GMSB simulated samples, the single-muon trigger chains were found to be efficient. GMSB signatures can contain two typically high- β LLPs that reach the MS and additional muons stemming from neutralino decays, both can

trigger the event. Figure 11 (right) exhibits the muon trigger efficiency as a function of the β of the particle that triggered the event. The lower- β particles can still be found if a higher- β particle triggered the event as can be seen in Figure 11 (left).

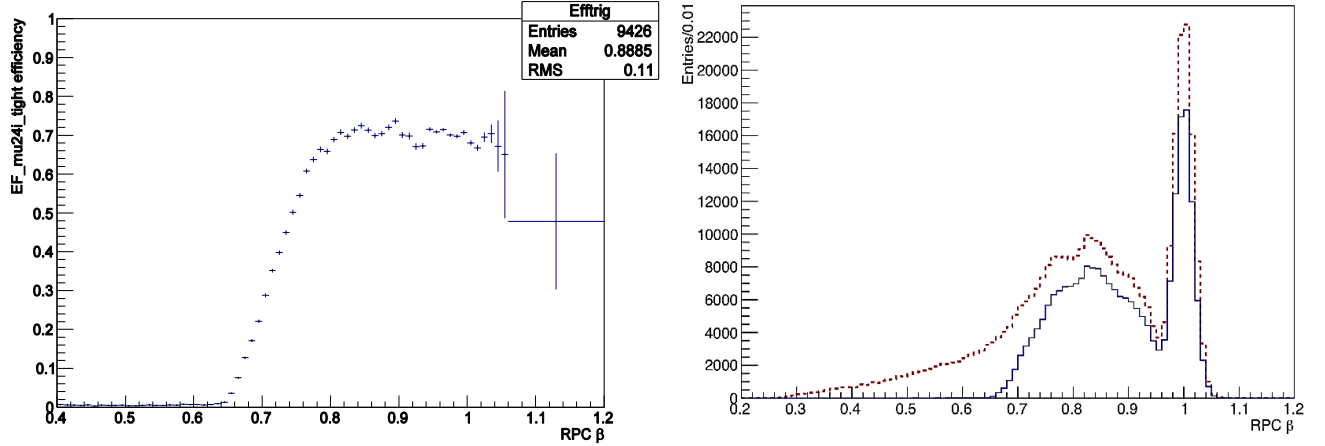


Figure 11: Left: Muon trigger efficiency in simulated GMSB events as a function of the trigger hit β (after correcting the mean with respect to BC according to the data). Right: Distribution of β for trigger candidates (line) and for all candidates in the event (points) passing the trigger. Candidates with β below the trigger threshold are found in triggered events when there is another higher- β particle that triggered the event.

The estimated muon-trigger efficiency for GMSB events range between 65–85%. When tested on Chargino simulated events the efficiency was found to be between 24–67%, lower than in the slepton case. This is a result of lack of muons in the chargino production scenario that includes either $\tilde{\chi}_1^+ \tilde{\chi}_1^-$ or $\tilde{\chi}_1^+ \tilde{\chi}_1^0$, and in the later case which is $\sim 67\%$ of all the events only one candidate can trigger the event. For lower mass charginos, the trigger efficiency is higher as they expected to travel in higher- β with respect to the higher mass charginos. Last, for the R-hadron simulation the efficiency is estimated to be even lower (less than 35% and

lower for higher masses) as a result the relatively low- β and flip charge scenarios when the R-hadron reaches the MS neutral.

(ii) Missing transvers momentum trigger

Events containing LLPs sometimes contain high- p_T jets from QCD initial-state radiation (ISR). The energy deposit of a LLP in the calorimeters is relatively modest, at the scale of the energy deposit of a muon as can be seen in Figure 7, as a result the E_T^{miss} can be large for that event.

In the stable chargino production scenario, the contribution to the E_T^{miss} can result from ISR. The long-lived neutralinos escaping detection and only later on are reconstructed as E_T^{miss} . While in the sleptons scenario, the large E_T^{miss} can come from EW production of charginos or sleptons decaying to stau and a neutrino. Jets in the final-state-radiation (FSR) are negligible in both Chargino and slepton scenarios.

The MET trigger chains included in this analysis are of p_T threshold above 60GeV for the R-hadron search and above 70GeV for the other searches.

The MET trigger efficiency is not reduced due to slow particles late to arrive, as in the muon trigger case.

(iii) Total trigger efficiency

For all searches a logical OR of the MET or Muon triggers is applied in the selected events.

In the slepton search, the addition of the MET trigger to the event selection increases the efficiency of signal events to be selected. The MET trigger includes events of late arrival particles that did not fire the muon trigger because they did not arrive on time with the collision BC. The total efficiency is reduced with increasing mass of the stable slepton. This is a result of the late arrival of particles

to the MS that the MET trigger did not manage to include due to low E_T^{miss} in the event. Figure 12 shows the trigger efficiency obtained for GMSB events as a function of the stau mass.

Figure 13 shows the trigger efficiency for a stable slepton of fixed mass at 300GeV within the LeptoSUSY models as a function of the squark (left) and gluino (right) masses. In these plots the same squark (gluino) mass can appear more than once for different efficiencies measured. This is a result of studying models with one squark (gluino) mass with different gluino (squark) masses.

In the stable chargino model scenario, the trigger efficiency is demonstrated in Figure 14 (left). The increase in the MET trigger efficiency with increase in the chargino mass is a reflection of the increase in the neutralino mass as well (as they are nearly mass degenerate).

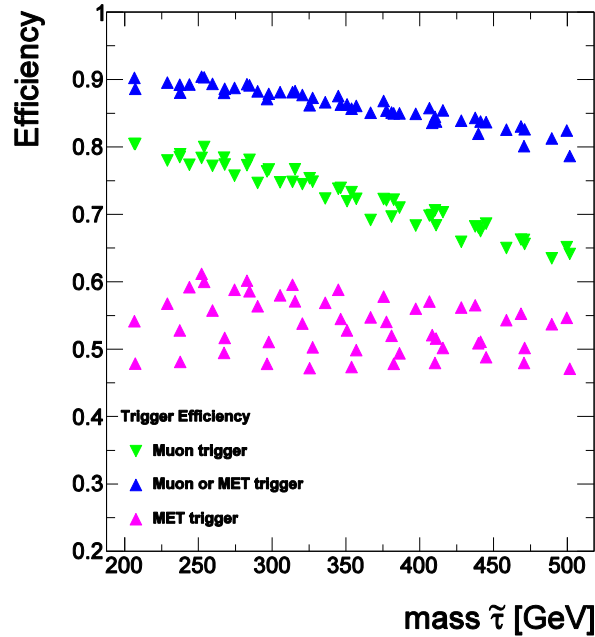


Figure 12: Expected efficiency of the muon triggers (green points), the E_T^{miss} triggers (purple triangles) and a logical OR of the two (blue squares) for GMSB events, as a function of the stau mass.

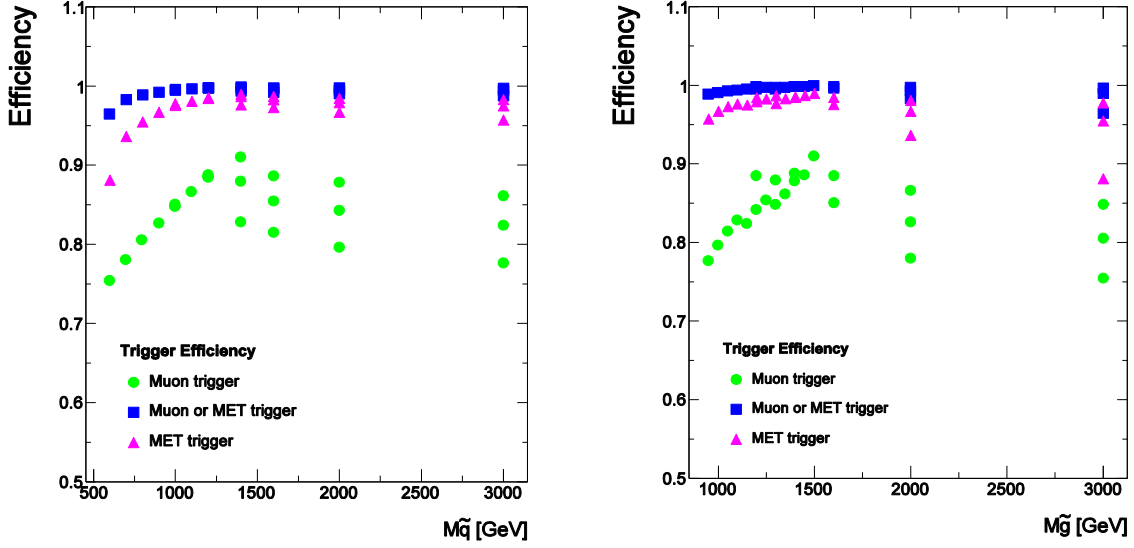


Figure 13: Expected efficiency of the muon triggers (green points), the E_T^{miss} triggers (purple triangles) and a logical OR of the two (blue squares) for LeptoSUSY events as a function of squark mass (left) and gluino mass (right).

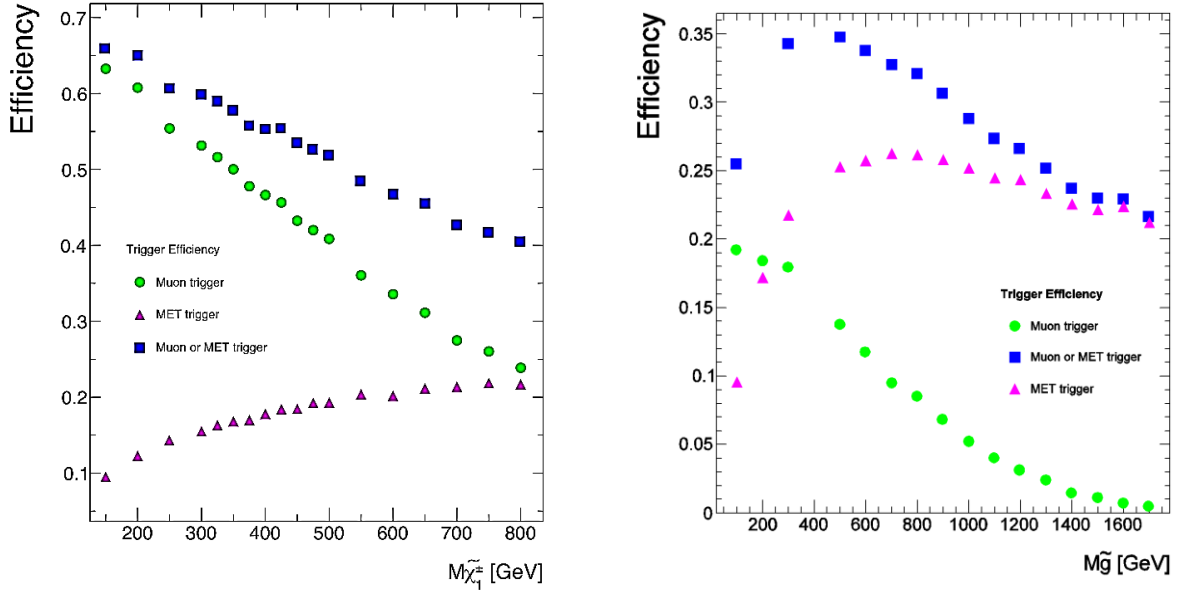


Figure 14: Expected efficiency of the muon triggers (green points), the E_T^{miss} triggers (purple triangles) and a logical OR of the two (blue squares) for the long-lived chargino samples as a function of the chargino mass (left) and gluino within the R -hadron simulation (right).

Figure 14 (right) shows the trigger efficiency for R-hadrons as a function of the gluino mass. A decrease in the MET trigger efficiency as a function of the gluino mass comes from changes in production mechanism and thus the ISR content in these events (from gluon-gluon fusion to quark-anti-quark annihilation).

In all cases a decrease in the muon trigger efficiency with the LLP mass is shown in the plots, as a result of the increase in out-of-time candidates due to their higher mass.

ii. Offline event selection

Only events with a good primary vertex (PVX) are selected. I.e. at least three ID tracks and additional requirements on the position of the reconstructed PVX.

The PVX is defined as the reconstructed vertex with the highest $\sum p_T^2$ of associated tracks.

In the slepton search, an additional requirement is placed on the least number of reconstructed muons per events to be two. This is an inflection of both GMSB and LeptoSUSY models conserving R-parity. The final state is expected to include two stable sleptons, i.e. two charged LLPs are expected per event, and they both have a muon-like signature. This cut was found to be very efficient in reducing the number of background events.

For the charginos and R-hadron searches the cut on the number of reconstructed muons is not applied, mainly because in the chargino production it is likely to have events with chargino-neutralino, hence only one LLP can be found. For the R-hadron scenario, cutting on the number of muons can eliminate events with an R-hadron that was produced as electrically charged (i.e. with an ID track) but exit the calorimeters as neutral. Hence without an MS signature.

iii. Offline candidate selection

The candidates within each event that passed the online and offline selections are required to pass their own set of selection cuts that are defined according to the SR.

(i) Sleptons

Due to the similar final state (two charged stable sleptons) in both GMSB and LeptoSUSY scenarios, the candidates are selected by the same cut flow and their SRs are defined in the same way.

The selection of the candidates starts with relatively loose selection cuts with high signal efficiency (with respect to the other SRs) and two candidates per event. Vary rarely would a non-GMSB event have two high- p_T muons, with poorly measured β and large reconstructed mass. Events with 2 candidates that passed the loose selection are categorized in the “two-candidate” SR. However, a case when only one reconstructed candidate passed the loose selection can be a result of a bad reconstruction of the other candidate. In order not to eliminate this event, the single reconstructed candidate is required to pass another set of tighter selection cuts to ensure it is not a source of background. In case the candidate passed the tighter selection it will be categorized under the “one-candidate” SR.

Table 5 summarizes the number of events in both data and expected number of events in examples of simulated sleptons samples.

The following cuts are applied in the loose “two-candidate” selection:

- $|\eta| < 2.5$
- $p_T > 70\text{GeV}$
- Z veto: in case a candidate is combined with any other track to an invariant mass of approximately ($\pm 10\text{GeV}$) the Z boson mass are both rejected

- Cosmic veto: elimination of muons originating from cosmic-ray background by removing tracks that do not pass close to the PVX in the Z coordinate (distance of track bigger than 10mm) and by applying a topological cut on the combination of any two candidates with opposite η and ϕ ($|\eta_1 + \eta_2| < 0.005$ and $||\phi_1 - \phi_2| - \pi| < 0.005$)
- Two muon stations: the candidates are required to have associated hits in at least two out of the three super-layers of precision measurement chambers in the MS
- β quality: the estimated β from each of the different technologies is required to be consistent within that technology, as specified in section (v). A requirement on the total number of DoF > 3 (number of calorimeter cells + MS hits – number of technologies contributing to the combined β estimation) is also applied (example can be seen in Figure 15)
- β consistency: consistency requirement between all the technologies contributing to the combined β within a 3σ agreement
- β - $\beta\gamma$ consistency: the combined β is also required to be consistent with β from $\beta\gamma$ deduced for the Pixel measurements
- $0.2 < \beta < 0.95$: reduction of background by applying a final cut on the combined β to be within the specified range

The “one-candidate” SR contains single candidates that passed the loose selection without a second candidate and are required to pass a tighter selection:

- β quality: the β of the candidate needs to be estimated from at least two technologies (out of the three), and the number DoF > 6
- $0.2 < \beta < 0.95$: The range of $0.85 < \beta < 0.95$ is used as a control region for systematic uncertainties studies on the background estimation method, while a harsher cut on the combined β to be within the $0.2 < \beta < 0.85$ range is for a candidate in the “one-candidate” SR

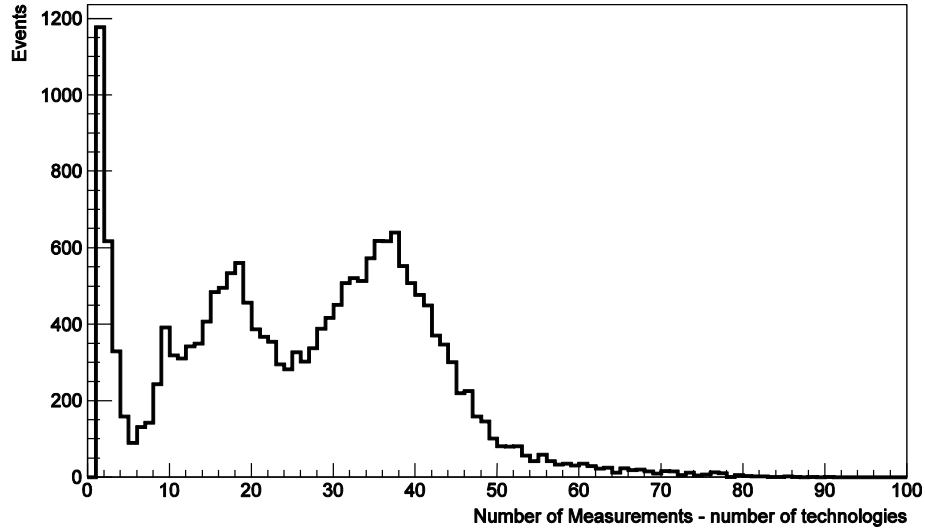


Figure 15: The number of calorimeter cells plus MS hits contributing to the β measurement, minus the number of sub-detector systems used for a signal slepton sample.

Events	Data	GMSB				LeptoSUSY			
		$m_{\tilde{\tau}_1} = 345\text{GeV}$		$m_{\tilde{\tau}_1} = 438\text{GeV}$		$m_{\tilde{g}} = 3000\text{GeV}$		$m_{\tilde{g}} = 1600\text{GeV}$	
		$m_{\tilde{q}} = 600\text{GeV}$	$m_{\tilde{q}} = 1000\text{GeV}$	$m_{\tilde{q}} = 600\text{GeV}$	$m_{\tilde{q}} = 1000\text{GeV}$	$m_{\tilde{q}} = 600\text{GeV}$	$m_{\tilde{q}} = 1000\text{GeV}$	$m_{\tilde{q}} = 600\text{GeV}$	$m_{\tilde{q}} = 1000\text{GeV}$
	Observed	Exp.	Eff.	Exp.	Eff.	Exp.	Eff.	Exp.	Eff.
Generated		44.6	100.0	11.1	100.0	3.9	100.0	1.05	100.0
Quality & Trigger	68958057	39.0	84.7	9.4	84.7	3.8	97.4	1.04	99.0
2 muons	32083845	37.4	83.9	8.9	80.2	3.6	92.3	1.02	97.1
Two-candidate SR	149	13.5	30.2	3.4	30.6	1.2	30.7	0.34	32.4
One-candidate SR	2254	8.6	19.3	2.3	20.7	0.9	23.1	0.22	20.9

Table 4: Number of events in data and expected number of events and the efficiency in the signal simulation at each step of the events selection for several signal models.

Candidates	Data	GMSB				LeptoSUSY			
		$m_{\tilde{\tau}_1} = 345\text{GeV}$		$m_{\tilde{\tau}_1} = 438\text{GeV}$		$m_{\tilde{g}} = 3000\text{GeV}$		$m_{\tilde{g}} = 1600\text{GeV}$	
		Exp.	Eff.	Exp.	Eff.	Exp.	Eff.	Exp.	Eff.
<u>Events at this point</u>	32083845	37.4		8.9		3.6		1.0	
trigger and 2 μ 's	42010563	69.2	100.0	16.6	100.0	6.5	100.0	1.9	100.0
<u>Loose selection</u>									
$ \eta < 2.5$	41814348	69.1	99.9	16.5	99.4	6.4	98.5	1.9	100.0
$p_T > 70\text{GeV}$	2712643	67.9	98.1	16.1	97.0	6.3	96.9	1.9	100.0
Z veto	2176494	67.7	97.8	16.1	97.0	6.3	96.9	1.8	94.7
Cosmic veto	2007530	66.6	96.2	15.8	95.2	6.1	93.8	1.8	94.7
Two muon station	1933892	65.2	94.2	15.4	92.8	6.0	92.3	1.8	94.7
β quality	1628357	54.1	78.2	12.9	77.7	5.1	78.5	1.5	78.9
β consistency	1582449	50.2	72.5	12.0	72.3	4.7	72.3	1.4	73.7
β - $\beta\gamma$ consistency	1499033	48.6	70.2	11.6	69.9	4.5	69.2	1.4	73.7
$0.2 < \beta < 0.95$	114400	44.4	64.2	11.0	66.3	4.2	64.6	1.2	63.1
<u>Tight selection</u>									
Loose selection cuts	1499033	48.6	70.2	11.6	69.9	4.5	69.2	1.4	73.7
β quality	930201	34.3	49.6	8.4	50.6	3.3	50.8	1.1	57.9
β consistency	930201	34.3	49.6	8.4	50.6	3.3	50.8	1.1	57.9
β - $\beta\gamma$ consistency	930201	34.3	49.6	8.4	50.6	3.3	50.8	1.1	57.9
$0.2 < \beta < 0.95$	59676	32.3	46.7	8.1	48.8	3.1	47.7	0.9	47.4

Table 5: Number of candidates in data and expected number of candidates and the efficiency in the signal simulation at each step of the candidates selection for several signal models.

Table 5 summaries the number of candidates in the data and the expected number of candidates for selected signal models passing the selection cuts.

In the last stage we calculate the reconstructed mass of the candidate from the momentum of the candidate (measured from the track) and the final combined β : (Equation 3) $m = \frac{p}{\beta\gamma}$ then a final cut is applied on the candidate's mass. The mass

cut is chosen individually per model, i.e. the mass of the hypothetical slepton in a given model, so as to achieve 99% signal efficiency with respect to the earlier selection. For the two-candidate SR both candidates are required to have higher mass than the cut chosen.

The compatibility between the hypothetical truth mass of the slepton and its reconstructed mass was verified as can be seen in Figure 16 (left), there is a good agreement between the two.

The average efficiency, for all slepton scenarios (GMSB, EW production within GMSB and LeptoSUSY) in the two SRs combined give a total of $\sim 50\%$ expected efficiency. $\sim 30\%$ for the two-candidate SR and $\sim 20\%$ for the one-candidate SR.

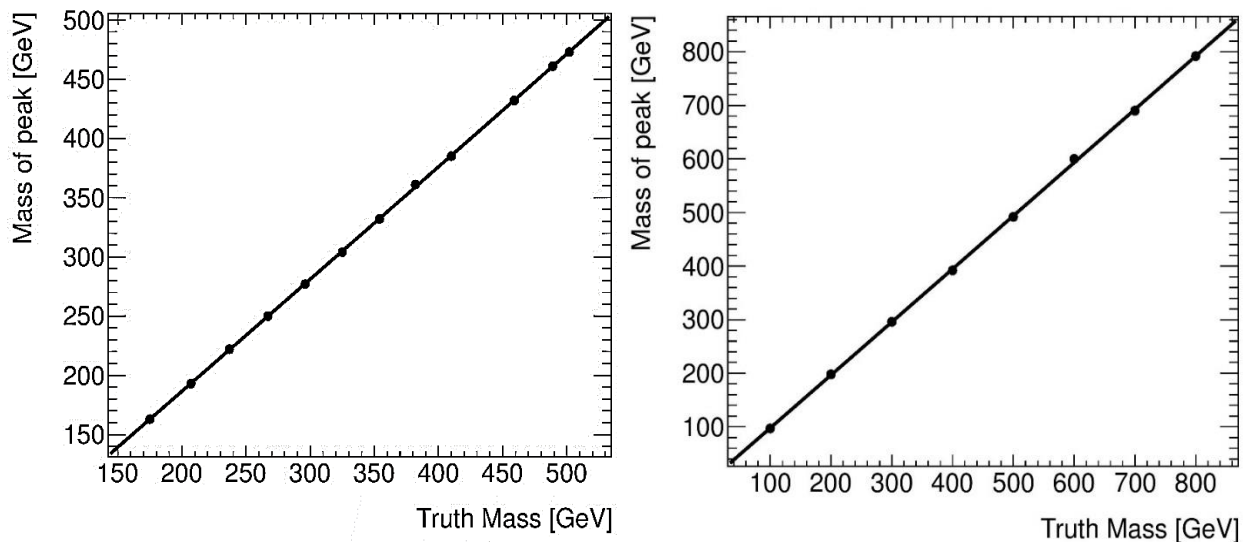


Figure 16: The mean value of the reconstructed mass peak as a function of the slepton (left) and chargino (right) truth mass, for different mass hypothesis.

(ii) Charginos

The basic selection of events and candidates for the charginos is the same as for the sleptons, apart from the requirement of the event to have at least two muons. Events from chargino-neutralino production would be lost if such cut is applied to the events.

The scenario of a chargino–chargino direct production should exhibit similar detector signature as the final state of two charged sleptons and hence the selection is similar. Event with two candidates passing the loose selection is categorized under the “two–candidate” SR.

In the chargino–neutralino production a single LLP candidate is accompanied by MET caused by the un–detected neutralino. As the MET is directly related to the reconstructed LLP, we expect it to point in the opposite direction. Figure 17 shows the MET dependence on the $\Delta\phi$ between the track and the MET in both data and MC.

In order not to eliminate chargino–chargino events, the cut on the MET is applied only in case only one candidate in the event passed the loose selection. The event will be tested for MET presence above 100GeV. Events passing this selection will be categorize under “one–loose–candidate” SR.

Last, events with one candidate that fail to pass the two–candidate loose selection and does not have a large MET, are required to pass another set of tighter selection cuts (e.g. $\beta < 0.85$). These candidates are categorized in the “one–candidate” SR.

Another major difference between the slepton and chargino “one–candidate” selections is the cut applied on the η region. The charginos are expected to be produced centrally, and it was found that requiring the chargino candidates to be within $|\eta| < 1.9$ reduces the background in both one–loose–candidate and one–candidate signal regions. Where in the sleptons the requirement of the event to have at least two muon–tracks per event is reducing a lot of this background.

The final stage is also similar between the two searches. A final cut on the reconstructed mass is applied and also here, the cuts are individual for the

different chargino mass hypothesis. Figure 16 (right) shows the agreement between the reconstructed mass with the truth mass.

The total signal efficiency is approximately 30-40%, depending on the chargino mass. $\sim 15-20\%$ for the “two-candidate” SR, $\sim 12-17\%$ for the “one-loose-candidate” and $\sim 3\%$ for the “one-candidate” SR.

Table 6 summarizes the number of events in both data and expected number of events in examples of simulated charginos samples with mass of 300 and 700GeV. Table 7 and Table 8 summaries the number of candidates in data and the expected number of candidates for the same chargino models as in Table 6, passing the candidate selection cuts.

(iii) R-hadrons

The R-hadron bound state, composed of a colored LLP and light quarks (or gluons), can change due to nuclear interactions with the hadronic calorimeter material. While mesons can change to other mesons or baryons, baryons can only change to other baryonic states due to baryon number conservation (also the probability that an R-baryon state will interact with a pion in the nucleus is negligible). Hence the electrical charge of the hadronic composition might not be conserved, cases of flip charge are anticipated and an electrical neutral bound state would escape detection.

This study is based on bound states produced as electrically charged at the IP, leaving traces in the ID and considers scenarios where it either becomes neutral while interacting the calorimeter (ID+ Calo) or remains charged (combined candidates).

A priority is given to selection of combined candidate tracks, and only in case there is no available information from the MS, a “half-track” (ID+ Calo) selection is applied. As a result an exclusive search of two signal-regions is performed that

will later be combined ('full-detector' search) in the limit settings. Due to the nature of this search to have either full or half tracks, the mass of the candidate was estimated twice: once based on β from ToF measurements: m_β and second with $\beta\gamma$ from Pixel $\frac{dE}{dx}$ measurements: $m_{\beta\gamma}$.

In approximately $\sim 15\%$ of the events there is more than one candidate, in such cases a combined candidate is preferred. In case there are more candidates with a combined track, one is chosen randomly.

The R-hadron search is divided into a search for gluinos, stops and sbottoms. This division is driven solely by the lower cross-section of the squarks and hence the different optimization. While stops and sbottoms have the same cross-section, sbottoms tend to hadronise into neutral states more than stops (57% vs. 43%). In addition, sbottom-based R-hadrons convert more into neutral states as they transvers material than stop-based R-hadrons do, extending the expected reach of the stop analysis compared to the sbottom one.

Additional requirements on the momentum, β and $\beta\gamma$ are set depending on the mass hypothesis in question. As the signal efficiency in the R-hadron case is relatively small, (due to the all possible 'neutral' scenarios, about $\sim 50\%$ of the events are not considered in this search), choosing individual cuts per mass value helped increasing it. All mass and momentum requirements are the same for a given mass value of gluinos, sbottoms and stops, while the requirements on β and $\beta\gamma$ are optimized separately to account for the lower expected cross-section in the sbottom and stop cases. Both mass estimates are required to be larger than the mass-peak value for the given hypothesis minus twice the width of the mass peak, which is typically around 20% of the peak mass, leading to an efficiency of more than 95%.

The total signal efficiency for gluino, sbottom and stop is typically 8–15%, 8–11% and 15–18%, respectively, in the full detector search, depending on the mass hypothesis.

Table 9 and Table 10 specifies the selection cut flow applied in the R-hadron search for combined track and ID+ Calo candidates respectively, for different LLP masses.

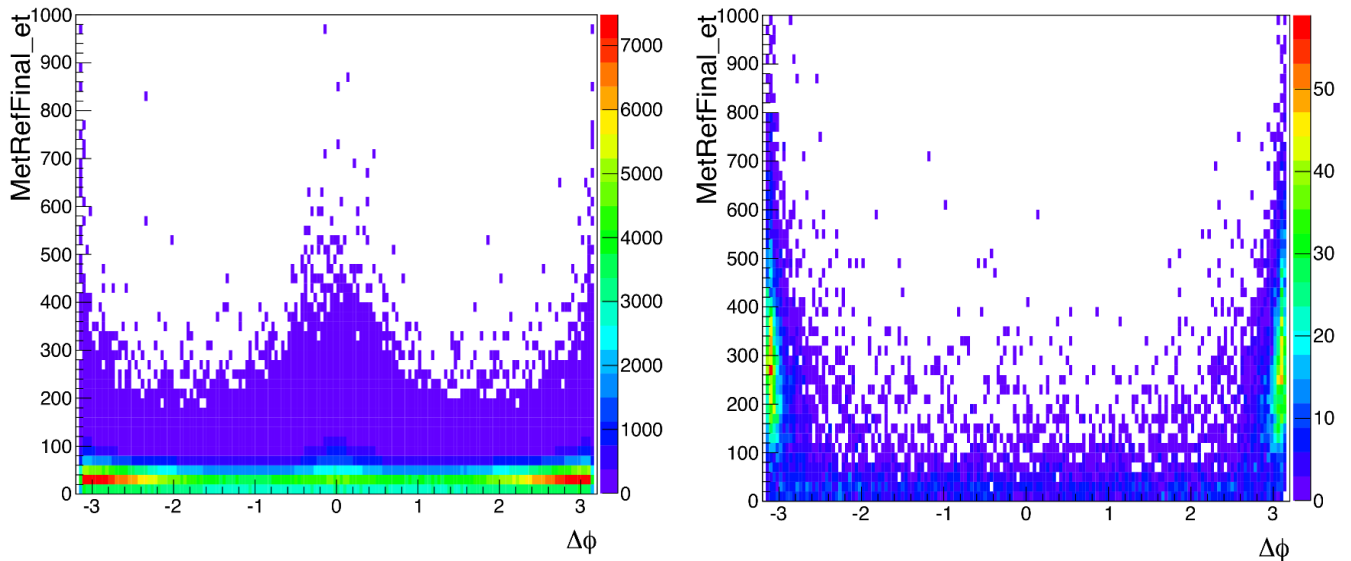


Figure 17: E_T^{miss} vs. $\Delta\phi$ between the reconstructed LLP and the E_T^{miss} for data (left) and for simulated chargino-neutralino sample (right).

Events	Data	Stable Charginos					
		Total		$\tilde{\chi}_1^\pm \tilde{\chi}_1^0$		$\tilde{\chi}_1^\pm \tilde{\chi}_1^\mp$	
	Observed	Exp.	Eff.	Exp.	Eff.	Exp.	Eff.
Generated		3886	100.0	2628	100.0	1258	100.0
Quality & Trigger	68958057	1878	48.4	1151	43.8	727	57.8
1 muon	62982159	1833	47.2	1108	42.2	726	57.7
Two-candidate SR	152	236	6.1	0	0	236	18.8
One-loose-candidate	3312	464	12.0	434	16.5	30	2.4
One-candidate SR	4097	183	4.7	20	0.8	163	6.2
Events	Data	Stable Charginos					
		Total		$\tilde{\chi}_1^\pm \tilde{\chi}_1^0$		$\tilde{\chi}_1^\pm \tilde{\chi}_1^\mp$	
	Observed	Exp.	Eff.	Exp.	Eff.	Exp.	Eff.
Generated		30.7	100.0	20.9	100.0	9.9	100.0
Quality & Trigger	68958057	11.3	37.0	7.0	33.3	4.2	42.4
1 muon	62982159	10.7	35.1	6.6	28.6	4.2	42.4
Two-candidate SR	152	1.6	4.9	0	0	1.6	16.2
One-loose-candidate	3312	3.3	11.0	2.9	14.3	0.5	5
One-candidate SR	4097	1.1	3.2	0.3	1.4	0.8	0.8

Table 6: Number of events in data and expected signal efficiency at each step of the event selection for the stable chargino models, for chargino-chargino, chargino-neutralino and in total

Candidates	Data Observed	Stable Charginos $m_{\tilde{\chi}_1^\pm} = 300\text{GeV}$					
		Total		$\tilde{\chi}_1^\pm \tilde{\chi}_1^0$		$\tilde{\chi}_1^\pm \tilde{\chi}_1^\mp$	
		Exp.	Eff.	Exp.	Eff.	Exp.	Eff.
<u>Events at this point</u>	62982159	1833		1108		726	
trigger and 1 μ	68839983	2703	100.0	1328	100.0	1374	100.0
<u>Loose selection</u>							
$ \eta < 2.5$	68630633	2366	87.5	1064	80.1	1302	99.4
$p_T > 70\text{GeV}$	5043056	2347	86.8	1055	80.1	1292	98.7
Z veto	4318342	2288	84.6	998	75.1	1290	98.6
Cosmic veto	4007044	2254	83.4	976	73.5	1278	97.6
Two muon station	3843444	2211	81.8	959	72.2	1252	95.7
β quality	3226478	1753	64.9	750	56.5	1002	76.6
β consistency	3136402	1649	61.0	714	53.8	935	71.4
β - $\beta\gamma$ consistency	2974670	1581	58.5	648	51.5	897	68.5
$0.2 < \beta < 0.95$	217233	1414	52.3	601	45.3	812	59.0
<u>Loose + MET selection</u>							
Loose selection cuts	2974670	1581	58.5	684	51.5	897	68.5
$ \eta < 1.9$	2425070	1220	33.8	513	38.6	707	54.0
$E_T^{\text{miss}} > 100\text{GeV}$ & $ \Delta\phi > 1$ & $0.2 < \beta < 0.95$	3317	497	18.3	434	32.7	63	4.8
<u>Tight selection</u>							
Loose + MET sel.	2425070	1220	44.8	513	38.6	707	54.0
Tight β quality	1767710	778	28.9	308	23.2	470	35.9
$0.2 < \beta < 0.95$	111647	739	26.8	289	21.8	450	34.0

Table 7: Number of candidates in data and the expected signal efficiency at each step of the candidate selection for a stable chargino model with mass of 300GeV for chargino-chargino, chargino-neutralino SR and in total

Candidates	Data Observed	Stable Charginos $m_{\tilde{\chi}_1^\pm} = 700\text{GeV}$					
		Total		$\tilde{\chi}_1^\pm \tilde{\chi}_1^0$		$\tilde{\chi}_1^\pm \tilde{\chi}_1^\mp$	
		Exp.	Eff.	Exp.	Eff.	Exp.	Eff.
<u>Events at this point</u>	62982159	10.8		6		4.2	
trigger and 1 μ	68839983	15.4	100.0	7.3	100	8.1	100.0
<u>Loose selection</u>							
$ \eta < 2.5$	68630633	13.5	99.3	6.1	83.6	7.4	91.4
$p_T > 70\text{GeV}$	5043056	13.0	95.6	5.9	80.8	7.1	87.7
Z veto	4318342	12.9	94.2	5.7	78.1	7.1	87.7
Cosmic veto	4007044	12.6	92.7	5.6	76.7	7.0	86.4
Two muon station	3843444	12.2	89.8	5.4	74.0	6.8	84.0
β quality	3226478	9.8	72.3	4.3	58.9	5.5	67.9
β consistency	3136402	9.3	67.9	4.1	56.2	5.2	64.2
β - $\beta\gamma$ consistency	2974670	8.9	65.0	3.9	53.4	5.0	61.7
$0.2 < \beta < 0.95$	217233	8.8	65.0	3.9	53.4	4.9	60.5
<u>Loose + MET selection</u>							
Loose selection cuts	2974670	8.9	65.0	3.9	53.4	5.0	61.7
$ \eta < 1.9$	2425070	7.6	56.2	3.3	45.2	4.3	53.1
$E_T^{\text{miss}} > 100\text{GeV}$ & $ \Delta\phi > 1$ & $0.2 < \beta < 0.95$	3317	4.3	31.4	2.9	39.8	1.4	17.3
<u>Tight selection</u>							
Loose + MET sel.	2425070	7.6	56.2	3.3	45.2	4.3	53.1
Tight β quality	1767710	5.1	37.2	2.1	28.8	2.9	35.8
$0.2 < \beta < 0.95$	111647	5.1	37.2	2.1	28.8	2.9	35.8

Table 8: Number of candidates in data and the expected signal efficiency at each step of the candidate selection for a stable chargino model with mass of 700GeV for chargino-chargino, chargino-neutralino SR and in total

Candidates		Data	R-hadrons					
			$m_{\bar{g}} = 1300\text{GeV}$		$m_{\bar{b}} = 700\text{GeV}$		$m_t = 800\text{GeV}$	
		Observed	Exp.	Eff.	Exp.	Eff.	Exp.	Eff.
<u>Events at this point</u>		69598819	8.74		127.27		65.96	
At least 4 tracks from any vertex	$N_{tracks}^{Vertex} > 3$	370159794	17.34	1.000	255.69	1.000	132.50	1.000
Minimum transvers momentum	$p_T > 50\text{GeV}$	26642886	7.88	0.454	121.31	0.474	77.53	0.585
Sensible absolute momentum	$p < 4\text{TeV}$	26360302	7.71	0.445	120.13	0.470	77.05	0.581
Isolation from high-p jets	$\Delta R_{jet,p_T > 40\text{ GeV}} > 0.3$	16341913	7.56	0.436	118.75	0.464	76.09	0.574
Isolation from other high-p tracks	$\Delta R_{trk,p_T > 10\text{ GeV}} > 0.25$	15397731	7.46	0.430	117.61	0.460	75.07	0.567
At least 6 SCT hits	$N_{SCT}^{hits} + N_{SCT}^{dead\ sensors} > 5$	14312551	7.41	0.427	116.90	0.457	74.74	0.564
At least 6 TRT hits	$N_{TRT}^{hits} > 5$	7815658	6.38	0.638	112.31	0.439	67.06	0.506
Central longitudinal vertex position	$ z_0 \leq 10\text{mm}$	7291354	6.36	0.367	111.46	0.436	66.81	0.504
Central radial position	$ d_0 \leq 2\text{mm}$	7277077	6.36	0.367	111.46	0.436	66.81	0.504
No shared Pixel clusters	$N_{PIX}^{shared\ hits} = 0$	7254509	6.33	0.365	110.94	0.434	66.47	0.502
At least 2 good Pixel clusters	$N_{PIX}^{good\ \frac{dE}{dx}\ hits} > 1$	6804661	5.87	0.338	104.64	0.409	62.32	0.470
Sensible Pixel $\frac{dE}{dx}$ value	$0\text{ MeVg}^{-1}\text{cm}^2 < \frac{dE}{dx_{PIX}} < 20\text{ MeVg}^{-1}\text{cm}^2$	6804398	5.86	0.338	104.64	0.409	62.32	0.470
Sensible $\beta\gamma$ value	$0.240 < \beta\gamma_{PIX} < 10$	3896765	5.68	0.327	101.13	0.396	60.38	0.456
Z veto	$ m(LLPcand, \mu) - m_z > 10\text{ GeV}$	2624689	5.65	0.326	100.51	0.393	59.98	0.453
Cosmic veto	$\frac{Q(LLPcand) * Q(trk)}{\geq 0\text{ or } \eta(LLPcand) + \eta(trk) \geq 0.005\text{ or } \phi(LLPcand) - \eta(trk) - \pi > 0.005}$	2624613	5.65	0.326	100.51	0.393	59.96	0.453
Quality β measurements		2428635	5.00	0.288	80.95	0.317	49.66	0.375
β consistency		1485495	4.25	0.245	46.56	0.182	37.05	0.280
Events at this point		1474631	3.62		42.05		31.31	

Table 9: Full-detector search of R-hadron candidate selection requirement for a combined track.

Candidates		Data	R-hadrons					
			$m_{\tilde{g}} = 1300\text{GeV}$ 800GeV		$m_{\tilde{b}} = 700\text{GeV}$		$m_t =$	
		Observed	Exp.	Eff.	Exp.	Eff.	Exp.	
<u>Events at this point</u>		69598819	8.74		127.27		65.96	
At least 4 tracks from any vertex	$N_{tracks}^{Vertex} > 3$	368674299	13.10	1.000	209.13	1.000	95.45	1.000
Minimum transverse momentum	$p_T > 50\text{GeV}$	25157391	3.63	0.277	74.75	0.357	40.48	0.424
Sensible absolute momentum	$p < 4\text{TeV}$	24874807	3.46	0.265	73.56	0.352	40.00	0.419
Isolation from high-p jets	$\Delta R_{jet, p_T > 40\text{ GeV}} > 0.3$	14856418	3.31	0.253	72.19	0.345	39.04	0.409
Isolation from other high-p tracks	$\Delta R_{trk, p_T > 10\text{ GeV}} > 0.25$	13912236	3.22	0.246	71.05	0.340	38.01	0.398
At least 6 SCT hits	$N_{SCT}^{hits} + N_{SCT}^{dead\ sensors} > 5$	12827056	3.16	0.242	70.34	0.336	37.69	0.395
At least 6 TRT hits	$N_{TRT}^{hits} > 5$	6330163	2.13	0.163	65.75	0.314	30.00	0.314
Central longitudinal vertex position	$ z_0 \leq 10\text{mm}$	5805859	2.11	0.161	64.89	0.310	29.76	0.312
Central radial position	$ d_0 \leq 2\text{mm}$	5791582	2.11	0.161	64.89	0.310	29.76	0.312
No shared Pixel clusters	$N_{PIX}^{shared\ hits} = 0$	5769014	2.08	0.159	64.37	0.308	29.42	0.308
At least 2 good Pixel clusters	$N_{PIX}^{good\ \frac{dE}{dx}\ hits} > 1$	5319166	1.62	0.124	58.07	0.278	25.26	0.265
Sensible Pixel $\frac{dE}{dx}$ value	$0\text{ MeVg}^{-1}\text{cm}^2 < \frac{dE}{dx}_{PIX} < 20\text{ MeVg}^{-1}\text{cm}^2$	5318903	1.61	0.123	58.07	0.278	25.26	0.265
Sensible $\beta\gamma$ value	$0.240 < \beta\gamma_{PIX} < 10$	2411270	1.43	0.109	54.57	0.261	23.33	0.244
Eta cut	$ \eta < 1.65$	1944827	1.20	0.091	51.02	0.244	20.51	0.215
Z veto	$ m(LLPcand, \mu) - m_z > 10\text{ GeV}$	959197	1.17	0.089	50.49	0.241	20.15	0.211
Cosmic veto	$\frac{Q(LLPcand) * Q(trk)}{\geq 0\text{ or } \eta(LLPcand) + \eta(trk) \geq 0.005\text{ or } \phi(LLPcand) - \eta(trk) - \pi > 0.005}$	959125	1.17	0.089	50.49	0.241	20.15	0.211
Sensible β calo	$0.2 < \beta_{calo} < 2$	924916	1.03	0.079	43.53	0.208	17.05	0.179
Quality β measurements	$\sigma_\beta < 0.12$	459737	0.59	0.045	25.77	0.123	9.98	0.105
<u>Events at this point</u>		4580630	0.60		24.59		9.35	

Table 10: Full-detector search of R-hadron candidate selection requirement for an ID+ Calo track.

IX. Background Estimation

Charged LLPs are expected to interact with the detector like heavy muons. Although they are not predicted by the SM, due to detector measurement resolution the β of a SM particle can be miss-measured, i.e. $\beta < 1$. Cutting on relatively high p_T and requiring high quality β measurement that is consistent between the different technologies will reduce the background events significantly.

Beam halo (straying muons) and cosmic rays can be another source of background for this search.

Beam halo muons are usually a result of the LHC beam protons interacting with residual gas in the beam-pipe or with the beam-pipe itself, leading to hadronic shower. Most of the shower will be absorbed in the surrounding material, yet muons from the shower can survive and enter the detector, travel in parallel to the beam line and be not in-time with the BC, mistakenly reconstructed as “late” from the previous collision BC [34].

Cosmic-ray muons are hitting the muon chambers at random times. Such a track can be miss-identified as two opposite tracks coming from the IP.

Both beam halo and cosmic-ray muons are likely to be measured not within collision BC hence will exhibit low β measurements and can be reconstructed accidentally as coming from the IP. These are handled by applying topological cuts on the track of the candidate to be close to the IP and not to be reconstructed together with another candidate with mass at the range of the Z boson.

Yet, some of the miss-measured muons together with other sources of background such as beam halo events and cosmic rays can still pass the selection applied to the candidates, and are the main sources for background in this analysis.

The background estimation is based entirely on data. Low β particles in the background are due to the measurement resolution and without a correlation to their measured momentum. A random pairing of momentum and β will reproduce the background. For LLPs there is a clear correlation between β and the momentum of the candidate, reflected in the mass. The signal would appear as a peak in the mass distribution. Producing random pairings of momentum and β breaks the correlation between the candidate's momentum and β and will smear the signal over the entire distribution rather than pile-up as a peak. Since the ratio of signal over background is very small (prior to the final selection cuts) and the background β is distributed around 1 due to measurement resolution, this technique ensures an accurate background mass estimation.

Yet, there are different detector technologies in different regions of the ATLAS, each has its own measurement resolution and when matching random pairings between the momentum and β one can artificially cause a correlation between the two. To avoid that we divide the detector into η regions and the pairing is done per region. Table 11 specifies the detector division into eight η regions.

i. Sleptons and Charginos

β probability distribution function (pdf) is constructed per search, per signal region within the search and per η region. A candidate with its measured momentum is matched with a randomly chosen β drawn from the pdf, replacing it's originally measured β and is then required to pass the final selection cuts. This step is repeated many times (~ 1000) and is weighted by the number of repetition to avoid statistical fluctuations. Figure 18 exhibits the constructed β pdfs per eta region of candidates that pass all pdf selection criteria in the slepton search.

The distribution of the resulted mass values obtained this way gives the background estimation. Figure 19 and Figure 20 show the data and background

estimation for the different signal–regions in the slepton and chargino searches, respectively.

Region Name	η
BARREL 1	$0 < \eta < 0.4$
BARREL 2	$0.4 < \eta < 0.65$
BARREL 3	$0.65 < \eta < 1.05$
ENDCAP 1	$1.05 < \eta < 1.19$
ENDCAP 2	$1.19 < \eta < 1.4$
ENDCAP 3	$1.4 < \eta < 1.7$
ENDCAP 4	$1.7 < \eta < 2.0$
ENDCAP 5	$2.0 < \eta < 2.5$

Table 11: Definition of the 8 η regions.

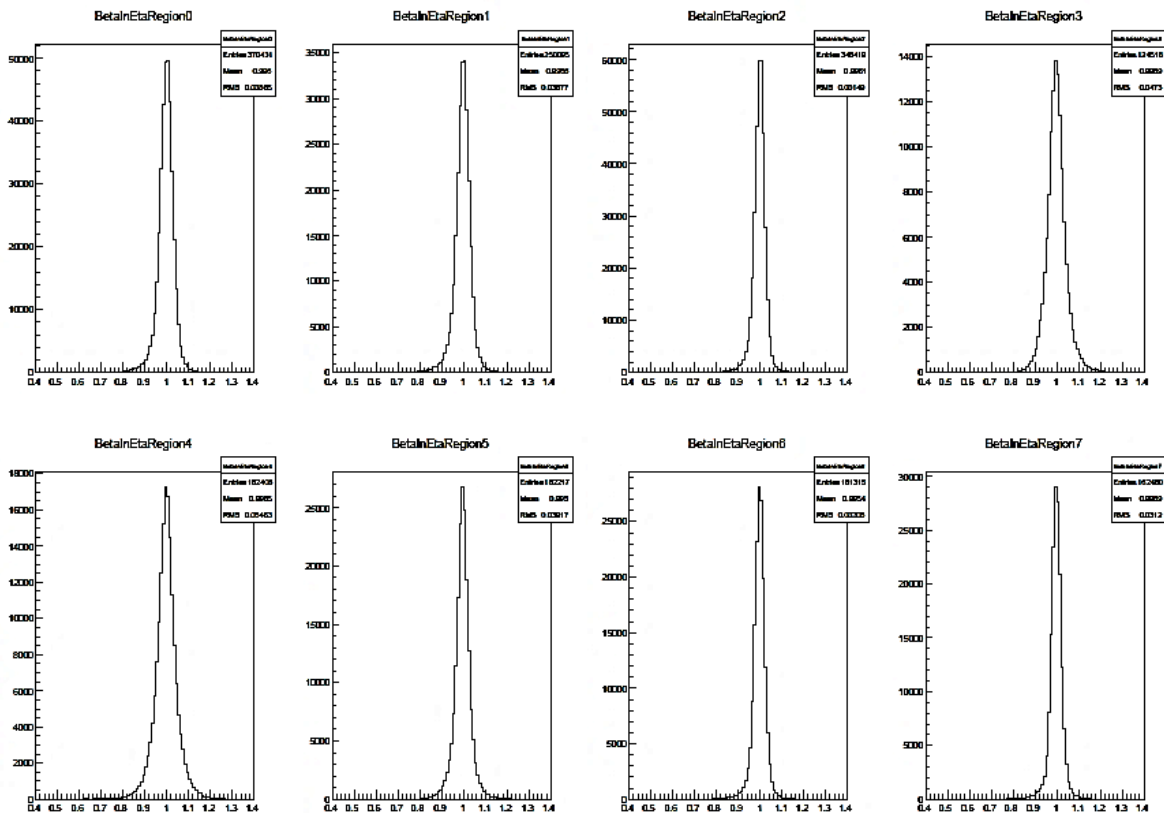


Figure 18: β distribution of data in the different η regions of the slepton search.

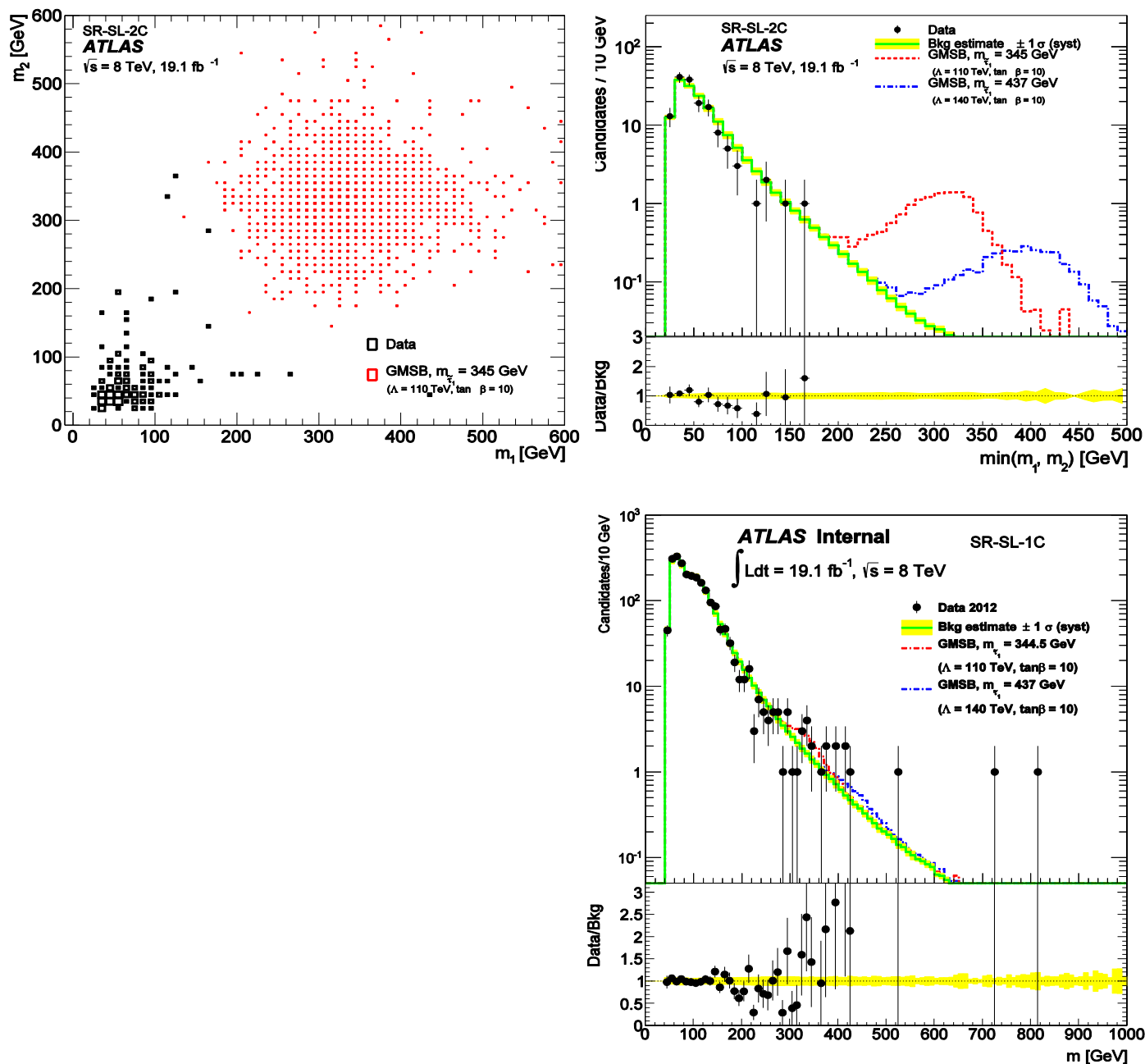


Figure 19: Reconstructed mass m_β of one candidate (m_2) vs. m_β of the other candidate (m_1) for observed data (black) and expected signal (red) in the GMSB slepton search in the two-candidate signal-region (top-left). Observed data, background estimate and expected signal (red/blue) in the slepton search for the lower of the two masses (m) in the two-candidate signal-region (GMSB $\tilde{\nu}_1$ masses of 344.5 and 437 GeV) (top-right), and for the one-candidate signal-region (LeptoSUSY simulation mass $m_{\tilde{q}} = 2.0, 1.2$ and 0.9 TeV with $m_{\tilde{g}} = 1.2$ TeV) (bottom).

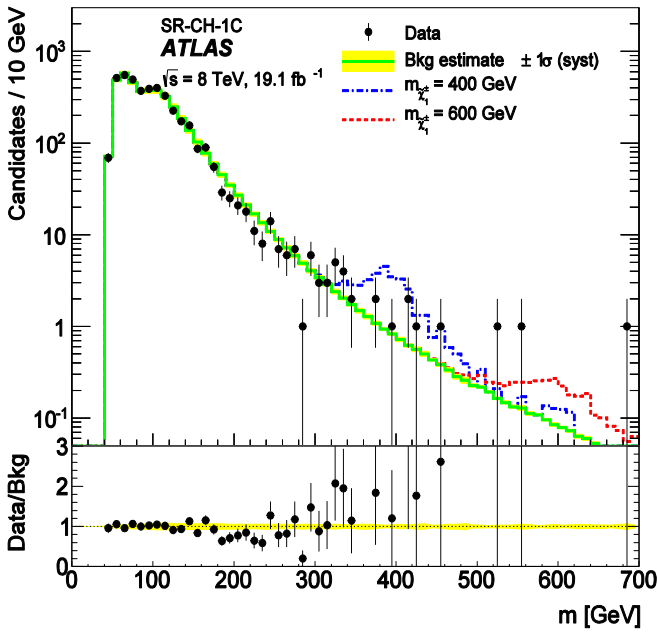
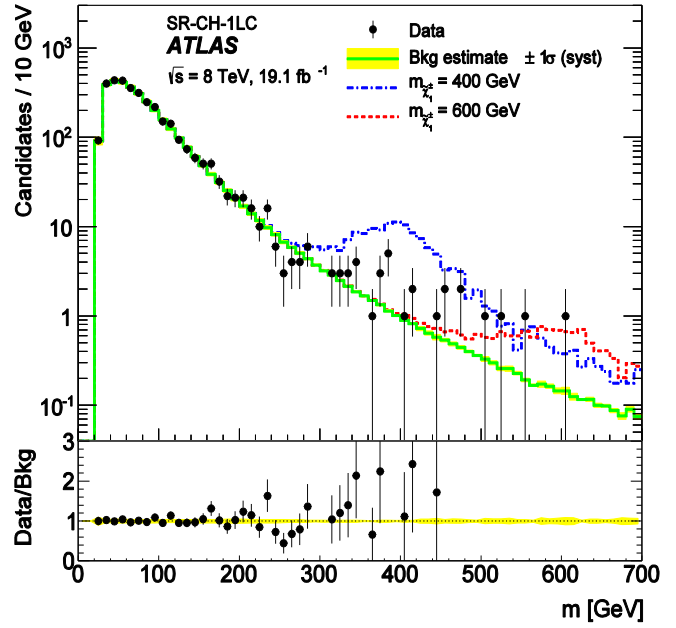
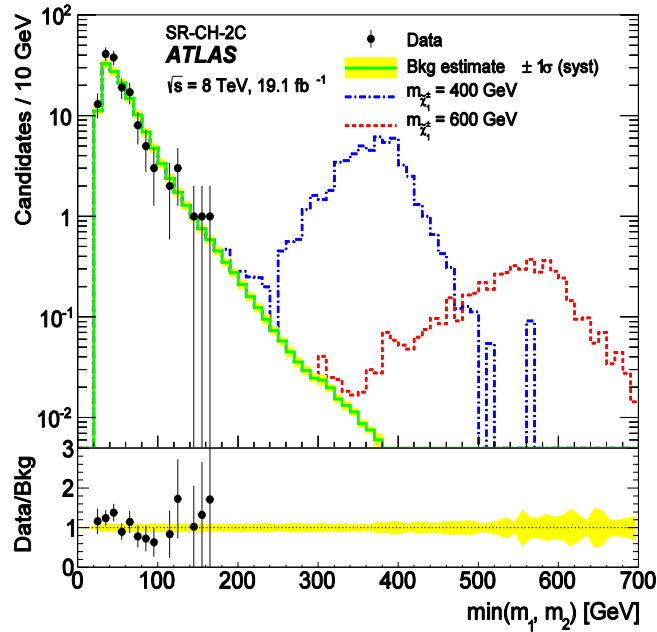


Figure 20: Reconstruction mass m_B in observed data, background estimate and expected signal ($\tilde{\chi}_1^\pm$ masses of 400 and 600 GeV) in the chargino search for the lower of the two masses in the two-candidate signal-region (top-left), for the one-loose-candidate signal region (middle) and the one candidate signal-region (bottom).

ii. R-Hadrons

Since the nuclear interactions between the light particles in the R-hadron and the detector material can lead to a flip of charge cases, this search considers either combined track or half-track (ID+ Calo). Especially in the latter case the Pixel dE/dX measurement plays a bigger role in this analysis than in the others. The final cuts are applied on β as well as on $\beta\gamma$ and p and are individual per model.

The majority of these LLPs are expected to be produced centrally (most of the energy will be exploited for the two LLPs production, leaving very little energy for other particles to be produced) hence cutting on lower η region than the other searches will reduce background events. The pdfs are constructed per search, and per η region for β as well as for $\beta\gamma$ and p and the background is estimated twice: once for mass with β based on ToF measurements (m_β) and second based on $\beta\gamma$ from Pixel dE/dX measurement ($m_{\beta\gamma}$) and a consistency between the two is studied. Figure 21, Figure 22 and Figure 23 show the data and background estimation of a 500GeV LLP searches: gluino, stop and sbottom, respectively, for both mass distributions.

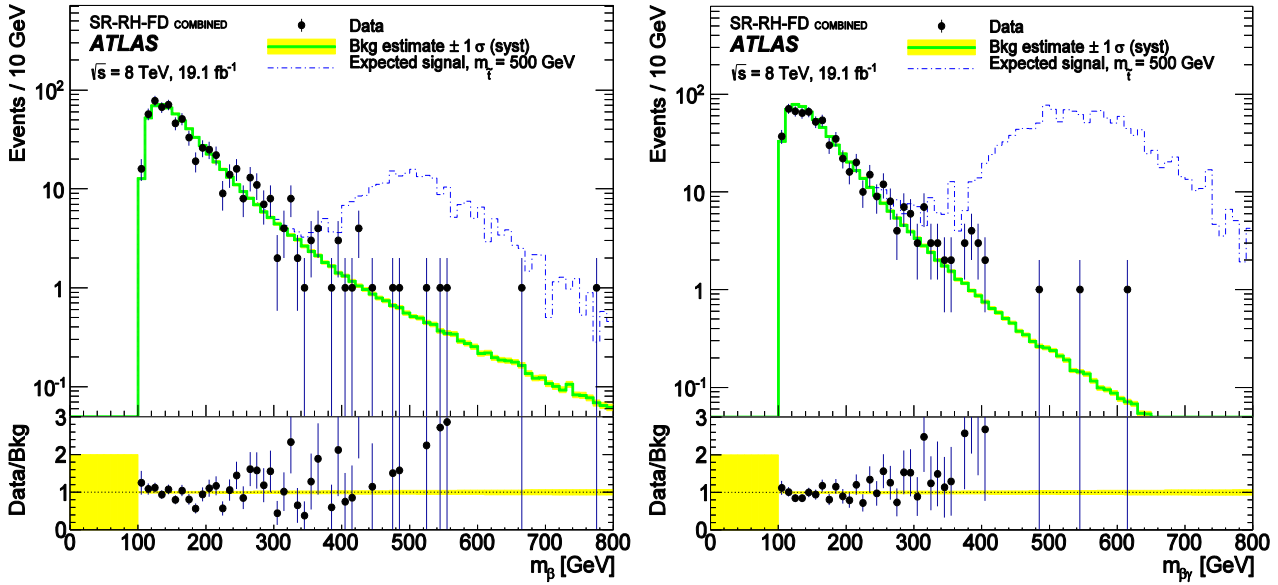


Figure 21: Data and background estimation for m_β (left) and $m_{\beta\gamma}$ (right) in the full-detector R -hadron search of a 500GeV gluino.

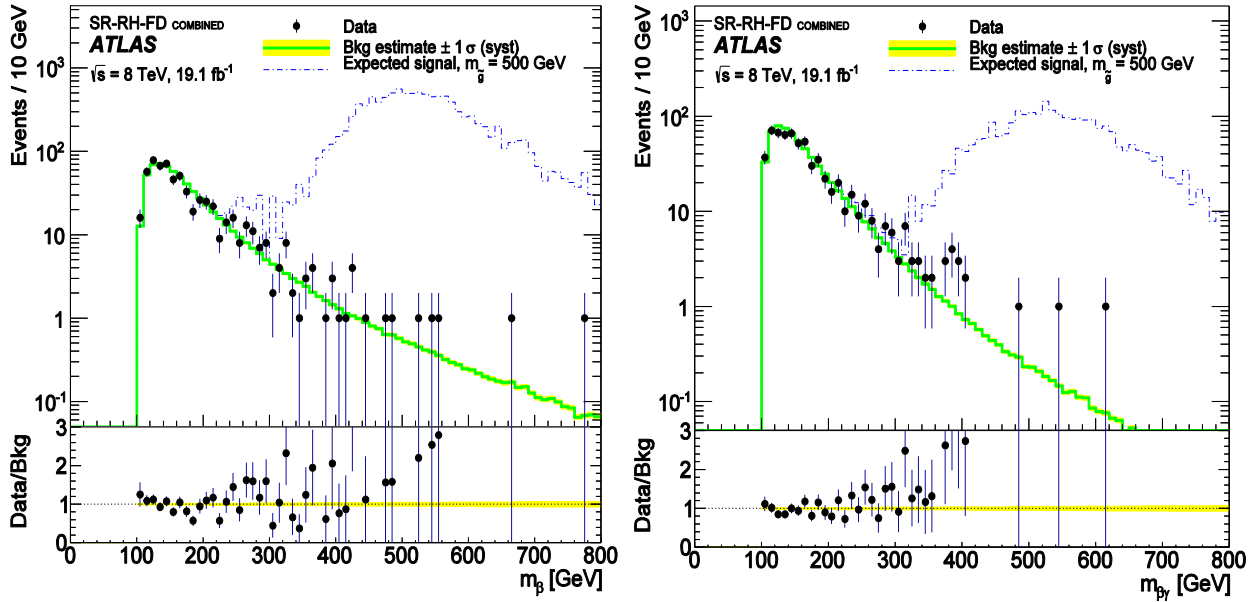


Figure 22: Data and background estimation for m_β (left) and $m_{\beta\gamma}$ (right) in the full-detector R -hadron search of a 500GeV stop.

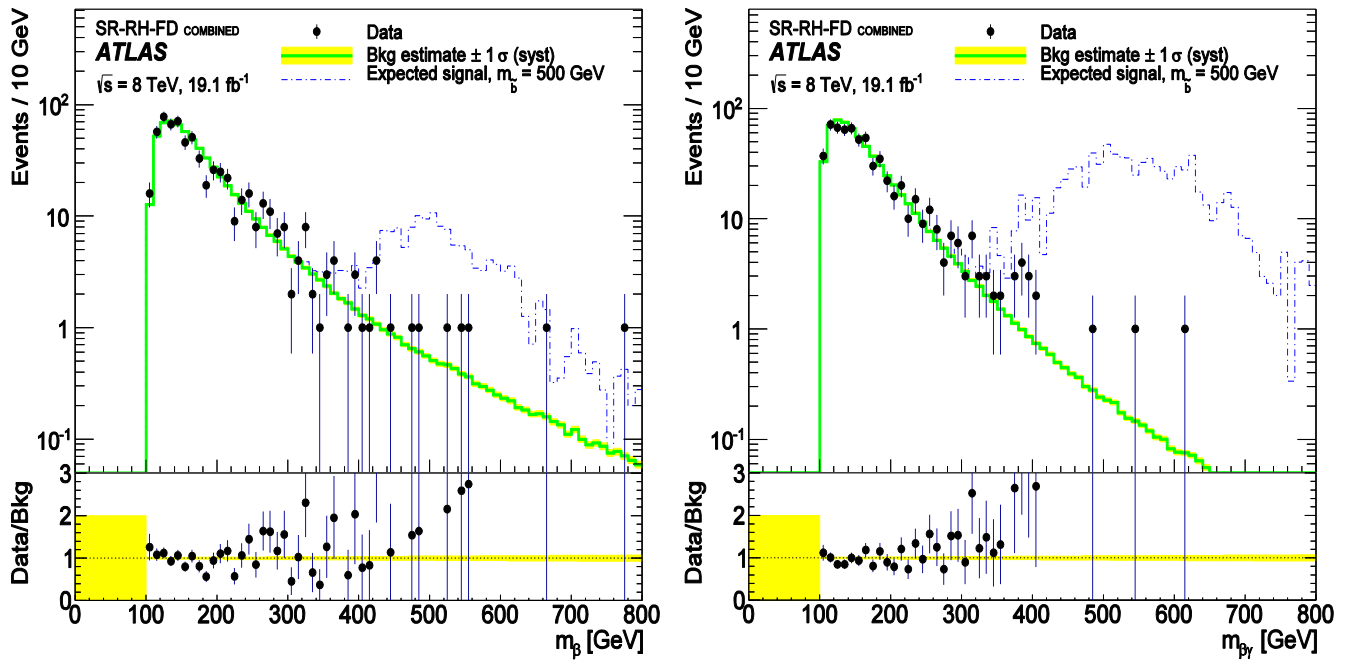


Figure 23: Data and background estimation for m_β (left) and $m_{\beta\gamma}$ (right) in the full-detector R -hadron search of a 500 GeV sbottom.

X. Systematic Uncertainties

Several possible sources of systematic uncertainty are studied. The resulting systematics uncertainties are summarized in Table 12 and Table 13 for the different searches. Detailed descriptions of each systematic study are given below.

Source	GMSB		LeptoSUSY	
	SR-SL-1C	SR-SL-2C	SR-SL-1C	SR-SL-2C
Signal size – theory	5	5	1-54	1-54
Signal efficiency				
Trigger efficiency	3.2	3.2	3.1	3.1
ISR	≤ 0.5	≤ 0.5	≤ 0.5	≤ 0.5
Pixel $\frac{dE}{dx}$ calibration	1.1	1.1	1.1	1.1
β timing calibration	1.0	2.0	1.0	2.0
Total signal efficiency	3.6	4.0	3.5	3.9
Luminosity	2.8	2.8	2.8	2.8
Background estimate	10-12	8.3-9	10-12	8.3-9

Table 12: Summary of systematic uncertainties for the slepton searches (in percentages). Ranges indicate a mass dependence for the given uncertainty (low-mass to high-mass).

Source	Charginos			R-hadrons
	SR-CH-1C	SR-CH-1LC	SR-CH-2C	SR-RH-FD
Signal size – theory	8.5	8.5	8.5	15-56
Signal efficiency				
Trigger efficiency	3.4	3.4	3.4	≤ 2.4
ISR	≤ 1.0	≤ 1.0	≤ 1.0	≤ 9
Pixel $\frac{dE}{dx}$ calibration	1.1	1.1	1.1	1.1
β timing calibration	1.0	1.0	2.0	≤ 3.6
Offline E_T^{miss} scale	5.6-7.6	2-4.2		
Total signal efficiency	6.8-8.5	4.3-5.7	4.2	≤ 10.2
Luminosity	2.8	2.8	2.8	2.8
Background estimate	3.5-6.8	4	8.7-20	3-15

Table 13: Summary of systematic uncertainties for the chargino and R-hadron searches (in percentages). Ranges indicate a mass dependence for the given uncertainty (low-mass to high-mass).

i. Theoretical cross-sections

Signal cross-sections are calculated at next-to-leading order in the strong coupling constant, including the resummation of soft gluon emission at next-to-leading-logarithmic accuracy (NLO+NLL) [35] [36] [37]. The nominal cross-section and the uncertainty are taken from an envelope of cross-section predictions using different parton distribution function sets and factorization and renormalization scales, as described in [38]. The procedure results in an uncertainty of 15% (at 100 GeV) to 56% (at 1700 GeV) for R-hadrons, a 5% uncertainty for the slepton search and a 8.5% uncertainty for the charginos. In the LeptoSUSY search the uncertainty ranges from 1% (low squark mass) up to 54% (high squark mass).

ii. Expected signal

(i) Muon trigger efficiency

The muon trigger efficiency for muons is calculated using the tag-and-probe technique on $Z \rightarrow \mu\mu$ events as described in [39].

No way was found to estimate the trigger efficiency of late arriving particles from the data. The data does not contain reasonable statistics of slow particles, and the few low beta measurements are for the most part (or entirely unless there is signal) due to mis-measurement, and are rejected by the quality cuts applied. Therefore there is no choice but to estimate the trigger efficiency of late arriving particles using the simulation.

However, the quality of the estimate depends on the exact timing implementation in the simulation, and needs to agree well with that of the data in order to obtain a good estimate of the trigger efficiency. There are two effects in the simulation which modify the efficiency; the mean hit time in the simulation is 4.7 ns earlier in the BC than in the data, and the simulated hit times are too well calibrated. Both reduce the number of triggers that are shifted from the collision BC due to inaccurate measurement. In order to account for both effects the simulated time measurements are modified to correspond for each detector element to the distribution observed in the data.

Since the trigger simulation is performed on un-smearred hit times, while the actual trigger is performed on uncalibrated time measurements, an emulation of the effect of uncalibrated time measurements on trigger efficiency is done as the following: In order to obtain the efficiency using the less accurate time measurements from data, the simulated hit times were smeared to the wider distribution observed in uncalibrated data. This was done by adding the strip-by-strip shifts of the hit time distribution (which are corrected for in the calibration process) to simulated hits, and then adding appropriate electronic jitter, as well as jitter from the charge production process, which is correlated between η and ϕ strip of the same chamber. The resulting smeared time measurements are compared to the time measurements in uncalibrated data in Figure 24 (top). When the same smearing is applied to the simulated signal the resulting modification to the β distribution can be seen in Figure 24 (middle).

The curve of trigger efficiency in the RPC as a function of β was produced from signal samples, as shown on the Figure 24 (bottom). The trigger efficiency is calculated from β measured of the hit with the longest time. This emulates the hit that determines in the trigger which BC the event is assigned to.

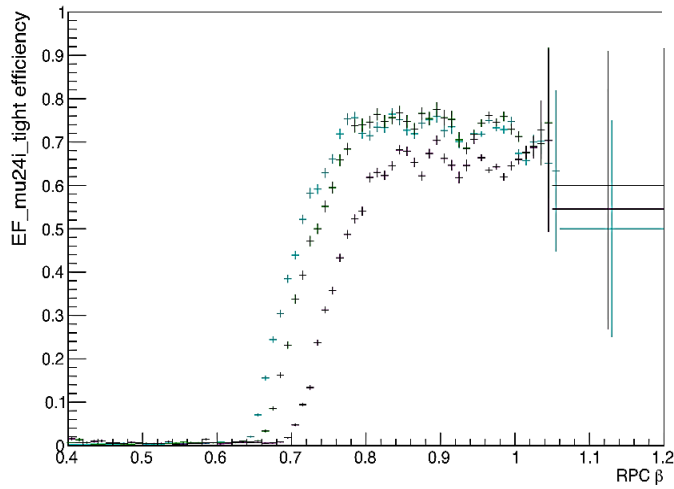
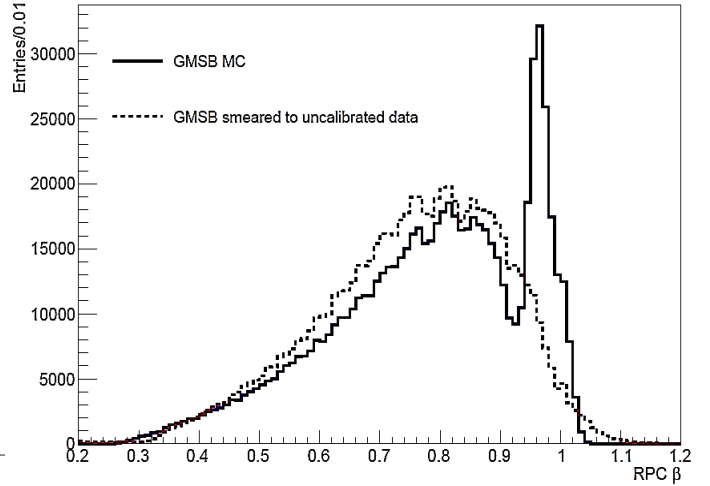
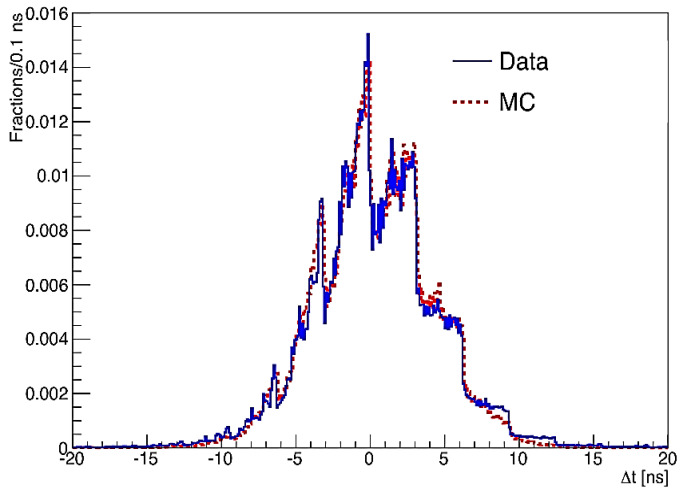


Figure 24: Top: Comparison between the hit time distribution in uncalibrated data (solid line) and in smeared simulated $Z \rightarrow \mu\mu$ events (dashed line). Middle: The β distribution in simulated GMSB events before (solid line) and after (dashed line) the RPC hit times were smeared to correspond to uncalibrated data. Bottom: Muon trigger efficiency in simulated GMSB events as a function of the trigger hit β in each of the three η barrel regions.

This trigger efficiency as a function of β is evaluated from the unsmeared simulated samples in three barrel η regions. It is then applied to the samples smeared to correspond to uncalibrated data, and the resulting trigger efficiency is calculated using:

$$\text{Equation 10: } N_{triggered} = \sum_{i=0}^{N_{events}} \left[1 - \prod_{j=0}^{N_{cand}} [1 - \epsilon(\beta_j)] \right]$$

where the RPC trigger efficiency ϵ as a function of β is obtained from Figure 24 (bottom).

The efficiency resulting from this procedure is 3–9% lower than the efficiency obtained by the trigger simulation on unsmeared simulation hits, depending on the signature and model. The difference is assigned as a systematic error for events triggered by the RPC only. Since the TGC timing in simulation is well matched to the data, events triggered by the TGC are not assigned a systematic uncertainty. The resulting systematic uncertainty on the muon trigger efficiency is 2.9–3.4%.

(ii) Missing transverse momentum trigger

The utilized triggers only rely on calorimeter energy deposits to calculate the transverse energy, and are thus ‘blind’ to muons (muons deposit very little energy in the calorimeters, as can be seen in Figure 7), which therefore could be used for calibration and systematics. To characterize the trigger efficiency, the trigger onset has been evaluated using:

$$\text{Equation 11: } \epsilon(E_T^{miss}) = \frac{A}{2} \left[1 + \text{erf} \left(\frac{E_T^{miss} - B}{\sqrt{2}C} \right) \right]^4$$

⁴ In this equation, A represents the plateau value, while B and C correspond to the effective threshold (the E_T^{miss} value at 50% efficiency) and the resolution (standard deviation of the Gaussian function that models the slope), respectively.

for $Z \rightarrow \mu\mu$ events, both in data and MC, as shown in Figure 25 and was then multiplied by bin-by-bin with the expected E_T^{miss} spectrum from simulated signal events. Here the $Z \rightarrow \mu\mu$ events are solely used to obtain the position and width of the turn-on of the given trigger chain and difference between data and MC. Figure 26 shows the E_T^{miss} distribution for $Z \rightarrow \mu\mu$ data and MC, overlaid with signal samples of stable charginos and gluino R-hadron events.

The total uncertainty is estimated from three contributions:

- (i) The relative difference between the efficiencies obtained using the onset fit from $Z \rightarrow \mu\mu$ data and MC.
- (ii) The difference in efficiencies obtained from independent $\pm 1\sigma$ variations in the threshold (B) and the distribution resolution (C) parameters relative to the unchanged onset fit in $Z \rightarrow \mu\mu$ in data.
- (iii) The difference in efficiencies obtained from independent $\pm 1\sigma$ variations in the threshold (B) and the distribution resolution (C) parameters relative to the unchanged onset fit in $Z \rightarrow \mu\mu$ in MC.

Table 14 and Table 15 shows an example of variations (ii) and (iii) illustrated for `xe80_tclcw_loose`⁵ trigger chain in a 800 GeV gluino R-hadrons sample.

The same procedure has been applied on the logical OR of all E_T^{miss} trigger chains at a given time and for all signal samples using the missing transvers momentum trigger. An overview of the maximal relative variations is given in Table 16.

⁵ Xe80 refers to a trigger chain with a $E_T^{miss} > 80 \text{ GeV}$ threshold. ‘tclcw’ refers to topoclusters (topological clustering algorithms) at event filter for E_T^{miss} and LC (local hadronic calibration).

Efficiency (relative change)	B-1 σ	B	B+ 1 σ
C-1 σ	0.25514 (+ 0.6%)	0.25269 (-0.3%)	0.25027 (-1.3%)
C	0.25600 (+ 1.0%)	0.25353	0.255111 (-1.0%)
C+ 1 σ	0.25696 (+ 1.4%)	0.25447 (+ 0.4%)	0.25203 (-0.6%)

Table 14: Efficiencies and relative change with respect to the central values of the fit parameters obtained by multiplying the fitted `xe80_tclcw_loose` turn-on curve, from $Z \rightarrow \mu\mu$ data, bin-by-bin with the E_T^{miss} spectrum, for the 800 GeV gluino R-hadrons signal MC sample. Independent 1σ variations of the effective threshold (B) and the resolution (C) are shown.

Efficiency (relative change)	B-1 σ	B	B+ 1 σ
C-1 σ	0.25428 (+ 0.6%)	0.25184 (-0.3%)	0.24944 (-1.3%)
C	0.25526 (+ 1.0%)	0.25279	0.25037 (-1.0%)
C+ 1 σ	0.25633 (+ 1.4%)	0.25384 (+ 0.4%)	0.25140 (-0.6%)

Table 15: Efficiencies and relative change with respect to the central values of the fit parameters obtained by multiplying the fitted `xe80_tclcw_loose` turn-on curve, from pile-up re-weighted $Z \rightarrow \mu\mu$ data, bin-by-bin with the E_T^{miss} spectrum, for the 800 GeV gluino R-hadrons signal MC sample. Independent 1σ variations of the effective threshold (B) and the resolution (C) are shown.

	Staus	Charginos	Gluino R-hadrons	Stop R-hadrons	Sbottom R-hadrons
Period A chains	1.85	5.07	3.83	3.41	6.29
Periods B-L chains	1.15	3.40	2.51	2.30	3.80
Luminosity weighted	1.18	3.47	2.56	2.34	3.90

Table 16: Overview of the maximal relative missing transverse momentum trigger efficiency variations for various signal types (in percentages).

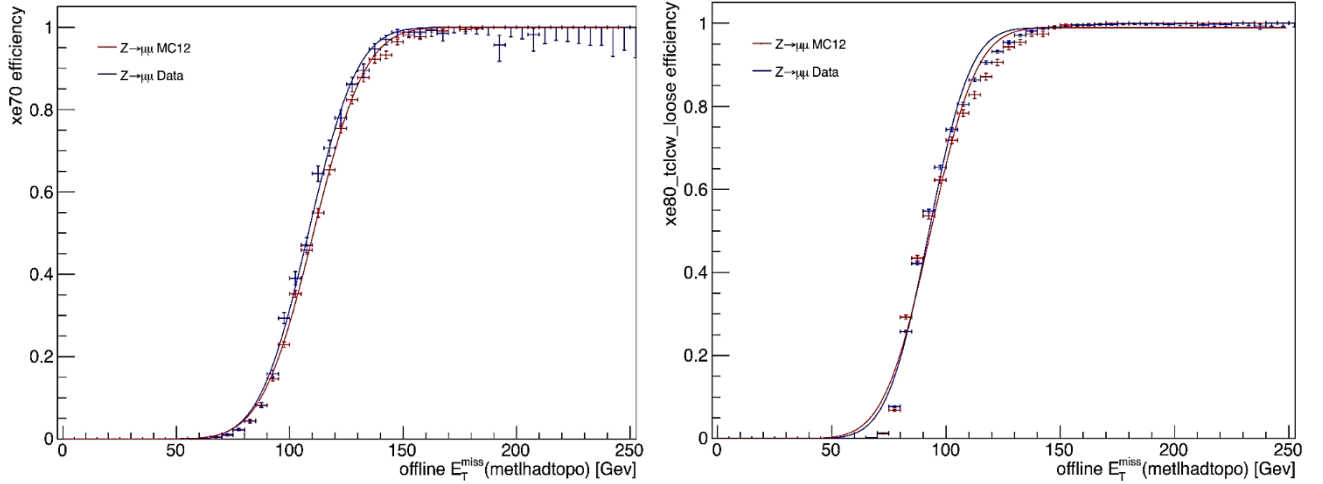


Figure 25: Turn-on curve for the $xe70$ ⁶ (left) and $xe80_tclcw_loose$ (right) trigger chains in $Z \rightarrow \mu\mu$ data (blue) and in MC (red).

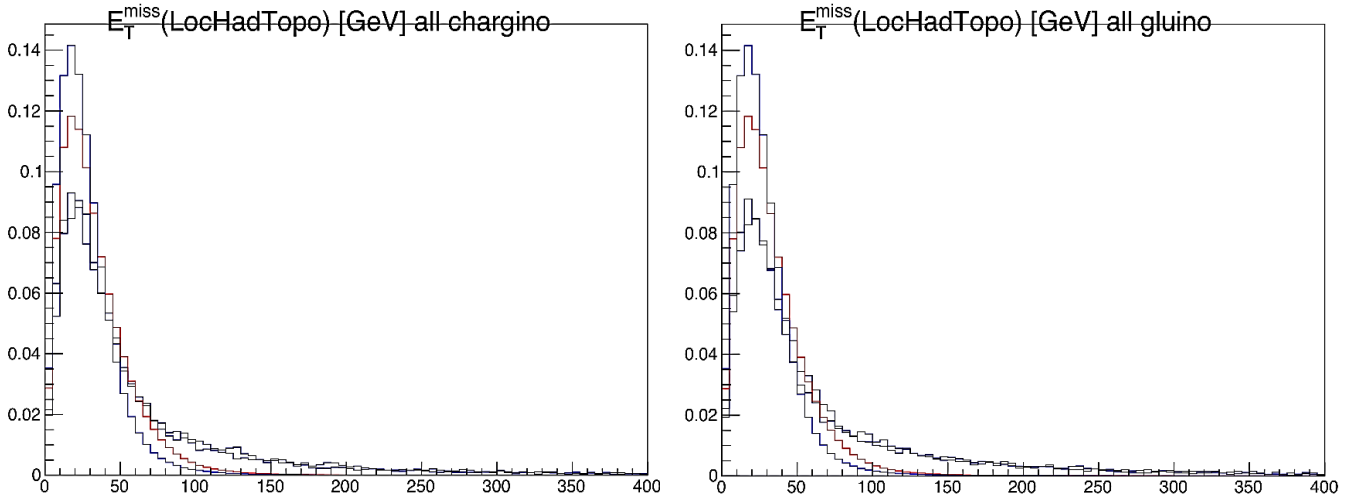


Figure 26: Missing transverse energy distribution for $Z \rightarrow \mu\mu$ (data in red, MC in blue) events, overlaid with three different stable Chargino of 400/700 GeV (left) and Gluino R -hadrons of 300/1300 GeV (right) signal events, respectively.

⁶ $xe70$ refers to a trigger chain with a $E_T^{miss} > 70$ GeV threshold, i.e. only events with a total E_T^{miss} of at least 70 GeV will trigger.

(iii) Missing transverse momentum offline cut for charginos

A systematic error on the efficiency of the E_T^{miss} selection using the variable `Met_RefFinal`⁷ for the chargino SR which employs it, is estimated by means of the `MissingETUtility-01-02-10`⁸ tool. This tool allows to recompute the E_T^{miss} and its contributions after the reconstruction step, and to obtain E_T^{miss} variations by scaling up and down these contributions. The soft contribution scale and resolution have been varied using the default procedure given by the tool. A systematic error on the signal efficiency can be obtained by using those scaled values for the E_T^{miss} cut.

This analysis uses two different definitions of the E_T^{miss} variable `Met_RefFinal`:

- (i) $E_T^{miss}[reco]$ – coming directly from the reconstruction and is used to select signal chargino samples.
- (ii) $E_T^{miss}[tool]$ – coming from the `MissingETUtility` tool, used to assess a systematic error on the signal efficiency.

The value of `Met_RefFinal` recalculated using the tool ($E_T^{miss}[tool]$) differ from the one obtained in the reconstruction step ($E_T^{miss}[reco]$), as illustrated in Figure 27 for an example signal sample with a chargino mass of 400 GeV. The discrepancy is smaller than 10% in the range [0,200] GeV. This difference is coherently found in data and MC using $Z \rightarrow \mu\mu$ control sample.

Therefore, the total systematic error on the signal efficiency due to the E_T^{miss} cut is obtained by adding in quadrature the difference between the efficiencies

⁷ `Met_RefFinal` refers to an ATLAS variable name for a refined calibrated E_T^{miss} measurement.

⁸ `MissingETUtility` provides a tool for propagating physics object uncertainties, scaling/smearing and other momentum modifications to MET in a manner consistent with the MET algorithms. It uses the MET composition maps (in the form of object weights) to rebuild the MET terms from individual objects, as required, but can easily combine the original MET terms. The `METUtility` also provides access to some systematics on the MET that do not derive directly from the objects, e.g. those on the soft terms (topo clusters and/or tracks unassociated to physics objects) [43].

obtained by using the two Met_RefFinal versions and the differences between the nominal efficiency obtained by using $E_T^{miss}[tool]$ and the ones obtained with the scaling of the different terms. Table 17 and Table 18 contain the various contributions and the total systematic errors for different chargino signal samples in the one-loose-candidate and in the one-candidate SRs, respectively for the total and for the chargino-neutralino production. The one-candidate SR is affected because events may move from the one-loose-candidate SR into it or out of it due to the systematic variations.

Mass [GeV]	One-candidate-loose SR					
	Soft terms Scale (%)	Soft terms Resolution (%)	Muon scale (%)	Jet scale (%)	Reco definition (%)	TOTAL (%)
325	0.03	0.12	2.55	0.57	3.27	4.19
400	0.15	0.04	1.25	0.48	3.38	3.64
500	0.09	0.05	0.69	0.24	2.62	2.72
600	0.26	0.13	0.94	1.32	0.81	1.84
700	0.04	0.05	0.54	1.32	2.66	3.02
800	0.22	0.23	0.31	1.87	0.84	2.10
Mass [GeV]	One-candidate SR					
	Soft terms Scale (%)	Soft terms Resolution (%)	Muon scale (%)	Jet scale (%)	Reco definition (%)	TOTAL (%)
325	0.08	0.32	3.59	0.58	6.68	7.62
400	0.19	0.18	2.09	1.65	8.67	9.07
500	0.31	0.16	1.68	0.15	5.02	5.30
600	0.82	0.79	1.14	3.91	4.56	6.21
700	0.28	0.07	1.75	2.83	5.69	6.60
800	0.41	0.29	0.43	4.89	2.60	5.58

Table 17: Various contributions and total systematic errors on the signal efficiency due to the E_T^{miss} offline cut for some of the chargino models in the total chargino production.

Mass [GeV]	One-candidate-loose SR					
	Soft terms Scale (%)	Soft terms Resolution (%)	Muon scale (%)	Jet scale (%)	Reco definition (%)	TOTAL (%)
325	0.10	0.08	1.29	0.07	2.35	2.68
400	0.15	0.04	1.25	0.48	3.38	3.64
500	0.09	0.05	0.69	0.24	2.62	2.72
600	0.26	0.13	0.94	1.32	0.81	1.84
700	0.13	0.06	0.32	1.42	0.46	1.53
800	0.23	0.29	0.21	2.13	1.35	2.56
Mass [GeV]	One-candidate SR					
	Soft terms Scale (%)	Soft terms Resolution (%)	Muon scale (%)	Jet scale (%)	Reco definition (%)	TOTAL (%)
325	0.69	0.11	6.44	0.61	34.60	35.21
400	0.19	0.18	2.09	1.65	8.67	9.07
500	0.31	0.16	1.68	0.15	5.02	5.30
600	0.82	0.79	1.14	3.91	4.56	6.21
700	1.81	0.24	3.23	9.41	2.88	10.52
800	0.82	0.77	0.46	11.38	10.07	15.25

Table 18: Various contributions and total systematic errors on the signal efficiency due to the E_T^{miss} offline cut for some of the chargino models in the chargino-neutralino production.

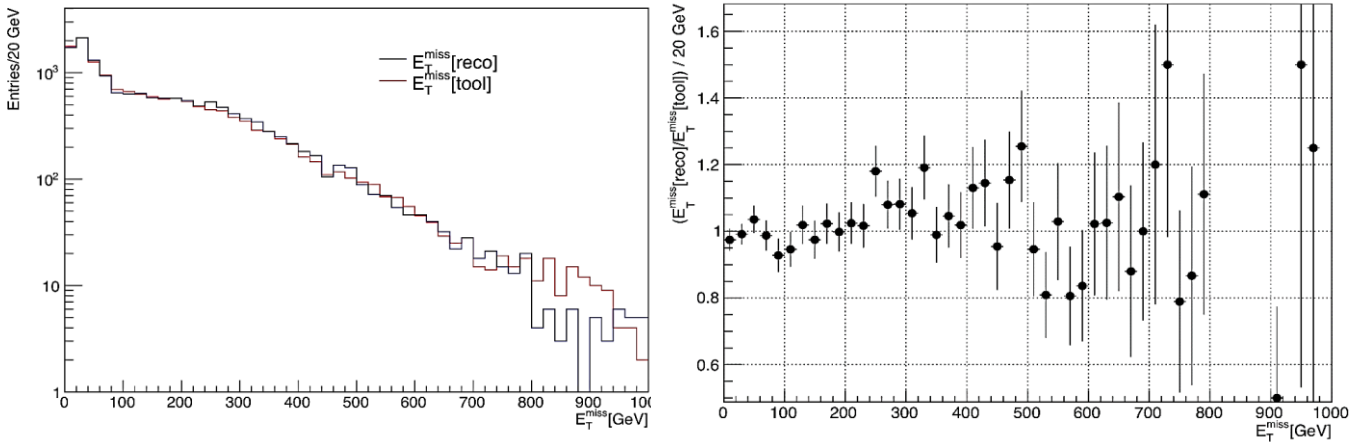


Figure 27: Comparison between the E_T^{miss} distribution from the reconstruction and the MissingETUtility for an exemplary chargino signal sample with a chargino mass of 400 GeV.

(iv) Initial state radiation in GMSB, LeptoSUSY and stable chargino events

The estimation of the Initial State Radiation (ISR) systematics for the sleptons and chargino samples is achieved by simulating events with different ISR levels for the signal samples. The mass points selected for the ISR study are representative of the full mass spectrum, the ISR systematics estimates for the remaining points are then calculated from an extrapolation of these chosen points. We used fast simulated samples with the ISR level scaled up and down within PYTHIA6.

The estimation procedure goes as follows: the missing transvers momentum distribution for each mass point is convoluted with the trigger turn-on curve to include the trigger effect in the estimation. The ratio of the convolution between Up (Down) variation and the nominal sample is our systematic estimate. The results are summarized in Table 19, Table 20 and Table 21. The variation of the estimate among the different mass points is negligible, hence the result is the same across signal types.

Λ	$\tan \beta$	ISR down %	ISR up %
80.0	10.0	-0.25	0.25
120.0	10.0	-0.25	0.25
160.0	10.0	-0.25	0.25
160.0	30.0	-0.25	0.25
160.0	50.0	-0.25	0.25

Table 19: Overview of the effect of ISR variations for the GMSB samples. The numbers are given as percentage change with respect to the nominal sample.

Squark mass [GeV]	Gluino mass [GeV]	ISR down %	ISR up %
800	3000	-0.39	0.39
1200	1200	-0.39	0.39
1200	1400	-0.39	0.39
1200	1600	-0.39	0.39
1600	1050	-0.39	0.39
1600	1250	-0.39	0.39
1600	1450	-0.39	0.39
3000	1150	-0.39	0.39

Table 20: Overview of the effect of ISR variations for the LeptoSUSY samples. The numbers are given as percentage change with respect to the nominal sample.

Chargino mass [GeV]	ISR down %	ISR up %
200	-1.6	1.6
400	-1.6	1.6
600	-1.6	1.6
700	-1.6	1.6
800	-1.6	1.6

Table 21: Overview of the effect of ISR variations for the chargino samples. The numbers are given as percentage change with respect to the nominal sample.

(v) Initial state radiation in R-hadron events

The missing transverse momentum trigger used for the R-hadrons relies on the two objects being boosted and thus the emission of at least one additional jet, which also accounts for the generally low triggering efficiency. Therefore, the trigger efficiency depends on the amount of Initial State Radiation (ISR), and depends on any uncertainty in any of these. The effect of variations in ISR have been investigated using fully simulated samples at various R-hadron masses with the ISR level scaled up and down within PYTHIA6. Applying the same procedure as used on the nominal samples to evaluate the missing transverse momentum trigger uncertainty, we estimate the effect of ISR variations. Depending on the search and mass in question and taking into account the ratio between combined and ID+ Calo candidates, the uncertainty is estimated to be less than 9.6%.

(vi) Time smearing in signal samples

The signal β resolution is estimated by smearing the measured time of the hits in the MS and calorimeter (in MC) according to the spread observed in the time calibration (data). The systematic uncertainty due to the smearing process is estimated by scaling the smearing factor up and down, so as to bracket the distribution obtained in data. A 1% (2%) maximal systematic uncertainty is found in the one-candidate (two-candidate) GMSB signal region and 3.6% in the R-hadrons. Figure 28 shows the β measurements for $Z \rightarrow \mu\mu$ MC events in the Calorimeter, the MDTs and the RPCs, with decreased and increased smearing compared to data, while Figure 30 shows the same comparison for the combined

β distribution. An example of mass distribution with different smearing for one of the sleptons signal sample is shown in Figure 31.

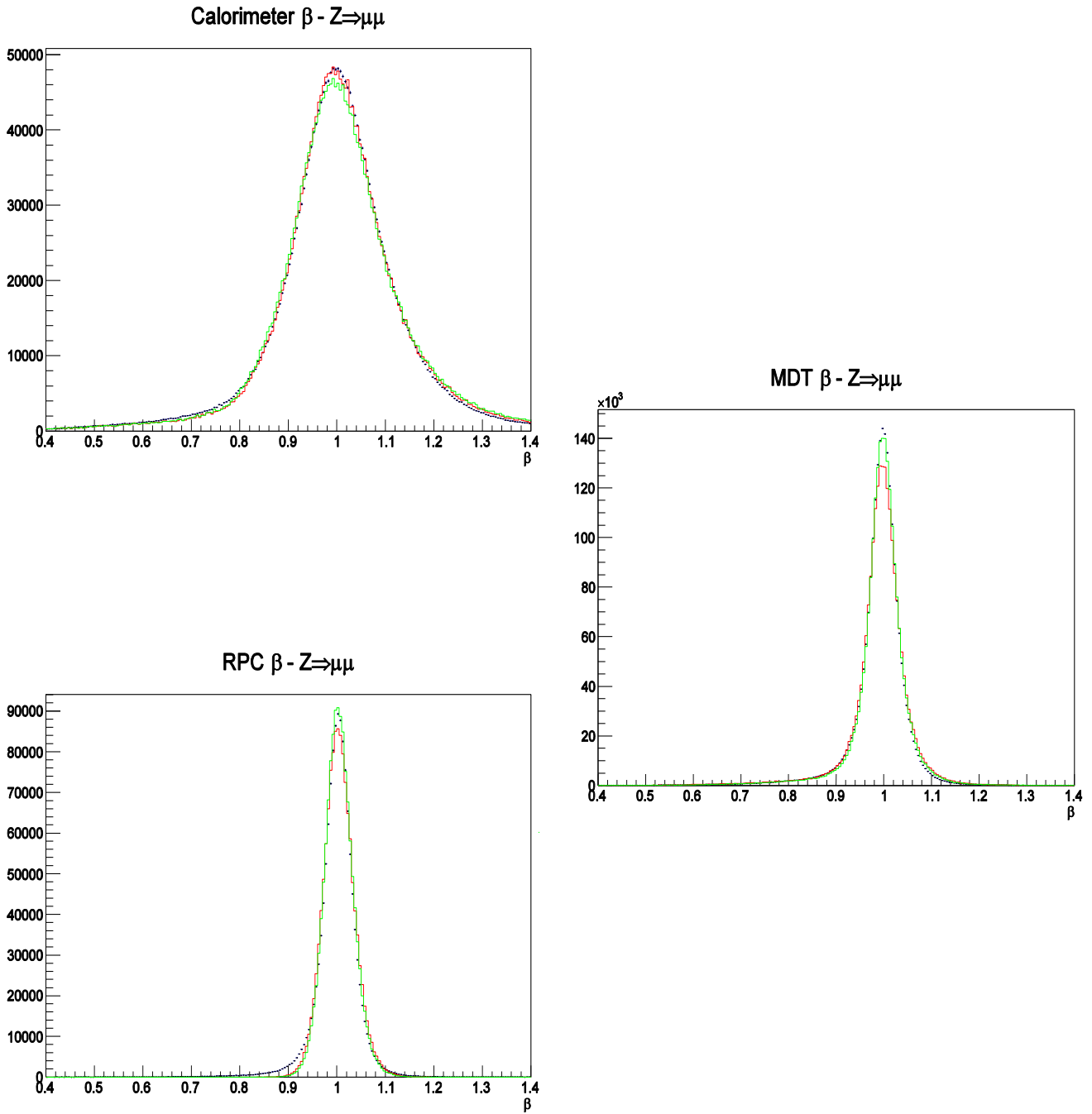


Figure 28: The β measurements of $Z \rightarrow \mu\mu$ events in the Calorimeters (top), MDTs (middle) and RPCs (bottom) with decreased (red) and increased (green) smearing of MC compared to the data (black).

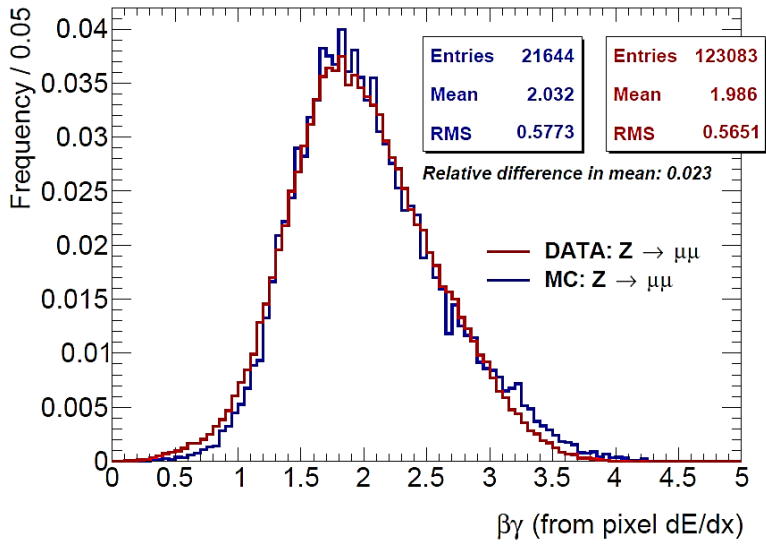


Figure 29: The $\beta\gamma$ measurements for muons from $Z \rightarrow \mu\mu$ in the data (red) and MC (blue).

Figure 30: Combined β distribution of $Z \rightarrow \mu\mu$ in the data (black) and MC smeared with up (green) and down (red) smearing factors.

Combined β - $Z \rightarrow \mu\mu$ - Loose Selection

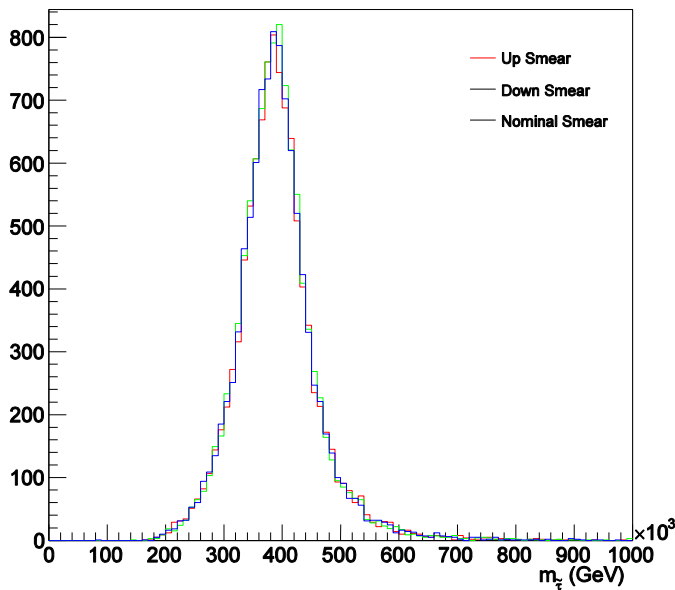
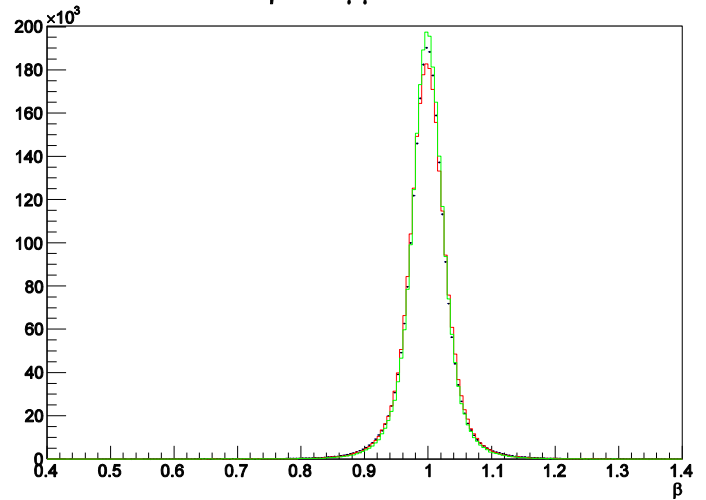


Figure 31: The mass distribution of $\tilde{\tau}_1$ with a mass of 248.6 GeV smeared with nominal (blue), up (green) and down (red) factors.

(vii) Uncertainty in $\beta\gamma$ from pixel $\frac{dE}{dx}$

The $\beta\gamma$ measurement from the pixel $\frac{dE}{dx}$ carries a systematic uncertainty in the differences between simulation and data on the R-hadron analysis. The differences can be measured by plotting $\beta\gamma$ in $Z \rightarrow \mu\mu$ events in data and simulation, as can be seen in Figure 29. It is important to stress that the details of the tails are not overly important, as the background estimates are based on the data itself, and thus it is the general scale that is important.

As can be seen in Figure 29, the scale between data and MC is off by 2.3%. We have also checked the variation of the proton mass (and given that tracking is very stable, this is in turn a check of the variations in $\beta\gamma$ scale) over time, and found the RMS of these to be 0.6%. Finally, the average proton mass itself is off the accepted value by 0.24%. Adding these effects in quadrature gives a systematic uncertainty on the $\beta\gamma$ scale of 2.4%. The impact on the signal efficiency of this uncertainty is obtained through variations. At low masses (300 GeV) the impact is 1.1%, while at higher masses (500 and 800 GeV) it is 0.4%. This is understandable, as we only cut loosely on $\beta\gamma$ and $m_{\beta\gamma}$ (i.e. very high efficiency) and as these cuts becomes relatively looser at higher mass. To stay conservative and for simplicity, we apply a systematic of 1.1% for all masses.

(viii) Luminosity

An uncertainty of 2.8% [40] is assigned to the integrated luminosity represented by the dataset.

iii. Background estimation in the slepton search

The total uncertainty on the background estimate for the slepton search considering the sources below is 10–12% for two-candidate events and 8.3–9% for one-candidate events.

(i) Momentum independence of the β distribution

To test the momentum dependence of the muon β PDF, the candidate in each η region are divided by their momentum into two bins with similar counts, and the background is estimated with the resulting β PDFs: the momentum cut used at this purpose are summarized in Table 22. The resulting systematic uncertainty is 8–11.7% for two-candidate events and 8–9% for one-candidate events. Figure 32 shows the background estimate obtained by using these β distributions for the two-candidate and one-candidate signal regions.

η Region Name	η	P cut [GeV]
BARREL 1	$0 < \eta < 0.4$	92.5
BARREL 2	$0.4 < \eta < 0.65$	102.5
BARREL 3	$0.65 < \eta < 1.05$	122.5
ENDCAP 1	$1.05 < \eta < 1.19$	152.5
ENDCAP 2	$1.19 < \eta < 1.4$	177.5
ENDCAP 3	$1.4 < \eta < 1.7$	217.5
ENDCAP 4	$1.7 < \eta < 2.0$	287.5
ENDCAP 5	$2.0 < \eta < 2.5$	412.5

Table 22: Momentum cut used in the different η regions to test the momentum dependence of the muon β PDF.

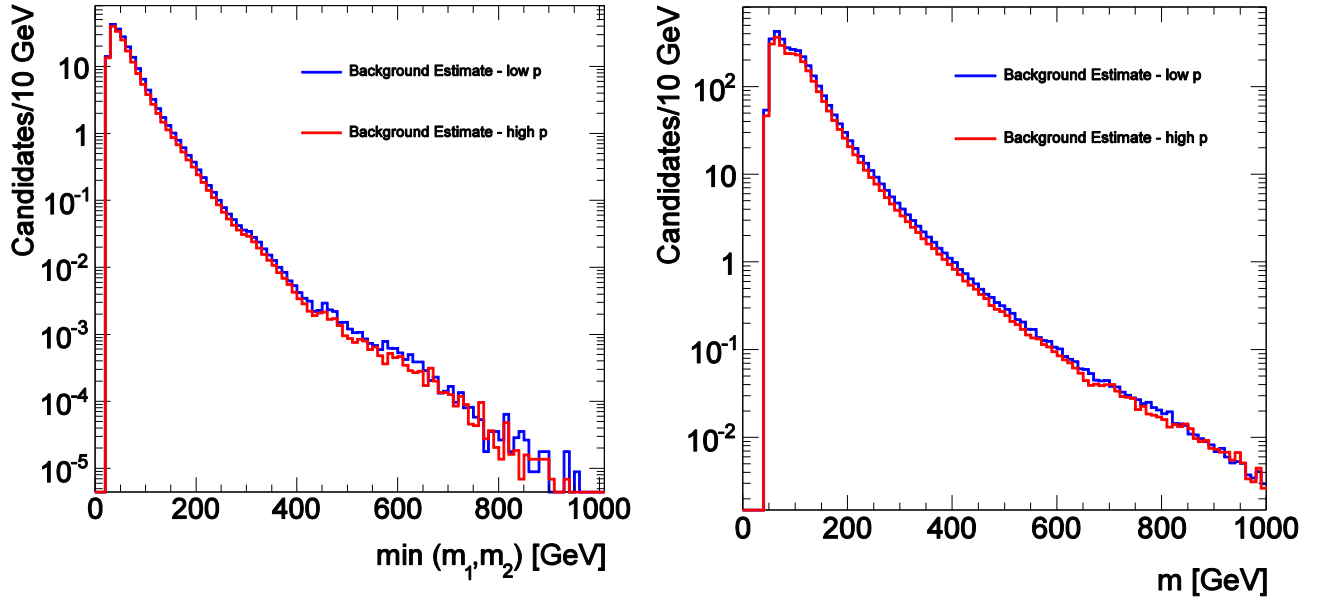


Figure 32: The background estimates obtained for the two-candidate (left) and one-candidate (right) SRs in the slepton search by using β PDFs obtained from ‘high- p ’ and ‘low- p ’ candidates.

In addition to the test above, another test was performed by extracting the momentum distributions for a sample of muons with $\beta < 0.95$ and with $\beta > 0.95$. This test is sensitive to correlations between β and momentum, and to the low statistics at the tails of the momentum distributions. Figure 33 shows the two distributions overlaid, and one can see that while the low β fraction has low statistics, the distributions are consistent. The associated systematic error is estimated as described in the previous paragraph, and not from these distributions.

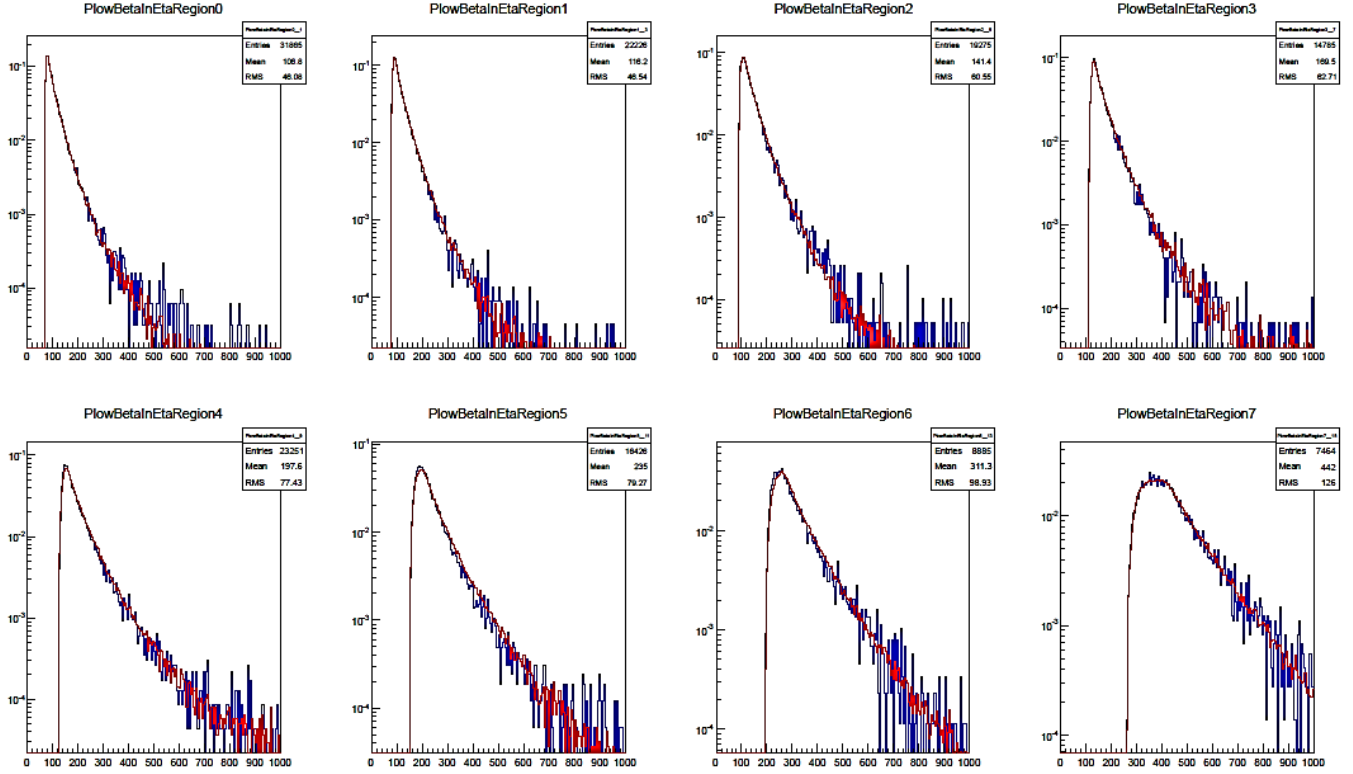


Figure 33: Momentum distributions for a sample of muons in data with $\beta < 0.95$ and with $\beta > 0.95$ (red).

(ii) Variability of β in the η regions

To quantify the variability of the β and momentum distributions within a region and its effect on the background estimation for sleptons, the detector is subdivided into 25 η regions instead of the 8 used in the searches and the background is estimated with this division. The resulting systematic uncertainty is 2–5% for the two-candidate events and 0.5–2% for the one-candidate events. Figure 35 top and bottom compare the background estimate obtained under the two η divisions schemes for the two-candidate (top) and one-candidate (bottom) signal regions respectively. Due to the finely grained division of the detector into 25 η regions, this test is also sensitive to effects related to the low statistics at the tails of the β distribution.

(iii) Source independence of the β distribution

A comparison of the background estimates obtained with muon β distribution in inclusive muon events to that from $Z \rightarrow \mu\mu$ decays when the Z veto is not applied in the selection is done. The requirement on the event to have at least two muons, ensures the majority of events will be of $Z \rightarrow \mu\mu$ decays.

The comparison study resulted in 4-5% systematic uncertainty for the two-candidate signal-region and 2-3% systematic uncertainty for the one-candidate signal-region. The background estimates are shown in Figure 34 (left and right) for the two-candidate (left) and one-candidate (right) signal-regions respectively.

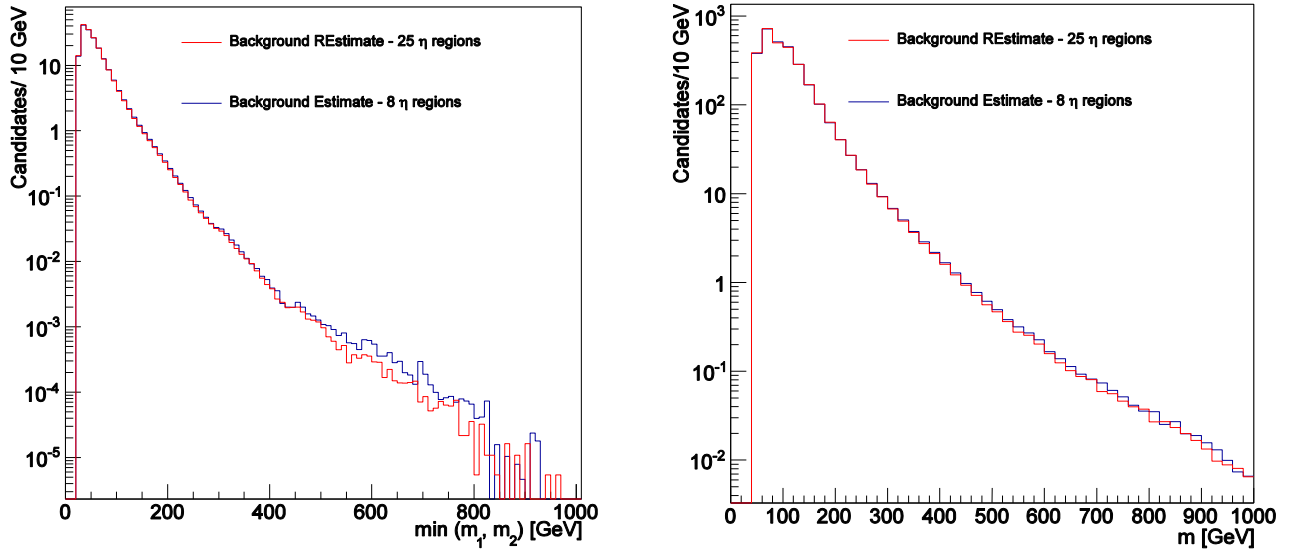


Figure 35: Comparison of the background estimate for the slepton search with 8 and 25 η regions for the two-candidate (left) and the one-candidate (right) signal-regions. The black line shows the background estimation obtained when dividing into 8 η regions, and the red line shows the background estimation obtained when dividing into 25 η regions.

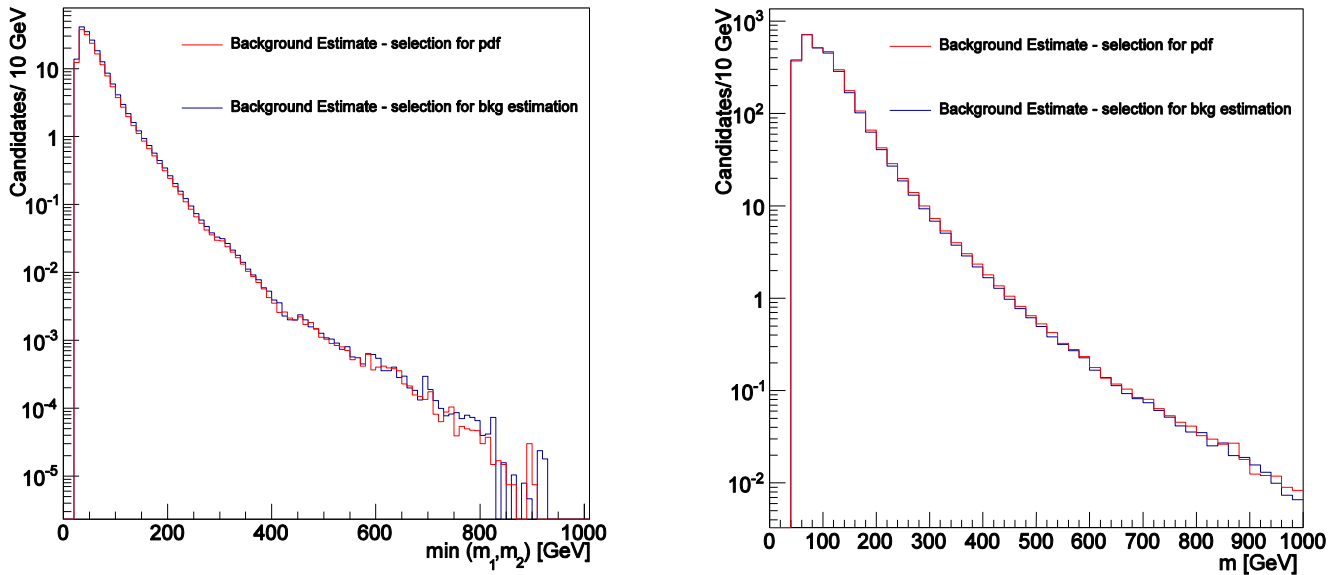


Figure 34: Comparison of the background estimation for the sleptons search using β distributions with (red) and without (blue) the Z veto for the two-candidate (left) and the one-candidate (right) signal regions.

(iv) Presence of signal

The uncertainty on the background estimation in case of the presence of signal events in the data is found to be negligible. This is so because although signal events produce a small increase of the amount of events in the low β region of the β distribution, the momentum of background particles is not correlated with these low β 's. Therefore, when the background estimation is performed, and these beta are attached to other momenta, the influence of these low β additions is washed away.

This is demonstrated by estimating the background for a data sample contaminated with MC signal events. The number of MC signal events contaminating the data is equivalent to 10 times what is expected for the integrated luminosity analyzed. Figure 37 and Figure 36 show the mass distribution for the contaminated sample and the corresponding background estimate for the two-candidate and one-candidate signal-regions respectively.

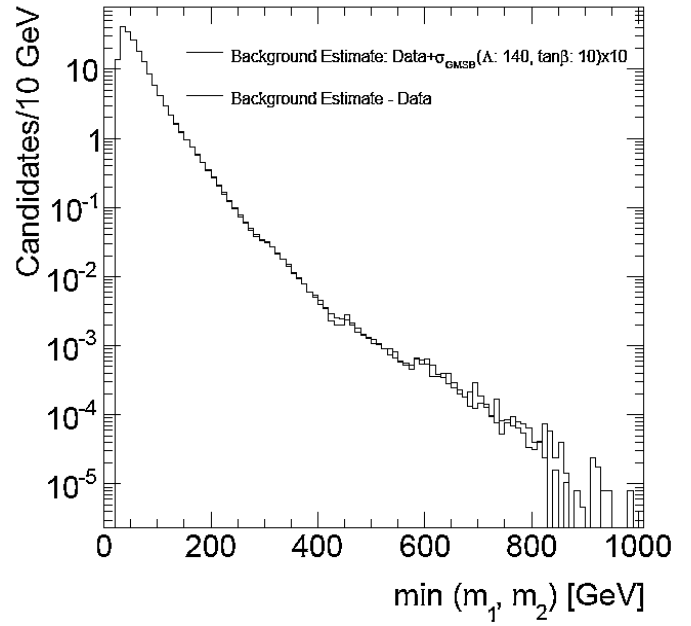
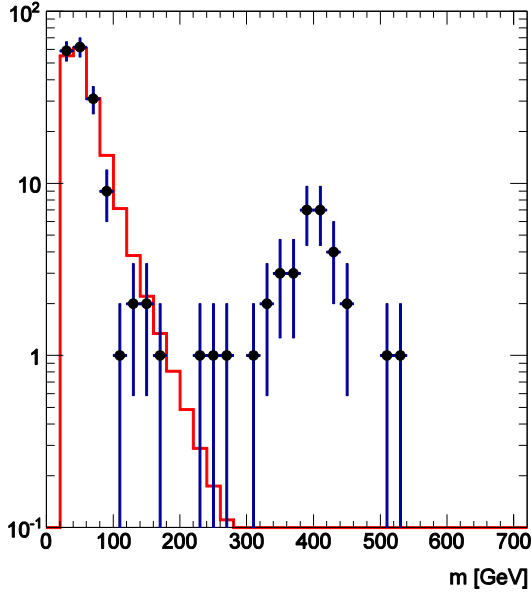


Figure 37: Mass distribution (left) and background estimation (right) for a data sample contaminated with GMSB MC signal for the two-candidate signal-region.

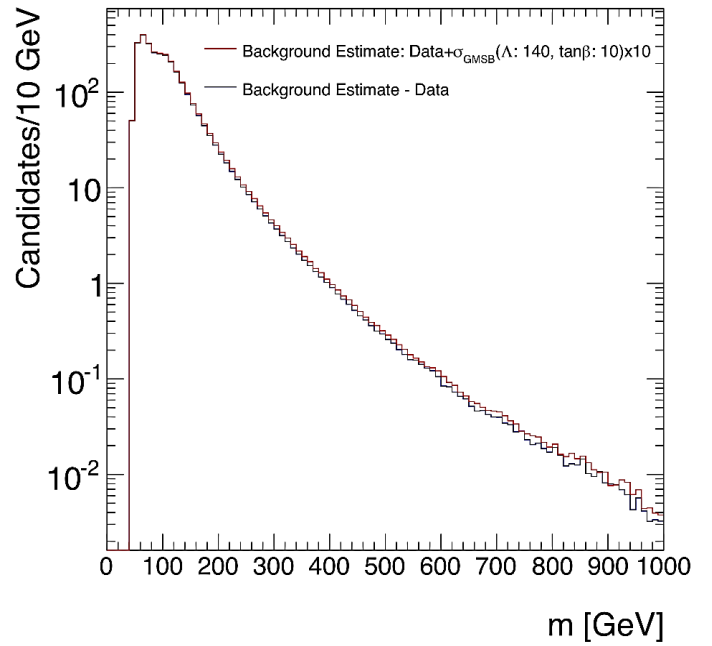
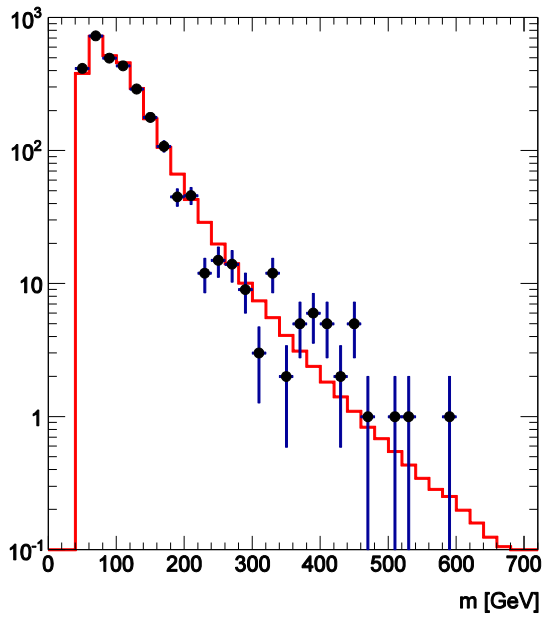


Figure 36: Mass distribution (left) and background estimation (right) for a data sample contaminated with GMSB MC signal for the one-candidate signal-region.

iv. Background estimation in the chargino search

In the case of the chargino search the same background estimation technique as for the slepton case has been used, therefore the same sources of systematic uncertainties have been considered. In addition, for the one-loose-candidate SR also the uncertainty due to possible correlations between β and E_T^{miss} or $\Delta\phi$ has been evaluated by using a PDF where neither the E_T^{miss} nor the $\Delta\phi$ cut was applied. The resulting systematic uncertainty is 1.1–3.3%. The total uncertainty on the background estimate for the chargino search is 8.7–20% for the two-candidate events, 4% for the one-loose-candidate events and 3.5–6.8% for the one-candidate (tightly selected) events.

Table 23 summarizes the results for the various contributions to the total systematic uncertainty.

Source	Two-candidates	One-loose-candidate	One-candidate
Momentum independence	8.5–11	2.2–3	3.4–6.7
β variability in η regions	2–17	0.8–2.1	0.3–0.5
Independence of the β distribution	0.1–1	0–2.3	0–0.5
E_T^{miss} and $\Delta\phi$ correlations	–	1.1–3.3	–

Table 23: Summary of systematic uncertainties (given in percentages) for the chargino search. Ranges indicate mass dependence for the given uncertainty (low mass – high mass).

v. Background estimation in the R-hadron search

Similar tests are performed to determine the uncertainty on the background for the R-hadron search. Unlike the slepton search, the range of mass hypothesis tested is very large, and it has been found that the size of the systematic

uncertainty on the background estimate grows with mass, as would be expected. In order to quantify the systematic uncertainty, the PDFs used to produce the background estimates were varied. This is done by changing their selection cuts into tighter and looser cuts, as can be found in Table 24.

Selection	Cut in β and $\beta\gamma$ for a p-PDF	Cut in p for β and $\beta\gamma$ - PDF
Baseline	$Cut_{\beta} < \beta < 0.90$ and $Cut_{\beta\gamma} < \beta\gamma < 2.5$	$70 \text{ GeV} < p < 180 \text{ GeV}$
Tighter	$Cut_{\beta} < \beta < 0.88$ and $Cut_{\beta\gamma} < \beta\gamma < 2.4$	$80 \text{ GeV} < p < 150 \text{ GeV}$
Looser	$Cut_{\beta} < \beta < 0.92$ and $Cut_{\beta\gamma} < \beta\gamma < 2.6$	$60 \text{ GeV} < p < 200 \text{ GeV}$

Table 24: Variations of selection for PDFs used for background estimation. The RMS between the resulting backgrounds estimated using baseline, tighter and looser selections for the PDF is evaluated for each mass hypothesis.

The variation in number of events that enter the PDF is about 50% and the RMS is used as a mass dependent estimate of the systematic uncertainty. The RMS as a function of mass can be seen in Figure 38. The systematic grows roughly linear with the mass and therefore a linear fit has been applied, yielding a systematic as a function of mass. This has been applied to all the hypothesis tested.

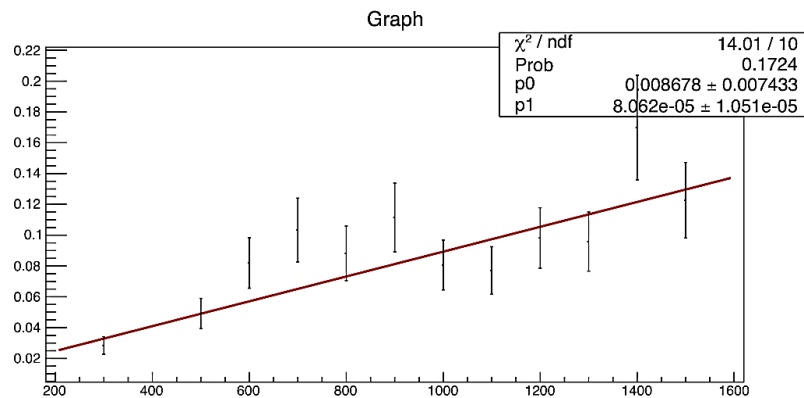


Figure 38: RMS between the resulting backgrounds estimated using baseline, tighter and looser selections for the PDF as a function of mass hypothesis. These results are fitted with a line which is then used as the final mass dependent systematic uncertainty on the background estimate.

XI. Results

The mass distribution of data vs background in all searches and their signal regions did not indicate any significant excess of data over the background, hence no discovery of new physics and limits on the studied scenarios are set using the CLs prescription [41]. The limits on the visible cross-section are calculated from the likelihood to observe the number of events found in each signal-region with candidate mass above the selected mass cut, given the background estimate and the signal efficiency, using the RooStats package [42].

For each signal region the likelihood function is built assuming a Poisson counting model for the observed number of events with Gaussian constraints for the systematic uncertainties.

For the sleptons and chargino searches, a global extended likelihood, given by the product of the likelihood functions of the various signal regions is used. In the CLs calculation, a profile likelihood statistics test is used.

Mass limits are derived by comparing the obtained cross-section limits to the lower edge of the $\pm 1\sigma$ band around the theoretical predicted cross-section for each process.

i. Sleptons

The resulting production cross-section limits at 95% confidence level (CL) in the GMSB scenario as a function of the $\tilde{\tau}_1$ mass are presented in Figure 39 and compared to theoretical predictions.

A long-lived $\tilde{\tau}_1$ in GMSB models with $N_5 = 3$, $m_{messenger} = 250 \text{ TeV}$ and $sign(\mu) = 1$ is excluded at 95% CL up to masses of 440, 440, 430, 410, 385 GeV for $\tan\beta = 10, 20, 30, 40, 50$, respectively.

Limits on the rates of specific production mechanisms are obtained by repeating the analysis on subsets of GMSB samples corresponding to each production mode. For GMSB models with parameters in this range, strong production of squarks and gluinos is suppressed due to their large masses. Directly produced sleptons constitute 30–63% of the GMSB cross-section, and the corresponding $\tilde{\tau}_1$ production rates depend only on the $\tilde{\tau}_1$ mass and the mass difference between the right-handed \tilde{e} or $\tilde{\mu}$ and the $\tilde{\tau}_1$. Thus the same analysis constraints a simple model with only pair-produced sleptons which are long-lived, or which themselves decay to long-lived sleptons of another flavor. Such direct production is excluded at 95% CL up to $\tilde{\tau}_1$ masses of 373 to 330 GeV for models with slepton mass splitting of 2.7–93 GeV. The slepton direct-production limits are shown Figure 41. Figure 40 shows the cross-section limits on direct $\tilde{\tau}_1$ production for the case where the mass splitting to the other sleptons is very large. As the theoretical prediction and the associated uncertainty bands overlap almost entirely for various values of $\tan\beta$, only the curve for $\tan\beta = 10$ is shown. Masses below 286 GeV are excluded if only the $\tilde{\tau}_1$ is produced. The values of direct $\tilde{\tau}_1$ only production are also used Figure 41 at very high mass splitting.

Finally, in the context of the GMSB model, 30–50% of the GMSB cross-section arises from direct production of charginos and neutralinos (dominated by $\tilde{\chi}_1^\pm \tilde{\chi}_1^0$ production) and subsequent decay to $\tilde{\tau}_1$. Figure 42 shows the 95% CL lower limits on the $\tilde{\chi}_1^0$ and $\tilde{\chi}_1^\pm$ mass when the final decay product is a long-lived $\tilde{\tau}_1$. In the samples used to derive these limits, the $\tilde{\chi}_1^0$ and $\tilde{\chi}_1^\pm$ masses are closely related by GMSB, as represented by the values on the two x-axes. The mass of the $\tilde{\tau}_1$ decreases with increasing $\tan\beta$ and increases with the $\tilde{\chi}_1^0$ and $\tilde{\chi}_1^\pm$ masses. At low $\tilde{\chi}_1^0$ and $\tilde{\chi}_1^\pm$ masses and large $\tan\beta$, the cross-section limits are thus affected by the amount of background in the $\tilde{\tau}_1$ mass search region, which starts at 120 GeV

for $\tan\beta = 50$ and at 170 GeV for $\tan\beta = 10$. The cross-section limits exclude $\tilde{\chi}_1^0$ masses below 537 GeV, with corresponding $\tilde{\chi}_1^\pm$ masses 210–260 GeV higher.

Limits on LeptoSUSY scenarios are set on squarks and gluinos decaying to long-lived sleptons within the LeptoSUSY model. The exclusion region in the plane $m_{\tilde{g}} vs. m_{\tilde{q}}$ is shown in Figure 43. Squark and gluino masses are excluded at 95% CL up to a mass of 1500 and 1360 GeV, respectively, in LeptoSUSY models where sleptons are stable and degenerate, with mass of 300 GeV, and all neutralinos (except $\tilde{\chi}_1^0$) and charginos are decoupled.

Examples of the observed and expected event yields, as well as efficiencies and uncertainties for data and some MC simulation signal samples, for stau within GMSB and LeptoSUSY sleptons are shown in Table 25 and Table 26 respectively, for various signal regions.

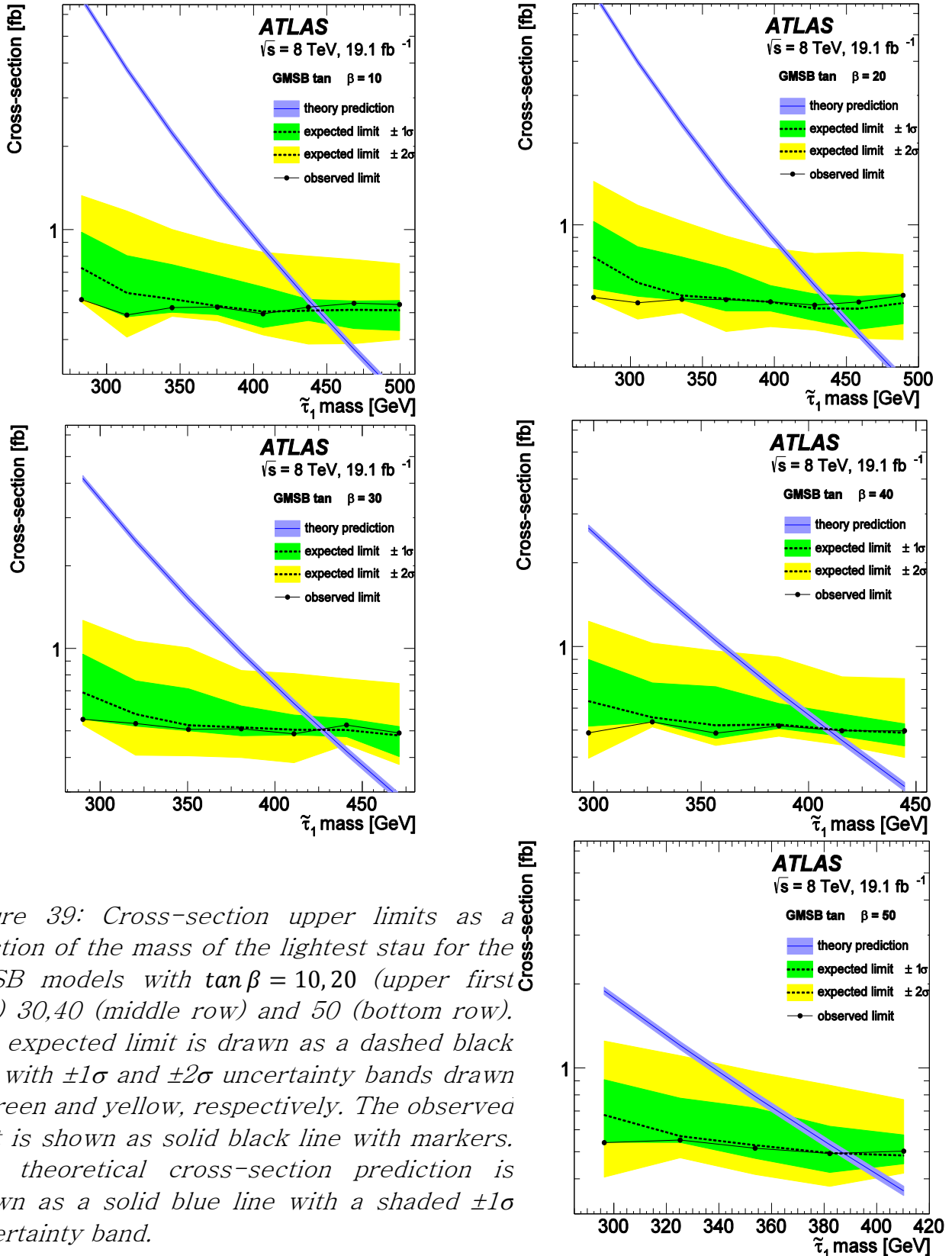


Figure 39: Cross-section upper limits as a function of the mass of the lightest stau for the GMSB models with $\tan\beta = 10, 20$ (upper first row) $30, 40$ (middle row) and 50 (bottom row). The expected limit is drawn as a dashed black line with $\pm 1\sigma$ and $\pm 2\sigma$ uncertainty bands drawn in green and yellow, respectively. The observed limit is shown as solid black line with markers. The theoretical cross-section prediction is shown as a solid blue line with a shaded $\pm 1\sigma$ uncertainty band.

Figure 41: 95% CL excluded regions for directly produced sleptons in the plane $m_{\tilde{l}} - m_{\tilde{\tau}_1}$ vs. $m_{\tilde{\tau}_1}$. The excluded region is shown in blue. The expected limit is drawn as a solid black line with a $\pm 1\sigma$ uncertainty band drawn in dashed black lines. The observed limit is shown as solid red line with a $\pm 1\sigma$ uncertainty band drawn as dashed red lines.

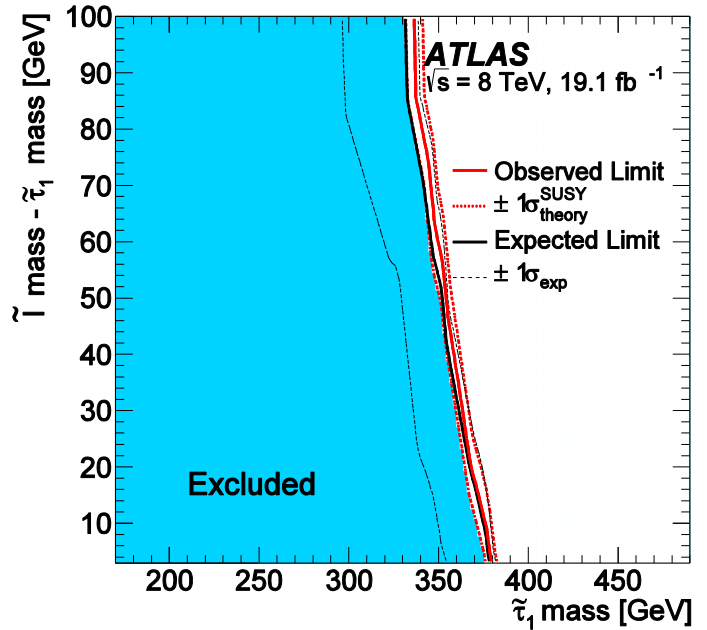


Figure 40: Cross-section upper limits as a function of the $\tilde{\tau}_1$ mass for direct $\tilde{\tau}_1$ production and three values of $\tan\beta$. The expected limit for $\tan\beta = 10$ is drawn as a dashed line with $\pm 1\sigma$ and $\pm 2\sigma$ uncertainty bands drawn in green and yellow, respectively. The observed limit for the three values of $\tan\beta$ are shown as solid lines with markers. The theoretical cross-section prediction for $\tan\beta = 10$ is shown as a colored $\pm 1\sigma$ band, and does not vary significantly for other $\tan\beta$ values.

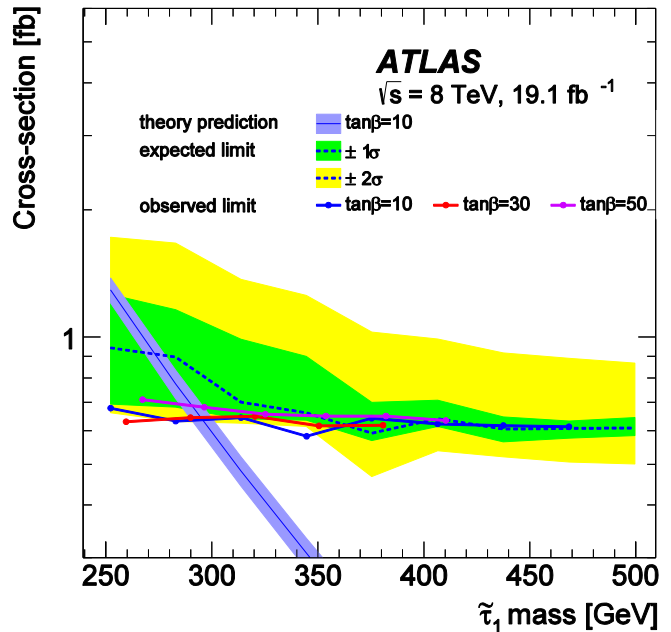


Figure 42: Cross-section upper limits as a function of the $\tilde{\chi}_1$ mass for $\tilde{\tau}_1$ sleptons resulting from the decay of directly produced charginos and neutralinos in GMSB. Observed limits are given as a solid black line with markers. Expected limits for $\tan\beta = 10$ are drawn as a dashed black line with $\pm 1\sigma$ and $\pm 2\sigma$ uncertainty bands drawn in green and yellow, respectively. The theoretical cross-section prediction (dominated by $\tilde{\chi}_1^\pm \tilde{\chi}_1^0$ production) is shown as a colored $\pm 1\sigma$ band. Depending on the hypothesis and to a small extent on $\tan\beta$, in these models, the chargino mass is 210 to 260 GeV higher than the neutralino mass.

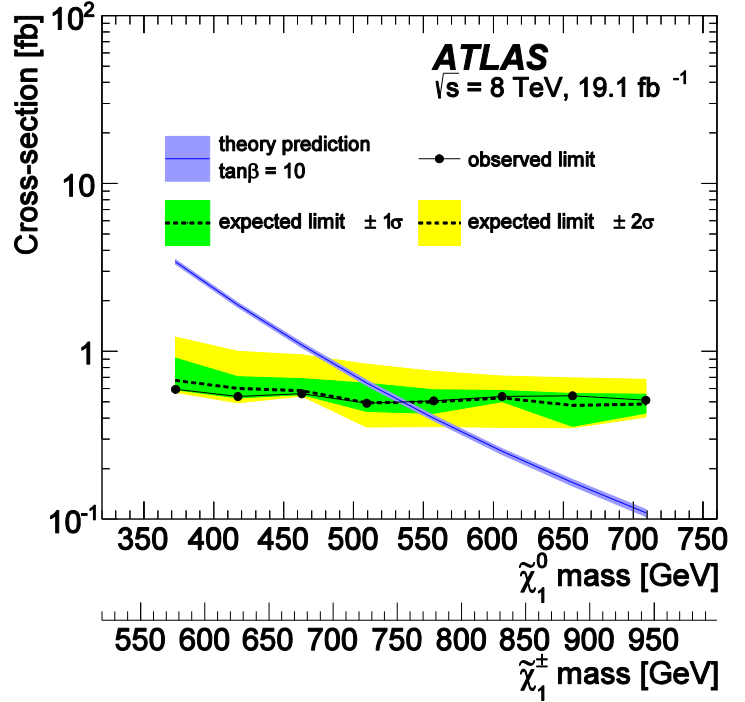
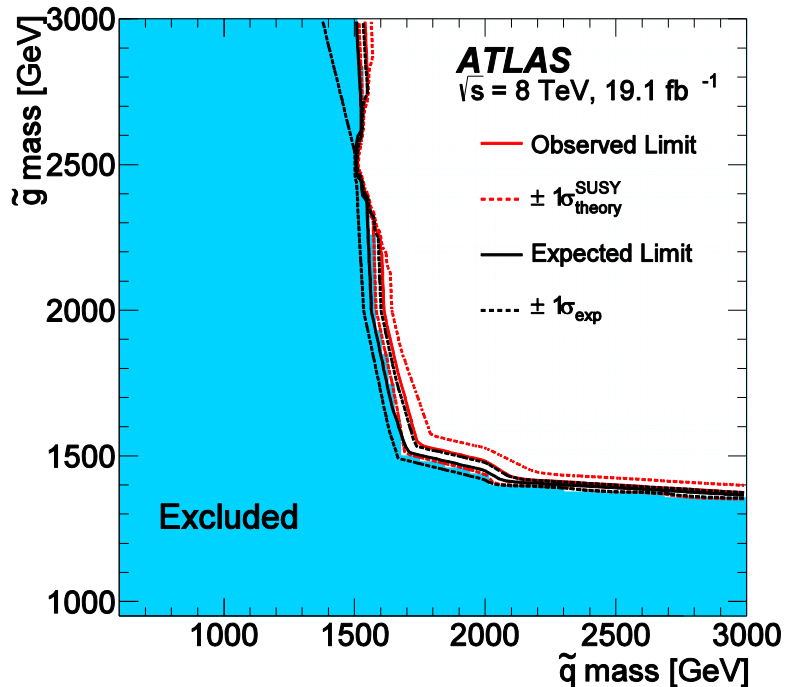


Figure 43: 95% CL excluded regions for squark and gluino mass in the LeptoSUSY models. The excluded region is shown in blue. The expected limit is drawn as a solid black line with a $\pm 1\sigma$ uncertainty band drawn in dashed black lines. The observed limit is shown as solid red line with a $\pm 1\sigma$ uncertainty band drawn as dashed red lines.



Signal Region	$\tilde{\tau}_1$ Mass [GeV]	345	407	469
Two candidate loose	m_β cut	240	270	469
	Expected signal	12.5	5.1	2.1
	Efficiency	0.28±0.01	0.29±0.01	0.28±0.01
	Estimated background	0.43±0.05	0.25±0.03	0.010±0.01
	Observed	0	0	0
One candidate tight	m_β cut	240	280	320
	Expected signal	8.5	3.5	1.5
	Efficiency	0.19±0.01	0.20±0.01	0.21±0.01
	Estimated background	49±5	27±3	15±1
	Observed	0.52	0.50	0.54
Cross -section limit [fb]		0.52	0.50	0.54

Table 25: Observed and expected event yields, as well as efficiencies and uncertainties for three MC simulation signal samples, in the two signal regions used in the GMSB slepton search. Cross-section upper limits are stated at 95% CL.

Signal Region	\tilde{g} Mass [GeV] \tilde{q} Mass [GeV]	1200 1600	2000 1400	3000 1600
Two candidate loose	m_β cut	190	190	190
	Expected signal	96.5	6.9	0.5
	Efficiency	0.27±0.01	0.30±0.01	0.19±0.01
	Estimated background	1.36±0.14	1.36±0.14	1.36±0.14
	Observed	0	0	0
One candidate tight	m_β cut	210	210	210
	Expected signal	66.9	4.9	0.5
	Efficiency	0.190±0.007	0.207±0.007	0.181±0.006
	Estimated background	80±7	80±7	80±7
	Observed	73	73	73
Cross -section limit [fb]		0.55	0.49	0.78

Table 26: Observed and expected event yields, as well as efficiencies and uncertainties for three MC simulation signal samples, in the two signal regions used in the LeptoSUSY slepton search. Cross-section upper limits are stated at 95% CL.

ii. Charginos

Limits are set on long-lived charginos, which are nearly degenerate with the lightest neutralino in the context of a stable chargino SUSY model. The production cross-section limits at 95% CL in this scenario as a function of the $\tilde{\chi}_1^\pm$ mass are presented in Figure 44 and compared to theoretical predictions. Masses below 620 GeV are excluded. The observed cross-section limit is found to be consistently one or two standard deviations (σ) above the expected limit, due to an excess of data events relative to the background estimate in the one-candidate-loose SR, as can be seen in Figure 19 (middle). However, this excess does not exhibit a peak which would indicate the presence of signal.

Table 27 shows an example for the observed and expected event yields, as well as efficiencies and uncertainties for data and some MC simulation signal samples for the stable chargino search.

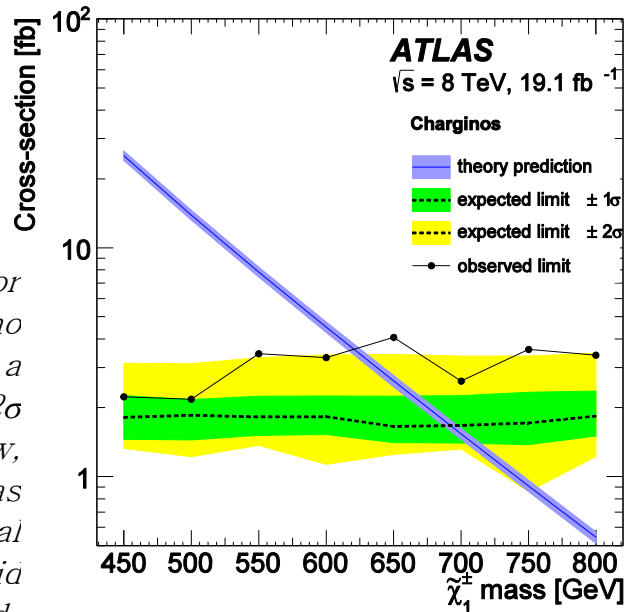


Figure 44: Cross-section upper limits for various chargino masses in stable-chargino models. The expected limit is drawn as a dashed black line with $\pm 1\sigma$ and $\pm 2\sigma$ uncertainty bands drawn in green and yellow, respectively. The observed limit is shown as solid black line with markers. The theoretical cross-section prediction is shown as a solid blue line with a dashed $\pm 1\sigma$ uncertainty band

Signal Region	$\tilde{\chi}_1^+$ Mass [GeV]	500	600	700
Two candidate loose	m_β cut	350	420	480
	Expected signal	16.9	4.9	1.5
	Efficiency	0.061±0.003	0.054±0.002	0.047±0.002
	Estimated background	0.053±0.006	0.018±0.003	0.008±0.001
	Observed	0	0	0
One candidate loose + MET	m_β cut	300	330	420
	Expected signal	35.0	10.7	3.3
	Efficiency	0.126±0.006	0.118±0.005	0.109±0.005
	Estimated background	29.6±0.3	21.1±0.3	8.6±0.3
	Observed	37	31	12
One candidate tight	m_β cut	340	430	450
	Expected signal	9.21	2.95	0.99
	Efficiency	0.033±0.002	0.033±0.002	0.032±0.002
	Estimated background	14.14±0.67	4.85±0.21	3.91±0.16
	Observed	14	6	6
Cross-section limit [fb]		2.18	3.31	2.62

Table 27: Observed and expected event yields, as well as efficiencies and uncertainties for three MC simulation signal samples, in the two signal regions used in the chargino search. Cross-section upper limits are stated at 95% CL.

iii. R-Hadrons

The R-hadron limits are shown in Figure 45. A lower mass limit at 95% CL of 1270 GeV for gluinos, 845 GeV for sbottoms and 900 GeV for stops is obtained.

Table 28 shows an example for the observed and expected event yields, as well as efficiencies and uncertainties for data and some MC simulation signal samples for the full-detector R-hadron search.

Signal Region	R-hadron type/Mass [GeV]	$\tilde{g}/1300$	$\tilde{b}/800$	$\tilde{t}/900$
Two candidate loose	m_β cut	785.1	560.3	612.9
	$m_{\beta\gamma}$ cut	746.9	512.7	565.5
	Expected signal	3.50	5.90	3.50
	Efficiency	0.11±0.01	0.11±0.01	0.17±0.02
	Estimated background	0.051±0.006	0.73±0.06	0.40±0.03
	Observed	0	1	0
Cross-section limit [fb]		1.33	1.80	0.84

Table 28: Observed and expected event yields, as well as efficiencies and uncertainties for three MC simulation signal samples, in the two signal regions used in the R-hadron search. Cross-section upper limits are stated at 95% CL.

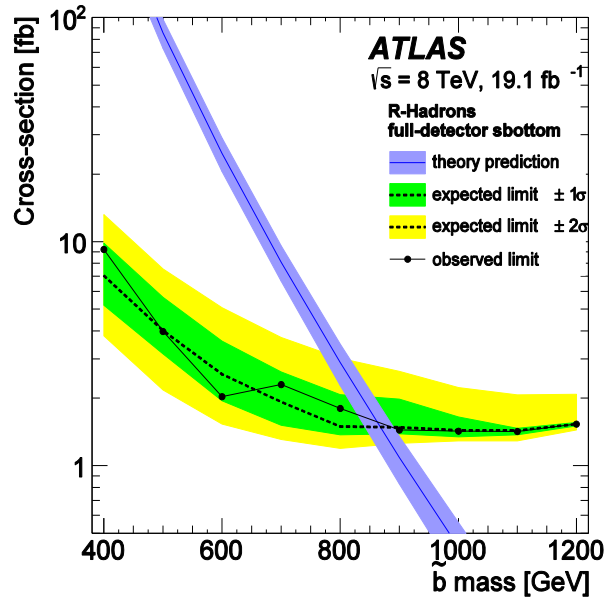
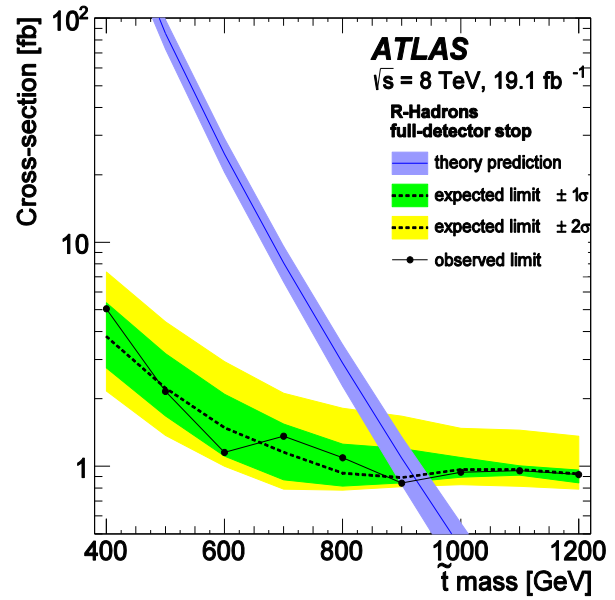
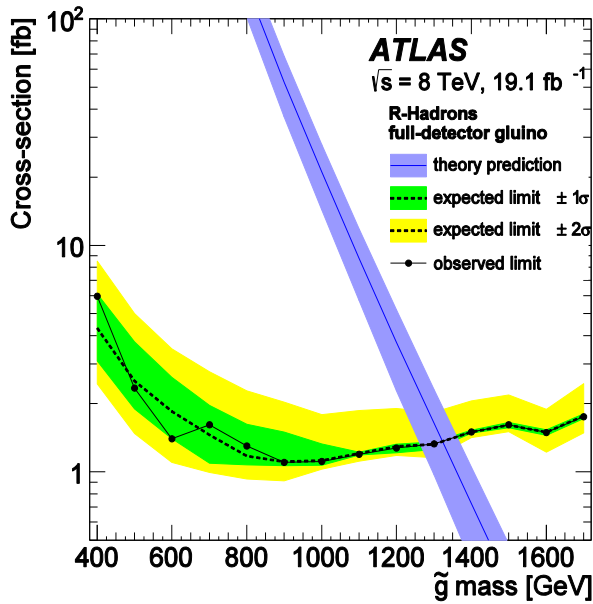


Figure 45: Cross-section upper limits as a function of the LLP mass for the R -hadron search. The expected limit is drawn as a dashed black line with $\pm 1\sigma$ and $\pm 2\sigma$ uncertainty bands drawn in green and yellow, respectively. The observed limit is shown as solid black line with markers. The theoretical cross-section prediction is shown as a solid blue line with a shaded $\pm 1\sigma$ uncertainty band.

XII. Summary

Searches for heavy long-lived charged particles are performed through measurements of the mass of candidates by means of time-of-flight and specific ionization loss measurements in ATLAS sub-detectors using data sample of fb^{-1} from proton-proton collisions at a center-of-mass energy of $\sqrt{s} = 8$ TeV collected by the ATLAS detector at the Large Hadron Collider. The data are found to match the Standard Model background expectation within uncertainties. The exclusion limits placed for various models impose new constraints on non-SM cross-sections.

An overview on all 95% CL lower mass limits placed in this search is given in Table 29.

The upper limits placed on cross-sections and lower limits placed on the mass of long-lived particles in various supersymmetric models, substantially extended previous ATLAS limits, and are largely complementary to searches for promptly decaying SUSY particles.

Search	Production	Lower mass limit [GeV]
GMSB sleptons	$\tan\beta = 10,20,30,40,50$	440, 440, 430, 410, 385
	Direct \tilde{l} production $\Delta m = m_{\tilde{l}} - m_{\tilde{\tau}_1} = 2.7 - 93 \text{ GeV}$	377-335
	Direct $\tilde{\tau}_1$ production	289
	$\tilde{\chi}_1^\pm \tilde{\chi}_1^0$ decaying to stable $\tilde{\tau}_1$	537
LeptoSUSY	\tilde{g}, \tilde{q} decaying to stable \tilde{l}	1500, 1360
Charginos	Direct $\tilde{\chi}_1^\pm$ production	620
R-hadrons	Full detector search for $\tilde{g}, \tilde{b}, \tilde{t}$	1270, 845, 900

Table 29: Summary of the lower mass limits at 95% CL from the various searches.

XIII. Bibliography

- [1] M. Fairbairn et-al, "Stable massive particles at colliders," *Phys. Rept.*, vol. 438, pp. 1-63, 2007.
- [2] N. Arkani-Hamed, S. Dimopoulos, "Supersymmetric unification without low energy supersymmetry and signatures for fine-tuning at the LHC," *JHEP*, vol. 073, no. 0506, 2005.
- [3] N. Arkani-Hamed, S. Dimopoulos, G. F. Giudice, A. Romanino, "Aspects of split supersymmetry," *Nucl. Phys.*, vol. B, no. 709.
- [4] M. Dine, W. Fischler, "A Phenomenological Model of Particle Physics Based on Supersymmetry," *Phys. Lett.*, vol. B110, no. 227, 1982.
- [5] L. Alvarez-Gaume, M. Claudson, M. B. Wise, "Low Energy Supersymmetry," *Nucl. Phys.*, vol. B207, no. 96, 1982.
- [6] C. R. Nappi, B. A. Ovrut, "Supersymmetric Extension of the $SU(3) \times SU(2) \times U(1)$ Model," *Phys. Lett.*, vol. B113, no. 175, 1982.
- [7] M. Dine, A. E. Nelson, "Dynamical supersymmetry breaking at low-energies," *Phys. Rev.*, vol. D48, p. 1277-1287, 1993.
- [8] M. Dine, A. E. Nelson, Y. Shirman, "Low-energy dynamical supersymmetry breaking simplified," *Phys. Rev.*, vol. D51, p. 1362-1370, 1995.
- [9] M. Dine, A. E. Nelson, Y. Nir, Y. Shirman, "New tools for low-energy dynamical supersymmetry breaking," *Phys. Rev.*, vol. D53, p. 2658-2669, 1996.
- [10] C. F. Kolda, "Gauge-mediated supersymmetry breaking: Introduction, review and update," *Nucl. Phys. Proc. Suppl.* , vol. 62, p. 266-275, 1998.
- [11] S. Raby, "Gauge mediated SUSY breaking at an intermediate scale," *Phys. Rev.*, vol. D56 , p. 2852-2860, 1997.
- [12] A. De Simone, J. Fan, V. Sanz, W. Skiba, "Leptogenic Supersymmetry," *Phys. Rev.*, vol. D80, no. 035010, 2009.

- [13] A. De Simone, J. Fan, M. Schmaltz, W. Skiba, "Low-scale gaugino mediation, lots of leptons at the LHC," *Phys. Rev.*, vol. D78, no. 095010, 2008.
- [14] A. collaboration, "Observation of a new particle in the search for the standard model Higgs boson with the ATLAS detector at the LHC," *Phys. Lett. B*, vol. 716, 2012.
- [15] C. collaboration, "Observation of a new boson at a mass of 125 GeV with the CMS experiment at the LHC," *Phys. Lett. B*, vol. 716, 2012.
- [16] M. Abdullah, I. Galon, Y. Shadmi, Y. Shirman, "Flavored Gauge Mediation, A Heavy Higgs, and Supersymmetric Alignment," *JHEP*, vol. 1306, no. 057, 2013.
- [17] J. L. Evans, M. Ibe, S. Shirai, T. T. Yanagida, "A 125GeV Higgs Boson and Muon $g-2$ in More Generic Gauge Mediation," *Phys. Rev.*, vol. D85, no. 095004, 2012.
- [18] J. L. Evans, M. Ibe, T. T. Yanagida, "Relatively Heavy Higgs Boson in More Generic Gauge Mediation," *Phys. Lett.*, vol. B705, no. 342, 2011.
- [19] collaboration, ATLAS, "Searches for heavy long-lived sleptons and R-hadrons with the ATLAS detector in pp collisions at 7 TeV," *Phys. Lett. B*, vol. 720, 2013.
- [20] S. P. Martine, "A Supersymmetry Primer," *arXiv:hep-ph*, vol. 9709356, 2008.
- [21] Tata, H. Baer and X., *Weak-scale Supersymmetry*, Cambridge: Cambridge University Press, 2006.
- [22] A. C. Kraan, "Interactions of Heavy Stable Hadronizing Particles," *hep-ex/0404001*, 2004.
- [23] R. Mackeprang, D. A. Milstead, "An update description of heavy-hadron interactions in GEANT-4," *Eur. Phys. J. C.*, vol. 66, 2010.
- [24] Collins, P. D. B., "Regge theory and particle physics," *Phys. Rept.*, vol. 1, no. 103-234, 1971.

- [25] A. Collaboration, "Search for heavy long-lived charged particles with the ATLAS detector in pp collisions at $\sqrt{s}=7$ TeV," *Phys. Lett. B*, vol. 703, pp. 428–446, 2011.
- [26] A. collaboration, "The ATLAS Experiment at the CERN Large Hadron," *JINST*, vol. 3, no. S08003, 2008.
- [27] T. Sjostrand, S. Mrenna, and P. Skands, "PYTHIA 6.4 Physics and Manual," *JHEP*, vol. 05, no. 026, 2006.
- [28] M. Bahr, S. Gieseke, M. Gigg, D. Grellscheid, K. Hamilton, et al., "Herwig++ Physics and Manual," *Eur.Phys.J.*, vol. C58, p. 639–707, 2008.
- [29] J. Alwall, M. Herquet, F. Maltoni, O. Mattelaer, and T. Stelzer, "MadGraph 5 : Going Beyond," *JHEP*, vol. 06, p. 128, 2011.
- [30] P. Meade and M. Reece, "BRIDGE: Branching Ratio Inquiry/Decay Generated Events," *arXiv:hep-ph/0703031*.
- [31] T. Sjostrand, S. Mrenna, and P. Z. Skands, "A Brief Introduction to PYTHIA 8.1," *Comput.Phys.Commun.*, vol. 178, p. 852–867, 2008.
- [32] S. A. e. a. GEANT4 Collaboration, "GEANT4: A simulation toolkit," *Nucl. Instrum. Meth.*, vol. A506, p. 250–303, 2003.
- [33] A. Collaboration, "dE/dx measurement in the ATLAS Pixel Detector and its use for particle identification," *Tech. Rep. ATLAS-CONF-2011-016*, 2011.
- [34] A. Collaboration, "Search for long-lived stopped R-hadrons decaying out-of-time with pp collisions using the ATLAS detector," *arXiv:1310.6584v3*, 2013.
- [35] W. Beenakker, M. Kramer, T. Plehn, M. Spira, and P. M. Zerwas, "Stop production at hadron colliders," *Nucl. Phys. B*, vol. 515, p. 3–14, 1998.
- [36] W. Beenakker, S. Brensing, M. Kramer, A. Kulesza, E. Laenen, and I. Niessen, "Supersymmetric top and bottom squark production at hadron colliders," *JHEP*, vol. 1008, no. 098, 2010.
- [37] W. Beenakker, S. Brensing, M. Kramer, A. Kulesza, E. Laenen, et al., "Squark and gluino hadroproduction," *Int.J.Mod.Phys. A*, vol. 26, p. 2637–2664, 2011.

- [38] M. Kramer, A. Kulesza, R. van der Leeuw, M. Mangano, S. Padhi, et al., "Supersymmetry production cross sections in pp collisions at $\sqrt{s} = 7$ TeV," *arXiv:1206.2892 [hep-ph]*.
- [39] collaboration, ATLAS, "Performance of the ATLAS muon trigger in pp collisions at $\sqrt{s} = 8$ TeV," *CERN-PH-EP-2014-154*, 2014.
- [40] A. Collaboration, "Improved luminosity determination in pp collisions at $\sqrt{s} = 7$ TeV using the ATLAS detector at the LHC," *Eur.Phys.J.*, vol. C73, no. 2518, 2013.
- [41] Read, A. L., "Presentation of search results: the CLs technique," *J. Phys. G*, vol. 28, p. 2693–2704, 2002.
- [42] L. Moneta, K. Belasco, K. Cranmer, S. Kreiss, A. Lazzaro, D. Piparo, M. Schott, W. Verkerke, and M. Wolf, "the RooStats Project," *arXiv*, 2010.
- [43] T. J. Khoo, "CERN Twiki".



**חיפוש אחר חלקיקים בעלי מטען חשמלי זמן חיים
ארוך עם גלאי האטלס בעת התנגשויות פרוטונים
באנרגית מרכז-מסה של 8 TeV**

חיבור על מחקר



לשם מילוי הדרישות לקבלת התואר

דוקטור לפילוסופיה

רויטל קופליאנסקי

המחקר נעשה בהנחיית פרופ' שלומית טרם בפקולטה לפיסיקה

אני מודה לטכניון על התמיכה הכספית הנדיבה בהשתלמותי

הוגש לסנט הטכניון - המכון הטכנולוגי לישראל

אוגוסט 2015

חיפה

אלול, תשע"ה

תקציר

תאוריות רבות המרחיבות את המודל הסטנדרטי של פיסיקה החלקיקים מנבאות את קיומם של חלקיקים בעלי זמן חיים ארוך דיו בכדי לנוע לאורכו של הגלאי אטלס ובכך לגלותם. תאוריית סימטריית-העל (Supersymmetry) היא אחת מתאוריות אלו והיא מאפשרת את קיומם של חלקיקים נוספים המהווים 'בני-זוג' של החלקיקים מהמודל הסטנדרטי. חלקם אף ארוכי-חיים מספיק בכדי לגלותם, ביניהם בני הזוג של הקווארקים, הלפטונים ובוזוני הכיול.

חלקיקים אלו עשויים להיווצר בהתנגשויות האנרגטיות של המאיץ ההדרוני הגדול (LHC) ובמידה ואכן יוצרו, ניתן יהיה למדוד את התנע הקווי שלהם ואת מהירותם ובכך לאמוד את מסתם על ידי שימוש בנוסחה: $m = \frac{p}{\beta\gamma}$.

עבודת מחקר זו מציגה חיפוש אחר חלקיקים כבדים, בעלי מטען חשמלי וזמן חיים ארוך, באמצעות הגלאי אטלס הממוקם באחת מארבע נקודות התנגשות הפרוטונים של המאיץ ההדרוני הגדול. החיפוש מתבסס על נתונים שנאספו בהתנגשויות פרוטונים באנרגית מרכז מסה של 8TeV, ונאספו על ידי הגלאי אטלס עם הארה כוללת של 19.8fb^{-1} .

החיפוש מתמקד בשני סוגי חלקיקים: חלקיקים נטולי מטען צבע: בני זוג של הלפטונים (ס-לפטונים) ובני הזוג של בוזוני הכיול (צ'ארגינוס), וחלקיקים נושאי מטען צבע: בני הזוג של הגלואון והקווארקים, גלואינואים וס-קווארקים בהתאמה, המתאגדים יחד עם חלקיקים נושאי מטען צבע רגילים למצב אנרגטי נטול צבע המכונה: הדרוני-R.

החיפוש אחר סלפטונים יציבים נעשה במסגרת מודלים של שבירת סופר-סימטריה על ידי בוזוני כיול (GMSB), ובמסגרת מודל פשוט יותר בו הסלפטונים בעלי מסה קבועה הנוצרים מדעיכתם של גלואינו ו/או סקווארק בעלי מסות שונות, בדעיכת שרשרת המלווה בהיווצרות לפטונים וסילונים.

החיפוש אחר צ'ארג'ינוס נעשה במסגרת מודל פשוט בו עשויים להיווצר זוג פרמיונים הנובעים מסופרפוזיציה של בני הזוג של בחוני כיוול (ווינו, היגסינו ובינו): צארג'ינו ונאוטרלינו ב-66% מהמיקרים וזוג צ'ארג'ינו ב-33% מהמיקרים. מאורעות אלו לא אמורים להכיל חלקיקים סופרסימטריים נוספים.

החיפוש אחר הדרוני-R נעשה במסגרת מודל SplitSUSY בו הגלואינו (בן הזוג הסופרסימטרי של הגלואון) הינו החלקיק ארוך החיים, ובמסגרת מודלים מופשטים יותר בהם החלקיק ארוך החיים הוא הסטופ- בן הזוג של הקווארק טופ, או סבוטום - בן הזוג של הווארק בוטום.

המאיץ ההדרוני הגדול הינו מאיץ חלקיקים הממוקם במרכז האירופאי הגדול לחקר הגרעין (CERN) שעל גבול שוויץ-צרפת. היקפו של המאיץ 27 ק"מ והינו מתוכנן להנגיש פרוטונים באנרגיות של עד 14TeV בקצב של 40MHz. עבודת מחקר זו מבוססת על שלב האצת פרוטונים של 8TeV ובקצב של 20MHz.

הגלאי אטלס הינו גלאי חלקיקים הממוקם באחת מארבע נקודות התנגשות הפרוטונים של המאיץ ההדרוני הגדול. צורתו גליל ומבנהו שכבות גלאים שונים שנועדו לזהות סוגי חלקיקים שונים. הגלאי הפנימי ביותר, שמטרתו לאתר מסלולים של חלקיקים בעלי מטען חשמלי שנוצרו כתוצאה מהתנגשות הפרוטונים, מושרה בשדה מגנטי המעקם את מסלול התנועה של חלקיקים ובכך מאפשר את מדידת התנע של החלקיקים. גלאי זה עטוף בשכבת גלאים נוספת מסוג קלורימטרים, הסופגים את אנרגיית החלקיקים שעוברים דרכם ומאפשרים את מדידת האנרגיה שלהם. שכבת גלאים מסוג ספקטרומטר מיואנים עוטפת את שכבת הקלורימטרים והיא מהווה השכבה החיצונית של הגלאי. מטרת הספקטרומטר הינה לאתר חלקיקים מסוג מיואונים שאינם נבלמים על ידי השכבות הפנימיות יותר.

הסלפטונים והצ'ארג'ינואים ישאירו חתימת גלאי דומה לזו של מיואונים, ולכן גילויים יעשה בעזרת כל שכבות הגלאי. הדרוני-R יבצעו אינטראקציות חזקות עם גרעיני החומר

שבקלורימטר, העשויים להוביל לשינוי המבנה ההדרוני שלהם ובכך לשנות את מטענם החשמלי. במסגרת עבודת מחקר זו, נעשה חיפוש אחרי הדרוני-R המשאירים חותם בכל מסלולי הגלאי או במקרה שבו מטענם שונה לניטרלי בעת מעבר בקלורימטר, ולכן חותמם יופיע בגלאי הפנימי והקלורימטרים בלבד.

עבור חלקיקים הטעונים בעת מעבר בכל שכבות הגלאי, החיפוש נעשה באמצעות חיפוש אחר חתימה בגלאי המסלולים הפנימי, זאת על ידי יינון הגז שבגלאי הפנימי המאפשר מדידת $\beta\gamma$, ובעזרת ממוצע משוקלל של β הנמדד מזמני האותות בקלורימטר ושכבות גלאי המיואונים השונים: RPC (תאי לוחות בעלי התנגדות) ו-MDT (צינורות סחיפה מבוקרים) המשמשים להארכת מהירות החלקיקים β . עבור חלקיקים מסוג הדרוני-R שחתימתם בשכבות הגלאי החיצוניות חסרה, נעשה שימוש במדידת מהירותם על ידי הקלורימטר בלבד.

המודל הסטנדרטי אינו מנבא את קיומם של חלקיקים כבדים ויציבים ולכן הרקע לחתימה הפיסיקאלית של חלקיקים אלו יהיה מורכב בעיקרו ממיואונים בעלי תנע גבוה ומדידת מהירות לא מדוייקת כך שהיא קטנה מהמצופה ממיואון. בכדי להקטין את כמות המיואונים המשוקללים, בגרף המסה נילקחים בחשבון רק מיואונים שמהירותם נמדדה כקטנה מ-95% ממהירות האור.

אסטרטגיית החיפוש מונעת משלושה גורמים המבטיחים את איכות התוצאות של מחקר מסוג זה:

1. שיפור רזולוציית המהירות הנמדדת: ככל שרזולוציית המדידה יותר טובה התפלגות המדידה יותר צרה, ובכך 'זנבות' המדידה יותר קטנים. דבר שמבטיח כי פחות פלוקטואציות יכללו במהירות המשוקללת ובכך קטן הסיכוי שאנומליות שמקורן בתופעות רקע המדידה יופיעו בגרף המסה וידמו תגלית. לאחר ממוצע משוקלל של כל המדידות התקבלה רזולוציית מדידה של 2.4% עבור המהירות הנמדדת.

2. דחיית רקע: הינה אלמנט חשוב בהבחנה בין מדידת חלקיק מן המודל הסטנדרטי וחלקיק שמקורו בפיסיקה חדשה. עיקרה מבוססת על דרישות המתייחסות לאיכות השיחזור של נתוני החלקיק ולאיכות מדידת מהירותו. כמו כן, בחירת מועמדים בעלי מהירות קטנה באופן משמעותי ממהירות האור. שלב זה נעשה תוך כדי הקפדה על אופי חיפוש שאינו תלוי במודל המנבא את קיום החלקיק (ככל האפשר).

במסגרת מודלי ה-GMSB השונים אשר מנבאים את קיומם של סלפטונים יציבים, צפויים להיווצר סלפטונים יציבים תמיד בזוגות, ולכן במידה ואכן ייווצרו בהתנגשות קיים סיכוי גבוה לגילוי שני החלקיקים. החיפוש אחר חלקיקים מסוג סלפטונים יציבים דורש כי המאורעות יכללו לפחות שני מסלולים משולבים (מהגלאי פנימי ועד לגלאי המיואונים) על מנת להיבחר. דרישה זו לשני מועמדים במאורע בעלי מהירות נמוכה ותנע גדול, מקטינה משמעותית את הרקע שכן הסיכוי לאתר שני מועמדים כאלו קטן, ולכן מאפשרת שימוש בתנאים מקלים יחסית בשאר פרמטרי הבחירה. מאורעות המכילים מסלול אחד בלבד העונה לדרישות המקלות יעברו סלקציה נוספת מחמירה יותר על מנת להקטין את מאורעות הרקע הנכנסים לשקלול. אסטרטגיית איתור חלקיקים אלו ננקטה גם בחיפוש אחר סלפטונים במסגרת מודל מופשט יותר של חיפוש סלפטונים (LeptoSUSY) וגם לחיפוש אחר הדרוני-R (למעט הדרישה לשני מועמדים במאורע ולחתימה בגלאי המיואונים). עבור חלקיקי הצ'ארג'ינוס שמשאירים חותמת דומה בגלאי לסלפטונים טעונים ננקטה אסטרטגיה דומה למעט הבדל אחד, בחיפוש אחר חלקיקי צ'ארג'ינוס ההנחה היא שב-66% מהמאורעות בהן ייווצרו צ'ארג'ינו יוצר עימו ניאוטרינו (בזון כיוול חסר מטען חשמלי) ולכן עבור מאורעות אלו נדרש כי המאורע יכיל 'אנרגיה חסרה' בערך הגבוהה מ-100GeV (במערכת מרכז-המסה סך כל התנע הוא אפס. אם בשקלול חתימות המאורע סך כל התנע שונה מאפס, ההפרש יכונה כ'אנרגיה חסרה').

3. הערכת הרקע למדידה: אומדן מדוייק של התפלגות המסה של הרקע וכמותו הינה הכרחית לקביעת גבולות חיפוש חדשים או לתגלית של חלקיק חדש. הרקע, צורת התפלגותו וכמותו מוערכים באופן ישיר מנתוני המדידה, ללא שימוש בסימולציות. מכיוון והמהירות המדודה של הרקע הינה פונקציה של הרזולוציה של המדידה ואינה תלויה בתנע של החלקיק, ניתן לקבל את התפלגות המסה על ידי חישוב מסה על ידי זיווג בין מדידת תנע ומהירות ממועמדים שונים שנבחרו באופן אקראי ואינם שייכים לאותו חלקיק.

תוצאות מחקר זה הניבו נתונים שנמצאו עקביים עם הערכת הרקע מהמודל הסטנדרטי, ולא נמצאו סטיות המצביעות על תגלית של פיסיקה חדשה. לכן גבולות חדשים לקיומם של חלקיקים יציבים מעבר למודל הסטנדרטי הוצבו:

עבור סלפטונים מסוג סטאו (בן הזוג של הלפטון - טאו) במסגרת מודל הGMSB עם הפרמטרים: $m_{messenger} = 250 \text{ TeV}, N_5 = 3, sign(\mu) = 1, c_{grav} = 5000, \tan \beta: 10 \rightarrow 50$ נשללו במידת ביטחון של 95% עד למסה של 440 GeV. עבור זוג סלפטוני סטאו שנוצרו כתוצאה מהיווצרות של צ'ארג'ינו ונאוטרלינו הדועכים לסטאו, נשללו במידת ביטחון של 95% מסות נאוטרלינו הקטנות מ-537 GeV. סלפטונים יציבים הנוצרים באופן ישיר ודועכים לסטאו נשללו במידת ביטחון של 95% עד למסה של 377 GeV עבור מודלים שבהם הפרש המסות בין הסלפטונים האחרים והסטאו קטן מ-93 GeV. עבור זוג סלפטוני סטאו הנוצרו באופן ישיר נשללו במידת ביטחון של 95% מסות הקטנות מ-289 GeV. עבור חיפוש אחר סלפטון שנוצר מדעיכה של סקווארק או גלואינו במסגרת המודל המופשט LeptoSUSY נפסלו במידת ביטחון של 95% מסות סקווארקים הקטנות מ-1500 GeV ומסת גלואינו הקטנה מ-1360 GeV. במיסגרת החיפוש אחר צ'ארג'ינו יציב, נפסלו במידת ביטחון של 95% מסות צ'ארג'ינו הקטנות מ-620 GeV.

בחיפוש אחרי הדרוני-R עם גלואינו נפסלו במידת ביטחון של 95% מסות גלואינו הקטנות
מ-1270 GeV. עבור הדרוני-R עם סטופ וסבוטום נפסלו בביטחון של 95% מסות של 900 GeV
ו-845 GeV, בהתאמה.